Structural characterization of recombinant and pathogenic Amyloidβ(1-42)-Peptide by solid-state Nuclear Magnetic Resonance Spectroscopy

Inaugural-Dissertation

zur Erlangung des Doktorgrades
der Mathematisch-Naturwissenschaftlichen Fakultät
der Heinrich-Heine-Universität Düsseldorf

vorgelegt von
Daniel Schölzel
aus Düsseldorf

Düsseldorf, Dezember 2018

Aus dem Institut für Physikalische Biologie
der Heinrich-Heine-Universität Düsseldorf

Gedruckt mit der Genehmigung der
Mathematisch-Naturwissenschaftlichen Fakultät der
Heinrich-Heine-Universität Düsseldorf

Berichterstatter:

1. Prof. Dr. Henrike Heise
2. Prof. Dr. Gunnar Schröder

Tag der mündlichen Prüfung:
13.12.2018

Contents

Abbreviations

Aβ	Amyloid-β
ACH	Amyloid cascade hypothesis
AD	Alzheimer's disease
APP	Amyloid precursor protein
CP	Cross polarization
cryoEM	Cryogenic electron microscopy
CSA	Chemical shift anisotropy
DNP	Dynamic nuclear polarization
H/D	Hydrogen/deuterium
INEPT	Insensitive nuclei enhanced by polarization transfer
MAS	Magic angle spinning
MW	Microwave
NMR	Nuclear magnetic resonance (spectroscopy)
PAIN	Proton-assisted insensitive nuclei
PDSD	Proton-driven spin diffusion
RMSD	Root mean squared deviation
ROS	Reactive oxygen species
RT	Room temperature
SNR	Signal to noise ratio
SPC5	Supercycled permutationally offset stabilized C5
ss	Solid-state
SW	Spectral width
ThT	Thioflavin t

Abstract

The 42 amino acid residue amyloid-β (Aβ(1-42)) peptide is involved in the development of Alzheimer's disease. Since it is more prone to aggregation than the more abundant Aβ(1-40) and furthermore involved in the early onset of the disease, it is of particular research interest. In the literature it has been shown, that these two addtional C-terminal residues not only accelerate the aggregation kinetics, but also lead to the formation of different molecule interfaces, β-sheet lengths and β-sheet arrangements.

In this combined study, we determined the structure of an hitherto undescribed recombinantly expressed Aβ(1-42) fibril polymorph with cryo-EM and solid-state NMR (ssNMR) on the same sample. To achieve this goal, a complete de-novo resonance assignment had to be accomplished by the acquisition of one and higher dimensional spectra.

The analysis of the measured chemical shifts yielded the secondary structure model, as well as hints for the protonation state of the acidic amino acids and the steric side-chain orientation. Furthermore, we could observe long-range contacts, confirming the structure determined by cryo-EM. All results combined exhibited a rigid S-shaped middle domain and C-terminus of the fibril, with a less rigid N-terminus. Notably, published cryo-EM or ssNMR studies of Aβ(1-42) fibril structures up to date described other polymorphs.

To investigate low temperature effects on sample preparation, resolution and signal enhancement, we carried out dynamic nuclear polarization (DNP) measurements. We tested two different sample preparation protocols, finding the standard preparation seems to be superior to our customized procedure. In addition, we found that cryogenic temperatures decreased the spectral resolution, which could be partly restored by measuring in higher static magnetic fields. Measuring relaxation rates in the transverse plane (T_ρ^1) with our experimental setup, was not suitable to detect a rather flexible N-terminus compared to the middle domain and the C-terminus. Additionally, we probed the fibril water interface by measuring the polarization transfer from water to the protein, facilitated by exchangeable protons. Afterwards, we tried to study the effect of Thioflavin-T (ThT) binding to the fibril, however the binding was impeded by the low pH of our sample.

Lastly, fibrils prepared at pH 7 were compared to the initial fibril sample at pH 2, indicating a possible second conformer at the N-terminus.

Zusammenfassung

In der Entwicklung der Alzheimer'schen Demenz spielt die Produktion des aus 42 Aminosäuren bestehenden Peptids Amyloid β (Aβ(1-42)) eine wichtige Rolle. Aufgrund der Tatsache, dass es schneller aggregiert als das häufigere Aβ(1-40) und bei der erblichen Form der Erkrankung involviert ist, ist es von besonderem Forschungsinteresse. Veröffentlichte Studien zeigen den starken Einfluss dieser zwei zusätzlichen C-terminalen Aminosäuren auf die Aggregationskinetik, der Ausprägung unterschiedlicher Molekülgrenzflächen und einer veränderten Anordnung und Länge der β-Faltblätter in der Fibrille.
In dieser kombinierten Cryo-EM und Festkörper-NMR Studie präsentieren wir die Fibrillenstruktur eines rekombinant-exprimierten Aβ(1-42)-Fibrillen-Polymorphs. Zur Aufklärung der Struktur musste zuerst eine vollständige de-novo Resonanzzuordnung mit ein- und höher-dimensionalen Spektren erfolgen.
Die Analyse der gemessenen chemischen Verschiebungen lieferte uns ein Sekundär-Strukturmodell, sowohl als auch Hinweise auf den Protonierungsgrad saurer Aminosäuren und der sterischen Seitenkettenorientierung. Die Detektion von langreichweitigen Kontakten konnte zusätzlich die Cryo-EM Ergebnisse bestätigen.
Zusammengenommen ergaben alle Resultate eine S-förmige Mittendomäne und C-Terminus der Fibrille, mit einem weniger rigiden N-Terminus. Beachtenswert ist, dass vorherige Festkörper-NMR- oder Cryo-EM-Studien unterschiedliche Aβ(1-42)-Fibrillen-Polymorphe beschrieben haben.
Zur Untersuchung der Temperaturabhängigkeit von Probenvorbereitung, Auflösung und Signalverstärkung benutzten wir "Dynamic Nuclear Polarization" (DNP)-Messungen. Wir testeten zwei verschiedene Probenvorbereitungs-Protokolle mit dem Ergebnis, dass das Standardprotokoll unserem angepassten Protokoll überlegen ist. Zusätzlich wiesen wir nach, dass kryogene Temperaturen zwar die spektrale Auflösung verschlechtern, dieser Effekt aber mit der Messung in einem höheren statischen Magnetfeld teilweise kompensiert werden kann. Das Messen von Relaxationszeiten in der Transversalebene (T_ρ^1) mit unserem experimentellen Aufbau, war nicht dazu geeignet einen mobileren N-Terminus zu detektieren, verglichen mit der rigiden Mittendomäne und dem C-Terminus. Desweiteren untersuchten wir die Fibrillen-Wassergrenzfläche durch Messung des Polarisationstransfers von Wasser auf die Fibrille, der durch austauschbare Protonen erleichtert wurde.
Abschließend versuchten wir den Effekt von Thioflavin-T-Bindung an die Fibrille zu untersuchen, was jedoch durch den niedrigen pH-Wert unserer Probe verhindert wurde. Zuletzt wurde eine Fibrillenprobe bei pH 7 untersucht, wobei die Ergebnisse auf ein mögliches zweites Konformer hinweisen.

1 Introduction

1.1 Amyloid-β

The following sections aim to provide a brief explanation of the field of Amyloid-β research, mentioning the most crucial contributions.

1.1.1 Amyloid cascade hypothesis

The amyloid-β peptide (Aβ) is well known as one of the histological hallmarks of Alzheimer's disease (AD), since the first description of the symptoms by Alois Alzheimer in 1906 [1]. The peptide forms microscopic deposits called amyloid plaques. The name amyloid is derived from its starch-like staining property, upon staining with iodine. The plaques can develop pathogenic characteristics, facilitating the formation of lesions in the brain, depending on their molecular structure.
Primarily, pathogenic assemblies lead to the death of neurons, causing symptoms of losses in memory, reasoning, abstraction, and language. Investigating and solving the molecular structure of the pathogenic aggregates has since been a target of proceeding research.
During the mid-1980s, the extracellular and insoluble neuritic plaques were structurally analyzed and found to be composed of Aβ peptides [2, 3].
Aggregation of Aβ peptides as functional moieties facilitating and/or causing neuronal death, led to the formulation of the amyloid cascade hypothesis [4].
The amyloid cascade hypothesis states Aβ aggregation and deposition would cause a cascade of events leading to pathological degeneration of neuronal cells, cell death and dementia. This hypothesis is deduced from several inherited mutations causing massive Aβ deposition and triggering an early onset of AD. [5–7]. Of note, there are some inconsistencies in the amyloid cascade hypothesis (ACH) [8]. It is not clear if plaques could be the product of neurodegenerative processes and if the aggregation and deposition leads to the formation of neurofibrillary tangles. The latter are a second pathogenic species of deposits, formed by hyperphosphorylated tau-proteins.

1.1.2 Aβ(1-42)

Aβ peptides are proteolytically cleaved from the integral membrane amyloid precursor protein (APP) in two steps and comprise up to 43 amino acids [9]. The most abundant isoform comprises 40 residues. Interestingly, in familiar AD-linked mutations, the production of the more aggregation prone Aβ(1-42) isoform is increased [10]. The primary sequence of Aβ(1-42) contains 6 charged amino acids, resulting in a net charge of −3 and several accumulated hydrophobic residues in the C-terminus.

1				**5**					**10**
D	A	E	F	R	H	D	S	G	Y
				15					**20**
E	V	H	H	Q	K	L	V	F	F
				25					**30**
A	E	D	V	G	S	N	K	G	A
				35					**40**
I	I	G	L	M	V	G	G	V	V

I A

Table 1.1: primary sequence of Aβ(1-42)

1.1.3 Aggregation

Aggregation of amyloidogenic peptides, like Aβ, in vitro, can be separated into three characteristic stages: lag-phase, growth phase and plateau phase, resulting in a sigmoidal fluorescence profile [11]. The terminology arises from the fluorescence intensity profile of thioflavin t (ThT), which binds to the growing fibrils, increasing the fluorescence intensity upon binding.
To spark the aggregation process, a condensed particle, consisting of previously soluble molecules, has to be formed. This process is termed primary nucleation and still under investigation [12]. After the initial nucleation, the fibril starts to grow (elongation). Elongation can be inverted by dissociation and fragmentation. The latter, in collaboration with secondary nucleation, are termed secondary processes.

1.1.4 Physiology

A mouse model proved that intracerebroventricular application of Aβ(1-42), dissolved in saline and in picomolar concentrations, improves cognitive function [13].

In addition, several studies could prove that the application of Aβ antibodies impaired the learning abilities of different animal species. Conversely, the application of nanomolar concentrations into the hippocampus of mice has been shown to be amnestic. Due to these facts one could argue that physiological concentrations seem to enhance learning and retention, whereas pharmacological concentrations hamper memory performance.
In addition, Aβ indirectly and directly modulates the mitochondrial function, as well as mitochondria regulate Aβ production [14, 15].
Furthermore, Aβ is suggested to have antimicrobial functions in vivo, strengthening the immune system [16].

1.1.5 General architecture of amyloid fibrils

Aggregation into fibrils seems to be a possible pathway of a wide variety of proteins, not only limited to Aβ [17]. On a microscopic length scale amyloid fibrils, like Aβ fibrils, have a long rod-like shape ranging from 5 to 10 nm in width and up to μm in length [18]. In fibre diffraction experiments, amyloid fibrils display a quite unique cross-β diffraction pattern (see figure 1.1) [19]. From the fibre diffraction experiments one can derive geometrical features of the fibrils:
One or several β-strands run perpendicular to the fibril axis and form β-sheets with roughly 5 $\AA$ inter-strand spacing, connected by inter-molecular hydrogen bonds. The spacing between the sheets shows a lower intensity in the diffraction experiments and has a width of approximately 10 $\AA$ [20, 22]. The accurate distance between the sheets is determined by the arrangement of the amino acid sidechains, which can conjoin to a waterfree interface (steric zipper), or stick out of the fibril towards the surrounding medium [21].

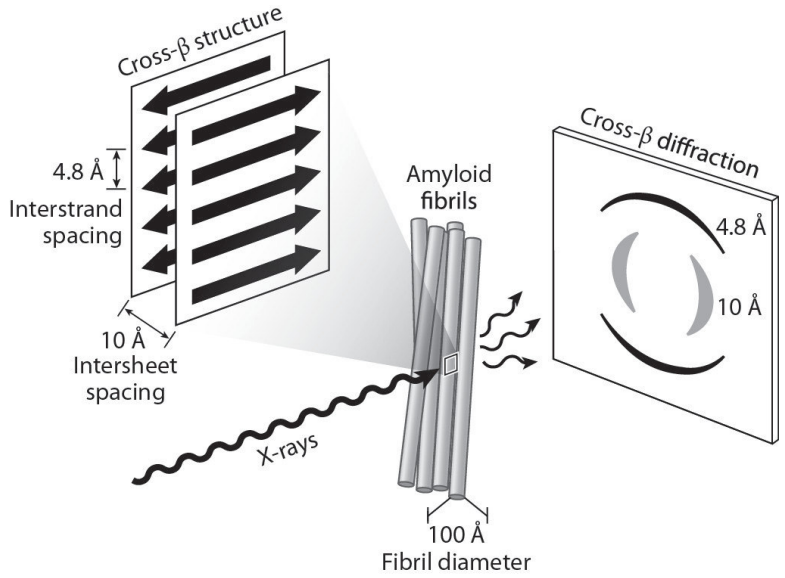

Figure 1.1: Exemplified fibre diffraction experiment and result [22].

1.1.6 Structural investigations of amyloid fibrils

In this subsection, a short overview of published amyloid structural models as well as structures will be presented, focusing on Aβ(1-40) and (1-42) solid-state NMR (ssNMR) studies, respectively.
During the 1990s several work groups started with the investigation of short fibril fragments, derived from the full-length sequence of Aβ. Depending on the primary sequence of the synthetic fragment derived from the full length protein, different properties could be generated, like Aβ(34-42), a fragment mainly containing hydrophobic residues [23–25]. Within these studies backbone distances of selectively labeled residues were measured with ssNMR, indicating an antiparallel β-sheet geometry. Similarly, two other publications focusing on selectively labeled synthetic Aβ(11-25) and Aβ(14-23) fragments, suggested an antiparallel β-sheet geometry, too [26, 27]. Interestingly, there is a case of an Aβ peptide fragment proposed to adopt an antiparallel-, as well as a parallel β-sheet architecture. Aβ(16-22) measurements of dipole-dipole couplings demonstrated the occurence of a parallel and an antiparallel β-sheet fibril, depending on the pH value and acylation state [28–31].
By generating longer fragments of Aβ a shift towards parallel in-register structures could be detected. Aβ(10-35) for example displays a parallel in-register β-sheet arrangement [32, 33]. Likewise this holds true for Aβ(10-40), Aβ(1-40) and Aβ(1-42) [34–42].
Surprisingly, there is also an exception to this rule. The Iowa mutant of Aβ(1-40) (D23N) displays a stable parallel in-register supramolecular organization, whereas the antiparallel β-sheet fibril is thermodynamically metastable [43].
Due to the fact that early structural investigations of Aβ peptides were limited in resolution, later studies targeted to provide information about the β-sheet registry, as well as the complete molecular fibril structure. In addition, these studies were able to detect polymorphism on the molecular level, which is related to self-propagation in seeding experiments and toxicity to neuronal cell cultures [35–38]. A common structural motif of these fibrils, matching the measured constraints, is a hairpin-shape. A schematic cartoon of the hairpin-motif is displayed in figure 1.2. Here, The β-strands do not need to start directly at the first residue of the N-terminus, nor need to end with the last residue of the C-terminus. Nevertheless, the hairpin is formed by two adjacent and antiparallel β-strands (β1 & β2), connected by a loop region.

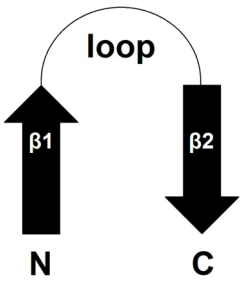

Figure 1.2: Schematic hairpin motif of amyloid fibrils

Remarkably, this structural motif is not only a characteristic of Aβ peptides, more-

over other fibril forming peptides, for example the WW domain, IAPP, β2m and Ure2p, display this feature [44–47].
In recent years, structures of completely labeled amyloid fibrils were published, showing the complete supramolecular organization of peptides, including side-chain orientations and sheet registry. Due to the higher resolution of these studies, several polymorphs of Aβ were described. Furthermore there is a clear trend recognizable towards analyzing brain-derived fibrils or using recombinantly expressed proteins.
One polymorph of brain-derived Aβ(1-40) fibrils consists of three monomers per layer, assembled in in-register parallel β-sheets, with a three-fold symmetry about the fibril growth axis [48]. The suggested structural model of the brain-derived fibrils clearly differed from in-vitro generated fibrils. The term in vitro in this case refers to the difference, if fibrils were seeded with sonicated brain extract or without, the latter being the in vitro definition. A published structure of recombinantly expressed Aβ(1-40) bearing the Osaka mutation (E22Δ), shows LS-shaped monomers, forming a parallel in-register dimeric fibril [49].
In reference to a reombinantly expressed Aβ(1-42) polymorph, T. Lührs et al. could solve the 3D structure of these parallel in-register fibrils, consisting of hairpin-shaped monomers [39]. Interestingly, they postulated a staggered arrangement of the monomers within one layer of the fibril. Unlike that, three more recent publications from different work groups, investigating Aβ(1-42) fibrils, found a planar arrangement of fibril layers, consisting of S-shaped monomers [40–42].
In addition, Quiang et al. studied brain-derived Aβ(1-40) and Aβ(1-42) fibrils, investigating the abundance of different polymorphs in dependance of the diagnosed disease type [50]. One predominant Aβ(1-40) polymorph could be found in each of two different types of AD, conversely there are at least two prevalent structures in the case of Aβ(1-42).
Several publications found a variety of different monomer and fibril structures, depending on the examined protein. There are two prions for example that are suggested to form a β-solenoid fibril, consisting of a triangular core [51, 52]. The structure of the monomeric α-synuclein fibril is determined by the Greek-key motif of the fibril core [53]. Two C-shaped monomers forming a dimeric fibril interface were detected in brain-derived tau fibrils [54]. To remove strain from the helical axes, caused by many twisted β-strand regions, the monomers ascend and do not lay planar within a fibril layer. The core structure of recombinantly expressed monomeric FUS-LC fibrils exhibits a pleated parallel in-register alignment of short β-strands [55].
To conclude, during the last 30 years we can clearly see a progress from structural models describing short synthetic fibril fragments, towards complete structures of full length brain-derived proteins, including microscopic and macroscopic measurements.

1.1.7 Short fibril fragments vs. full length fibrils

By extracting an amyloidogenic fragment out of the full-length protein, short fragments can form fibrils exhibiting similar morphologies to the corresponding full-length protein [32–34]. These fibril fragments were investigated by ssNMR, explained in detail in the previous chapter, but likewise they are suitable X-ray diffraction targets in the form of fibrils and microcrystals. Fibre diffraction studies found similarities between GNNQQNY-fibrils and microcrystals, derived from the full-length prion protein Sup35 [56–58]. In detail, both structures share a stable β-sheet rich architecture that allows for Congo red binding. The structure of the monoclinic microcrystal exhibited a parallel in-register double β-sheet, with a dry steric zipper interface. Nonetheless, GNNQQNY fragments form several polymorphic fibrils and crystals, making it necessary to investigate the structural details of crystals and fibrils. While the X-ray crystallography studies required large microcrystals, ssNMR measurements could be carried out with nanocrystals [59].
Here, two crystalline forms and three fibril forms were examined, showing chemical shift differences between each crystal and each fibril, as well as in between the two crystals and three fibril forms, respectively. In a subsequent study, distinct differences of the more complex fibril structures compared to the crystalline structures were found, though similarities could also be obtained [60].
Consequently, the crystals may be an adequate system to study the cross-β spine, however fibrils clearly deviate from these model systems. In addition, the longer a primary sequence gets, the more steric zipper-forming segments are available. More potential zipper locations enable the possibility of forming heterozippers from cross-complementary sheets. Furthermore, even unstructured regions of the protein might have an impact on the formation of fibril interfaces, for example by forming loops as described previously.
Since short fibril fragments tend to form self-complementary steric zippers, full-length proteins can form steric zippers assembling different β-strand regions within the protein (heterozippers). This effect can cause pleated β-sheet structures as observed in α-synuclein and FUS-LC for example [53, 55]. In addition, zippers formed by interdigitating layers have also been observed: the functional amyloid HetS forms a β-solenoid and the prion PrP^{Sc} is suggested to form a β-solenoid, too [51, 52, 61].
Being able to develop heterozippers leads to a higher diversity in the formation of fibril stabilizing elements, like hydrophobic clusters, salt-bridges and asparagine-ladders for example. Conversely, self-complementary fragments of microcrystaline Aβ(35-42) for example, can only form dimeric parallel β-sheets, as well as antiparallel β-sheets, each with dry interfaces [62].
On the contrary, dimeric full-length fibril structures of Aβ(1-42) can exhibit S-shaped monomers, whereas the monomer fold is governed by heterozippers form-

ing the dry intra- and intermolecular interfaces [41, 42].

1.1.8 Polymorphism

Aβ can form several distinct fibrillar polymorphs [63, 64]. Polymorphism is caused by structural heterogeneity on the microscopic length scale, yet also by varying arrangement of monomers and/or protofibril packing in mature fibrils on a macroscopic length scale. During the fibril preparation, the population of a certain polymorph within a heterogeneous mixture, can be tweaked by seeding [65]. Additionally, it has been shown that polymorphism is not exclusively an in-vitro issue, since different polymorphs were observed in brain-derived preparations, too [50].
Taking into account that at least five different Aβ(1-40) structures have been reported, we can conclude the dominant observed polymorph severely depends on the sample preparation conditions [66]. In the case of Aβ(1-40), a predominant fibril morphology can be selected by agitated or non-agitated growth conditions, leading to distinctly different conformations exhibiting different toxicities [37]. The toxicity is linked to the interaction of the fibrils with the cell-membranes and cell-surface receptors, which is determined by their structure.
It is high-likely that different Aβ assemblies can contribute to pathological effects in varying proportions, by membrane disruption, interaction with cell-surface receptors, impacting synapse function, induction of inflammation and/or generation of reactive oxygen species (ROS) [67–71].
On the whole, it can be ruled out that the molecular structure of a certain fibril is primarily determined by its primary sequence, since the growth conditions have significant effects on the structure.

1.2 Solid-state nuclear magnetic resonance spectroscopy

To gain structural information of insoluble and non-crystalline biological samples on an atomic length scale, Magic Angle Spinning (MAS) solid-state Nuclear Magnetic Resonance Spectroscopy (ssNMR) has successfully been applied [72–75]. Boundaries towards higher resolution of biomolecules, like amyloid fibrils, have been pushed with increasing field strengths, optimized sample preparation protocols and the design of new pulse sequences [76–78].
Since there is no rapid molecular motion, e.g. Brownian motion, like in solution-state NMR, anisotropic interactions affect ssNMR spectra. The two largest anisotropic interactions causing line broadening are chemical shift anisotropy (CSA) and homo- and heteronuclear dipolar couplings. Both interactions are explained briefly in this section, based on the detailled explanations in references [79–81].

1.2.1 Chemical shift anisotropy

By orienting solid samples in an external magnetic field (B_0), an induced field is generated by electrons surrounding the corresponding nucleus, causing partial shielding.
In solid samples, two separate processes contribute to the amount of shielding one nucleus experiences: The chemical environment of this particular nucleus and the orientation of the molecule within the external magnetic field. The detected chemical shift arises from the sum of the isotropic chemical shift (δ_{iso}) and the average of the spatial anisotropic chemical shift components (Eq. 2.1):

$$\delta_{obs} = \delta_{iso} + \frac{1}{3}\sum_{n=1}^{3}(3\cos\theta_n^2 - 1)\delta_{nn} = \frac{1}{3}\sum_{n=1}^{3}\delta_{nn} + \frac{1}{3}\sum_{n=1}^{3}(3\cos\theta_n^2 - 1)\delta_{nn} \tag{1.1}$$

From this equation one can see that δ_{iso} is the average over the three tensor main values (δ_{nn}). The spatial dependence is represented by the three angles θ_n describing the orientations between the three main axes of the CSA tensor and the external magnetic field.

1.2.2 Dipolar coupling

Neighboring spins can exchange polarization via dipolar couplings.
The dipolar coupling constant D depends inversely on the third power of the distance of the two coupling spins (r). Moreover, the gyromagnetic ratios of the nuclei (g_n) affect the coupling constant linearly. Equation 2.2 shows the formula to calculate the coupling constant, including the constants μ_0 (vaccum permeability) and $\hbar$ (reduced planck's constant).

$$D = \frac{\hbar\mu_0 g_1 g_2}{2\pi r^3} \tag{1.2}$$

The coupling constant D scales the magnitude of the dipolar coupling interaction in the dipolar coupling Hamiltonian $\hat{H}_D$. The dipolar coupling Hamiltonian $\hat{H}_D$ is proportional to the coupling constant and an angle-dependent term:

$$\hat{H}_D \propto (3\cos\theta_D^2 - 1) \cdot D \tag{1.3}$$

The angle θ_D describes the angle between the internuclear distance vector (r) and the external magnetic field.

1.2.3 Magic angle spinning

Since CSA and dipolar couplings are determined by the orientation of the nuclei within the external magnetic field, they lead to line broadening. Fortunately, this line broadening can be averaged out by spinning the sample in an angle of 54.7° with respect to the external magnetic field, called Magic Angle Spinning (MAS) (compare eq. 1.3) [82]. In one complete rotor revolution, anisotropic interactions are periodically modulated and averaged out.
If the anisotropic line-width of a signal is larger than the spinning speed, spinning sidebands arise in the recorded NMR spectrum. The sidebands appear at a distance of multiples of the spinning speed, with respect to the corresponding isotropic chemical shift. Hence, the number of sidebands can be decreased, if the same experiment is carried out with a higher spinning speed.
In the general case, where abundant spins and rare spins produce heteronuclear couplings, e.g. protons and carbons in biological samples, additional decoupling of the abundant spin is necessary. This is due to the fact, that the abundant spin might reorient itself during one rotor period, impeding the refocussing and causing line broadening.

1.2.4 Spin diffusion

Strong homonuclear couplings, due to dipolar couplings to other spins in a dense proton network in biological samples for example, exacerbate the direct acquisition of proton spectra in the solid state. Nonetheless, the proton network can be exploited to transport magnetization with spontaneous energy-conserving flip-flop transitions (spin diffusion). Flip-flop transitions can transfer polarization in between ^{13}C nuclei in proton-driven spin-diffusion (PDSD) experiments, which are explained in detail in [73].
However, a negative consequence of these transitions is homogeneous line-broadening, especially for strongly coupled spins like protons. Since homogeneous line-broadening cannot be refocused, strong decoupling sequences are essential during acquisition and evolution times of the experiments.

1.2.5 Dipolar recoupling

Averaging out dipolar couplings by MAS clearly improves the spectral resolution, as stated above. However, these couplings do comprise precious structural information, like the distance between the coupling spins. To reintroduce (recouple) these dipolar interactions, the periodical modulation of the anisotropic interactions has to be interfered with. There are several techniques targeting the recoupling of dipolar interactions, like SPC5 (supercycled permutationally offset stabilized C5), exemplified in reference [73].

1.2.6 Dynamic nuclear polarization

Dynamic nuclear polarization (DNP) exploits the much larger gyromagnetic ratio γ of the electron, compared to a ^{1}H nucleus. Both gyromagnetic ratios differ by a factor of 660, making it possible to theoretically enhance the sensitivity of a proton by this factor [84]. Electronic spin transitions can be excited from the thermal equilibrium by microwave irradiation, generated by a gyrotron for example. In continous wave DNP, there are four different transfer mechanisms: Overhauser effect, solid effect, cross effect and thermal mixing. Since the dominating mechanism depends on the choice of the temperature, the radical and its concentration in the sample, as well as the applied static magnetic field, we will focus on the dominating mechanism in our applied setup. In our work group, the bi-radical AMUPol is utilized, containing two electron spins which can couple with a nuclear spin to form a three-spin system. The resulting polarization transfer by the cross-effect will be covered in detail [85–87].
The cross-effect relies on a three-spin process between two strongly-dipolar coupled electron spins and one nuclear spin, first described by Kessenikh et al. in the 1960s [88–91]. To make it function properly, several experimental conditions have to be met [92–95]:

- The inhomogeneous electron paramagnetic resonance (EPR) linewidth has to exceed the nuclear Larmor frequency.
- The homogeneous EPR linewidth has to be small compared to the nuclear Larmor frequency.
- The frequency difference between the two electrons should match the nuclear Larmor frequency. In this case, two energy levels of the coupled system will become degenerated.
- The irradiation and saturation of the (high-field) EPR transition leads to positive NMR signal enhancement.
- The signal enhancement crucially depends on the electron-electron dipolar coupling and consequently on the distance of the two electrons.

Of note, the cross-effect scales inverse with the static magnetic field and relies on broad-line biradicals with a fixed electron configuration within, like AMUPol.

1.3 Recent structural studies of Aβ(1-42) fibrils

During the progress of this PhD-thesis, three ssNMR, one cryoEM and one EPR study of Aβ(1-42) fibrils were published.
In 2015 a cryoEM publication suggested a steric-zipper hydrophobic interface formed by the C-termini of synthetic Aβ(1-42) fibrils. Together with the assumption that β-sheets are parallel in-register a model was generated matching the electron density of the C-terminus [96]. In the structural model, parallel in register β-sheets were formed by two monomers packed face-to-face. However, the arrangement of the N-terminus remained elusive, due to a lower and less-defined density.
In the following year, an EPR study proposed a structural model of a recombinantly expressed Aβ(1-42) protofibril, exhibiting an S-shaped core-region [97]. The core region included three β-sheets, while the less ordered N-terminus was suggested to form one β-sheet, too.
A recently published ssNMR structure by Xiao et al., also showed only one protofibril consisting of one S-shaped monomer per layer, too [40]. Despite describing a similar monomer fold, the β-sheet locations clearly differed from the EPR and the ssNMR study. In contrast to that, the S-shaped fold of the monomer, described by Xiao et al., was later independently confirmed by Colvin et al., as well as Wälti et al. with ssNMR measurements (fig. 1.3) [40–42].
By including long-range and mass-per-length measurements of recombinantly expressed and uniformly labeled fibrils in the later ssNMR studies, a fibril consisting of two monomers could be described.
In total, both ssNMR structures show a fibril consisting of two monomers per layer with an interface formed by two intermolecular contacts between Met35-Leu17 and Met35-Gln15. The N-terminus in these polymorphs was detected to be flexible. The flat arrangement of the two monomers within a fibril layer was predicted by structure calculations in CYANA, based on the measured restraints. These structural features were the starting point for the measurements presented in this thesis and will be compared to our results.

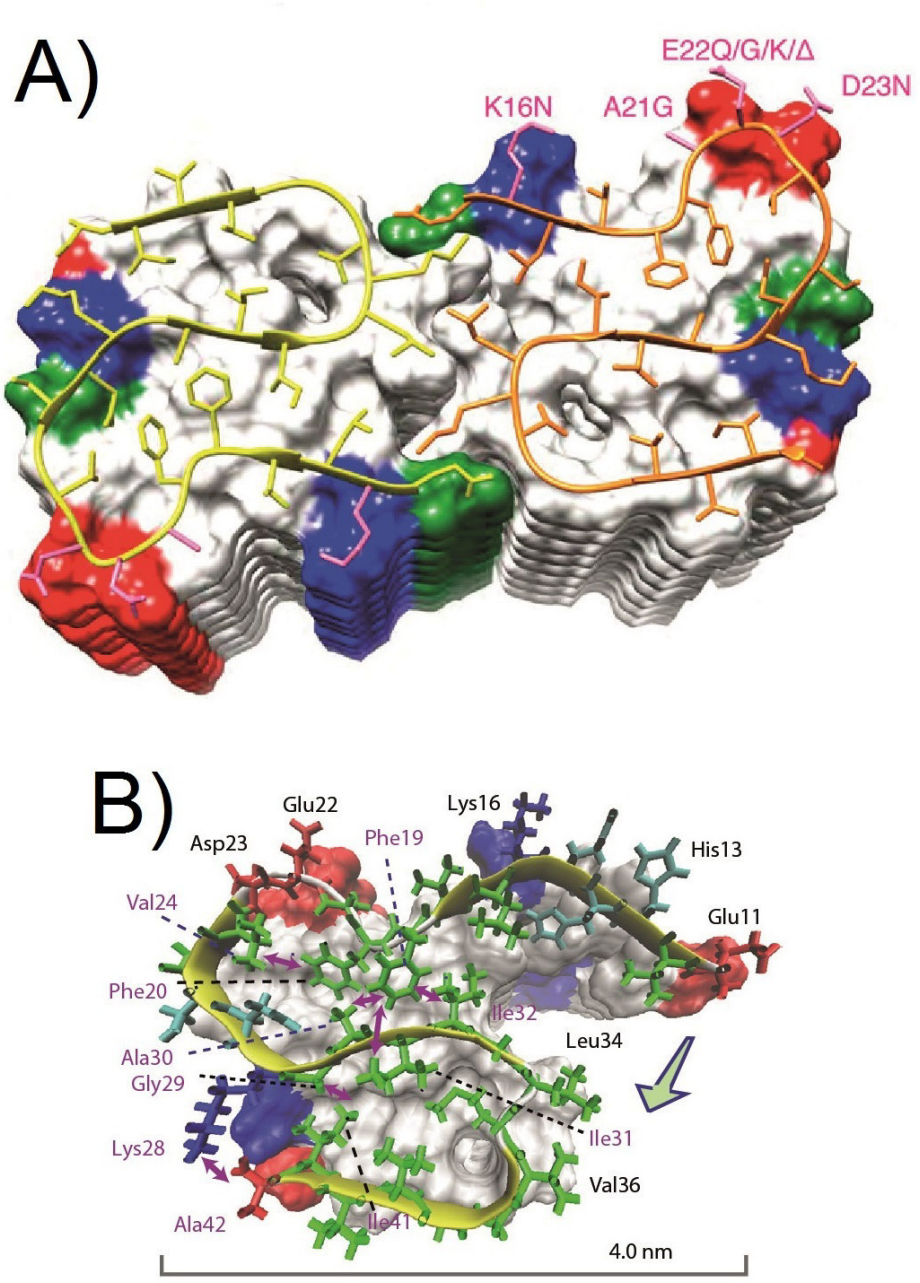

Figure 1.3: Published ssNMR structures of fibrillar Aβ(1-42). A) Dimeric fibril interface structure published by Colvin et al. and Wälti et al., respectively [41, 42]. Both structures expose two S-shaped monomers. The interface is formed by residues Gln15, Leu17, Leu34 and Met35. B) The fibril fold previously published by Xiao and coworkers [40]. In this study, selectively labeled samples were employed and there were no electron-microscopy measurements carried out. Due to this lack of information, a protofibril consisting of one monomer was proposed. Nonetheless an S-shaped monomer could be observed, with similar side chain orientations as in A).

2

Scope of this thesis

Since the aggregation of amyloidogenic proteins plays a crucial role in the development of several neurodegenerative diseases, knowledge of aggregate structures might yield a means to prevent or at least delay the progression of these diseases. Similarly to prions, amyloid proteins share the characteristic of altering the functional state of soluble proteins to an insoluble pathological state. The mechanism underlying the propagation of these pathological conformations can only be discovered on a microscopic length scale, since it seems to be hidden in the fibril structure itself.

Unfortunately, there are several structural models for the same amyloid protein, making it hard to find a common thread governing disease progression. Nonetheless, if we could find a common structural characteristic, detectable in all these different models, we could get a first indication on a superior shared structural relationship.

We set out to investigate a fibril structure in a bottom-to-top approach: first we decipher the molecular structure of the monomers within a fibril, to draw conclusions about the complete fibril architecture. Our tool of choice is ssNMR, due to its high-resolution capacity on an atomic length scale. In detail, we can observe the chemical shifts of the fibril atoms, yielding information about the secondary structure and protonation states. Moreover, there is the possibility to investigate side-chain side-chain contacts in long-range experiments, to model the arrangement of a basic unit within one fibril layer. Moreover, it is possible to determine the fibril rigidity and which residues are flexible.

To achieve this, a toolbox of pulse programs, software and sample preparation techniques has to be applied. Our model system of Aβ(1-42) fibrils is ideally suited for ssNMR measurements due to its intermediate length primary sequence. Additionally, it represents a large class of amyloidogenic proteins guaranteeing the transferability of the results to other amyloidogenic systems.

3

Material and methods

This section is partially taken from L. Gremer et al. (SI) with minor adaptations [98].

3.1 Aβ(1-42) sample

Recombinantly produced and uniformly ^{13}C-^{15}N-labeled Aβ(1-42) (95% purity) (with Asp1 as N-terminal amino acid residue) was purchased from Isoloid GmbH (Düsseldorf, Germany). Reverse phase high performance liquid chromatography (RP-HPLC) was applied leading to 98.5% purity. RP-HPLC was performed on a semipreparative Zorbax SB-300 C8 column (9.4 mm diameter, 250 mm length, Agilent, Böblingen, Germany) connected to an Agilent 1260 Infinity system with UV detection at 214 nm and a column temperature of 80°C. The mobile phase used was 30% v/v acetonitrile (ACN), 0.1% (v/v) trifluoroacetic acid (TFA) in water. Under these conditions uniformly ^{13}C-^{15}N-labeled Aβ(1-42) elutes as monomers [99]. Conversion of monomeric uniformly ^{13}C-^{15}N-labeled Aβ(1-42) to several μm long, unbranched fibrils occurred over several weeks by undisturbed incubation of the collected Aβ(1-42) fraction directly in the mobile phase as solvent at room temperature. After 8 weeks no monomeric Aβ(1-42) was detectable by analytical RPHPLC in supernatants of centrifuged (16,100 x g) fibrils.

3.2 Solid-state NMR experiments

3.2.1 Experiments

A detailed list of all experiments, including all acquisition parameters and pulse program codes, can be found in the supplement. Self-written pulse programs are explained in detail in this section. During all acquisition and evolution times high-power broadband proton decoupling with SPINAL phase modulation with an rf intensity of about 83 kHz was applied [100].

3.2.2 273 K measurements

Near room temperature Magic Angle Spinning (MAS) NMR spectra were recorded at Varian INOVA spectrometers at fields of 14.1 Tesla and 18.8 Tesla (correspond-

ing to ^{1}H resonance frequencies of 600 and 800 MHz, respectively), equipped with 3.2 mm standard bore triple-resonance MAS probe heads. The first series of experiments were performed on one uniformly ^{13}C-^{15}N-labeled Aβ(1-42) sample. The sample pellet containing $\sim$ 10 mg of protein was directly centrifuged into a 3.2 mm Varian rotor.

Additionally, to prove the reproducibility of our results, we filled a 3.2 mm Bruker rotor with a freshly prepared uniformly ^{13}C-^{15}N-labeled Aβ(1-42) sample, with the same procedure used for the Varian rotor filling. This procedure was also employed to fill the Aβ(1-42)-ThT-samples into a Bruker rotor. Furthermore, the pH of a pelleted fibril sample was shifted to 7 by adding 10 µl of a mixture of 0.25 $\frac{mol}{l}$ citric acid and 0.5 $\frac{mol}{l}$ Na_2HPO_4 (17.65%/82.35% v/v) to a 40 µl fibril pellet. Afterwards this sample was filled into a 3.2 mm Bruker rotor, using the same protocol as before. All samples in Bruker rotors were measured at a Bruker Aeon 18.8 Tesla spectrometer, corresponding to a ^{1}H resonance frequency of 800 MHz, equipped with a 3.2 mm wide bore triple-resonance MAS probe head.

3.2.3 Employed pulse sequences

For the acquisition of ^{13}C-T_ρ^1 and water-edited experiments, available PDSD and SPC5 pulse sequences had to be augmented by spin-lock pulses for the ^{13}C dimension or an echo sequence with subsequent longitudinal mixing for the proton dimension, respectively. All four applied sequences are presented in figure 3.1.
In the case of a ^{13}C-T_ρ^1 measurement, protons are excited with a 90° pulse first, with a subsequent CP step, transferring magnetization from ^{1}H to ^{13}C nuclei (fig. 3.1 a) and b)). Afterwards, the magnetization can evolve in an incrementation period (t_2) with decoupling of the proton channel in ^{13}C-T_ρ^1 PDSD experiment or it is spin-locked in the ^{13}C-T_ρ^1 SPC5 experiment. The incrementation in the SPC5 experiment happens after the excitation of double quantum transitions, unlike the PDSD where incrementation takes place directly after the CP. While the spin-lock is carried out, T_ρ^1 relaxation of carbon magnetization in the transversal plane occurs. The amount of relaxation scales with increasing spin lock times and is related to the rigidity or flexibility of the residues. ^{13}C-^{13}C recoupling is carried out via longitudinal mixing in the ^{13}C-T_ρ^1- and water-edited PDSD experiments, whereas double quantum (SPC5) recoupling is employed in the ^{13}C-T_ρ^1- and water-edited SPC5 experiments.

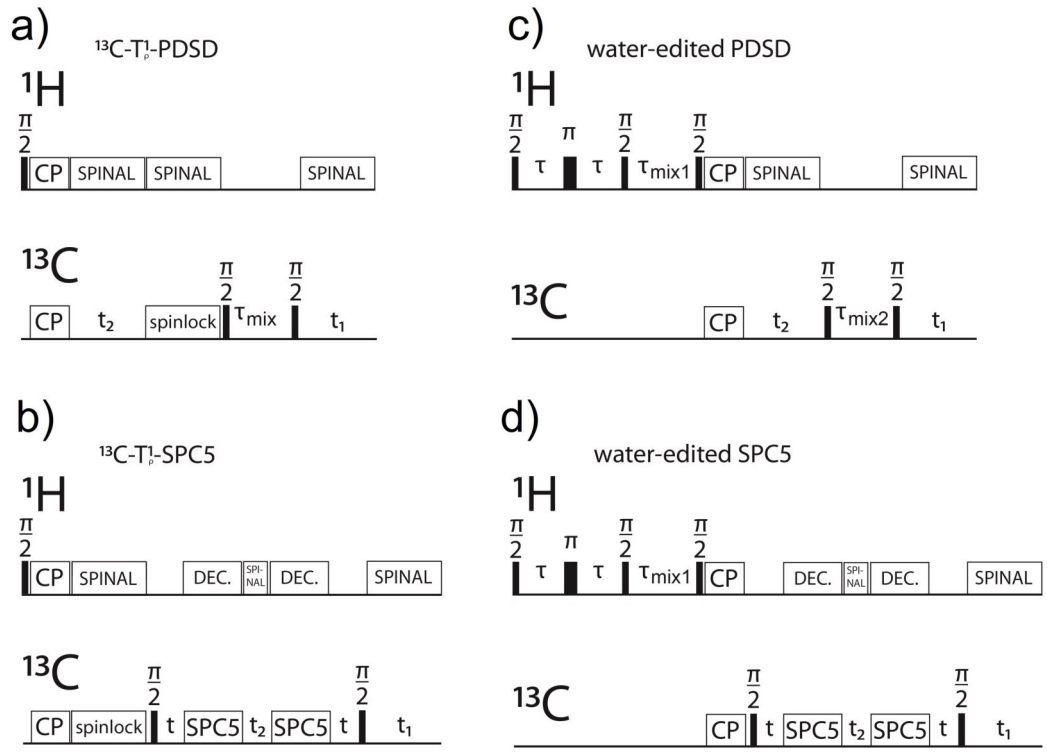

Figure 3.1: Overview of employed pulse sequences used in ^{13}C-T_ρ^1- and water-edited experiments. a) and b) showing ^{13}C-T_ρ^1 PDSD and SPC5 experiments, including the applied pulses. c) and d) display water-edited PDSD and SPC5 pulse sequences. PDSD and SPC5 sequences are constructed quite similar, only differing in the proton channel, or more specifically missing a spin-lock passage in the carbon channel. π indicates a 180° pulse, whereas τ represents a dephasing delay. t_2 and t_1 signify the acquisition times in the indirect and direct dimension, respectively. τ_{mix} indicates a longitudinal mixing passage in the pulse sequence. Two different decoupling sequences were used, continuous wave decoupling with Lee-Goldburg-offset during SPC5 recoupling (DEC.) and SPINAL decoupling during acquisition times and spin locks (SPINAL).

The main difference in the water-edited experiments is the echo sequence after the initial proton excitation. Protons with strong dipolar couplings will dephase faster during the dephasing time τ (500 µs). These protons cannot be refocused by the π pulse and will not contribute to the echo after another delay of τ, following the π pulse. Conversely water protons, which are mobile, can be refocused by the π pulse. Their polarization is subsequently diffused via longitudinal mixing and consequently repolarizes protons, which are strongly coupled to buffer-exposed fibril residues. Depending on the longitudinal mixing time τ_{mix1} (3 to 10 ms), more protons will get polarized. The complete proton magnetization is afterwards transferred to the carbon nuclei via CP. Finally, ^{13}C-^{13}C recoupling takes place.

^{13}C-T_ρ^1 experiments: PDSD-T_ρ^1 and SPC5-T_ρ^1 spectra were aquired as time series, starting with a spin lock time of 0 ms, as a reference spectrum and incrementing the spin lock time afterwards up to 10 ms. In all spectra, the same acquisition parameters were used. Afterwards, processed spectra were loaded into Sparky and all spectra were set to the same contour level and multiplication factor [101]. Subsequently, unambiguously assigned peaks were integrated with box sizes covering areas of 1 ppm x 1 ppm, shown in supplemental tables 4.1 and 4.2, respectively. Boxes were chosen to encompass the maximum without overlapping with other peaks. Due to a relatively low signal to noise ratio, some peaks vanished with increasing spin lock times. The integration of these peaks was not possible in Sparky, since there had to be a maximum above the noise level to mark a peak. Hence these peak integrals were set to the noise level (0). All peak integrals were normalized with the maximum measured integrated peak intensity for each acquired residue, to measure relative quantities.

Water-edited experiments: Water-edited PDSD and water-edited SPC5 spectra were aquired as time series, starting with a proton mixing time of 3 ms, as a reference spectrum. Afterwards the longitudinal proton mixing time was incremented up to 10 ms, apart from that all acquisition parameters remained the same. By using a T_2 spin echo on protons after initial excitation, only mobile water proton ^{1}H polarization remained, as previously described by Ader et. al, including the applied schematic pulse sequence [102]. Subsequently an incremented longitudinal proton mixing was carried out, whereas the diffused polarization was passed on to ^{13}C via cross polarization. Next ^{13}C- ^{13}C mixing was achieved by PDSD or by SPC5 recoupling. After the measurements, processed spectra were loaded into Sparky and all spectra were set to the same contour level and multiplication factor. Subsequently, unambiguously assigned peaks were integrated with box sizes covering areas of 1.8 ppm x 1.8 ppm (shown in supplemental tables 5.1 and 5.2). Boxes were chosen to encompass the maximum without overlapping with other peaks. All peak integrals were normalized with the maximum measured integrated peak intensity for each acquired residue, to measure relative quantities.

3.2.4 100 K DNP measurements

Since "DNP juice" [glycerol/D_2O/H_2O (60/30/10% v/v/v)] is usually employed in the literature, we prepared a similar sample with this glass-forming mixture to check, if it yields comparable results [124]. Since the fibrils were grown in a mixture of 70/30/0.1 % (v/v/v) H_2O/ACN/TFA, we had to maintain the ACN and TFA ratio to avoid structural rearrangements in the sample. To achieve this, we prepared a sample containing ~ 40 µl of fibril pellet dissolved in deuterated glycerol, deuterated ACN, D_2O, H_2O and TFA (40/30/20/10/0.1 % v/v/v/v) with an

AMUPOL concentration of ~ 3 m $\frac{mol}{l}$. Afterwards, this sample was centrifuged into a 3.2 mm sapphire DNP rotor.
Remarkably, we could detect a phase separation between deuterated ACN and deuterated glycerol, as we tried to prepare this DNP sample under native-like buffer conditions. This led to a higher concentration of AMUPol in the deuterated ACN phase. Hence, a second sample was prepared containing no deuterated glycerol. To pack the second 3.2 mm sapphire DNP rotor, the sample was pelleted (~ 40 µl) in a newly prepared washing buffer, containing D_2O/deuterated ACN/H_2O/TFA (60/30/10/0.1 % v/v/v/v). Afterwards, it was pipetted into a home-built rotor filling tool and then ultracentrifuged into the rotor (30 min at 100.000 g). Lastly the supernatant was discarded and the rotor was sealed with a silicon plug. The AMUPol concentration of the second sample was estimated to be ~ 5 m $\frac{mol}{l}$.
Both samples shared the same ratio of deuterated ACN, H_2O and TFA (30/10/0.1 % v/v/v).

3.2.5 Data analysis

Processing and assignment

All spectra were processed with nmrPIPE using squared and shifted sine-bell apodization [103]. 13C chemical shifts were externally referenced using an adamantane sample. The CH signal of adamantane was set to 31.4 ppm (corresponding to the DSS reference scale). ^{15}N chemical shifts were indirectly referenced to liquid NH_3 based on ^{13}C shifts and assigned in CCPN [104].

Peak integration

For peak integration, the "sum over boxes" method in Sparky was used [101]. Integration boxes were chosen to match the signal linewidths in the spectra, without making it necessary to re-center the peak maximum from spectrum to spectrum. In figure 3.2, a screenshot of the integration parameters and the integration box of Ser26-Cβ-CO is presented. All spectra within a series of measurements were set to the same contour level and multiplication factor. To measure the root mean squared deviation (RMSD) of the noise, the same signal free area was chosen in all spectra (30 ppm (y1)/110 ppm(x1) - 100 ppm (y2)/80 ppm(x2)) and the calculation was carried out using the "it" and "rt" command in Sparky. Next, the total number of points lying within an integration box was calculated. This was achieved by dividing the box length in the direct or indirect dimension in ppm by the spectral width (SW) of the direct or indirect dimension in ppm and afterwards multiplying the result with the number of points in the direct or indirect dimension, respectively:

1. Number of points in the direct dimension of an integration box:

$$n_{Box}^{dir.dim.points} = l_{\text{Boxlength}}^{dir.dim.}[ppm]/SW_{Spectrum}^{dir.dim.}[ppm] \cdot n_{Spectrum}^{dir.dim.points} \tag{3.1}$$

2. Number of points in the indirect dimension of an integration box:

$$n_{Box}^{ind.dim.points} = l_{\text{Boxlength}}^{ind.dim.}[ppm]/SW_{Spectrum}^{ind.dim.}[ppm] \cdot n_{Spectrum}^{ind.dim.points} \tag{3.2}$$

Both values, $n_{Box}^{ind.dim.points}$ and $n_{Box}^{dir.dim.points}$, were multiplied and the square root of the result was extracted. Afterwards, the square root of the product was multiplied with the root mean squared (RMSD) deviation of the noise found in the signal free area. This is due to the fact that the signal to noise ratio (SNR) increases with the square root of acquired scans. All values related to these calculations are given in supplement tables 4, 5 and 6. Finally the results were exported and plotted with Origin.

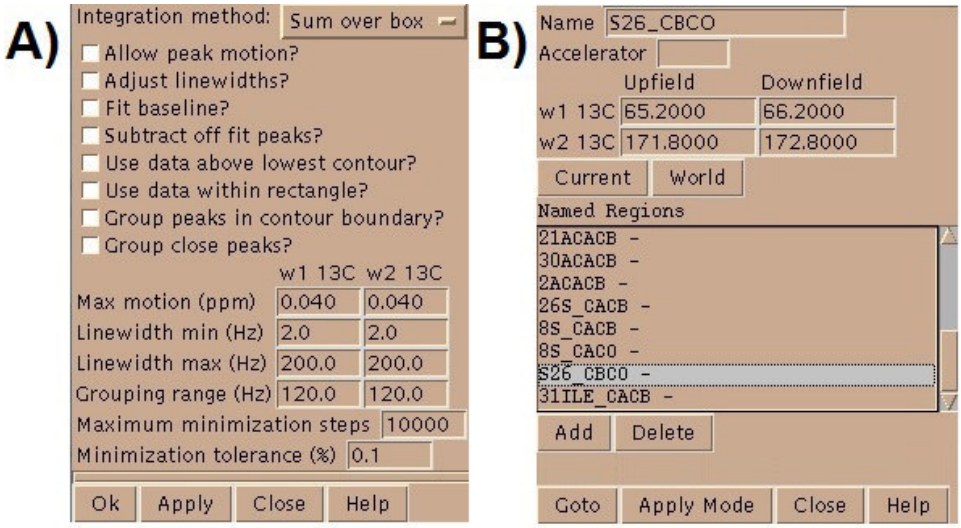

Figure 3.2: A) Sparky integration parameters determined with the "it"-command [101]. B) Integration box defined with the "rt"-command for all spectra, for example Ser26-Cβ-CO.

Discussion of decay and build-up times

Since the data points of the integrals were exported to Origin, a fitting function could be applied to estimate the decay times of the ^{13}C-T_ρ^1-experiments.
For the ^{13}C-T_ρ^1-measurements a mono-exponential fitting function could be applied to determine a characteristic decay time of the measured residue, analogous to the calculation of T^1 and T^2 decay times, respectively (eq. 3.3). The measured intensity $I(t)$ is equal to the product of a scaling factor A with the exponential function of $-t$ divided by T_ρ^1.

$$I(t) = A \cdot e^{bt} = A \cdot e^{\frac{-t}{T_\rho^1}} \tag{3.3}$$

$$\text{with} \quad T_\rho^1 = \frac{-1}{b} \tag{3.4}$$

The data points, which were plotted in Origin, were fitted in Origin, too.
For the mono-exponential plots, the function "Exp2PMod1" was used, which is equal to equation 3.3. The quality of the fits was measured with the R^2_{adj}-parameter (adjusted coefficient of determination), describing how well the regression fitted the data points (0-100 %).
In some special cases of water-edited experiments, the polarization of the protein protons can be assumed to be proportional to the square root of the proton-proton mixing time in the initial regime by reaching a state of saturation, due to a relayed magnetization transfer from the water protons [105–107]. However, the build-up is furthermore dependent on the diffusion constants of solvent-exposed and inward-facing residues, effects of the water-protein surface area and the protein volume. Since these variables have not been determined in this study, the build-up curves are only discussed quantitatively.

4

Results and discussion

This chapter is partially taken from L. Gremer et al. with minor adaptations [98].

In this thesis, the structure of recombinantly expressed and uniformly ^{13}C-^{15}N-labeled Aβ(1-42) fibrils is presented, based on cryo-EM and solid-state Nuclear Magnetic Resonance (ssNMR) measurements.
ssNMR results yielded the sequential resonance assignment and generated a secondary structure model based on the measured shifts compared to random coil values and TALOS-N [108]. Moreover, the complete N-terminus was observable, which has not been published before [40–42]. The analysis of the chemical shifts additionally led to the determination of protonation states. These results were reproducible with an independently prepared second sample, using the same preparation protocol. Since the cryo-EM structure yielded an overview of close inter-residual contacts, we conducted homo- and heteronuclear long-range correlation measurements. Afterwards, we focused on DNP experiments with the same uniformly ^{13}C-^{15}N-labeled sample. Here, we focused on comparing enhancement factors and resolution within two different static magnetic fields. Afterwards we acquired T_ρ^1 measurements to probe the rigidity of the fibril in the ambient temperature regime. Furthermore, we selectively polarized the surface-near residues of the fibrils, which are in close contact with the surrounding solvent. After these water-edited experiments, we continued with a ThT-binding study.
In the end, we also tried to investigate the behavior of the fibrils upon pH shift, whereas these data are complemented by on-going molecular dynamics simulations.

4.1 Aβ(1-42) fibril structure

Electron-micrographs revealed micrometer-long unbranched fibrils, where about 90 % of the fibrils had a rather invariable diameter of about 7 nm (fig. 4.1 and 4.2). These fibrils were used in a helical reconstruction procedure to compute a three-dimensional density to 4.0 $\AA$ resolution (figs. 4.3 - 4.6). The EM data were augmented by solid-state NMR and X-ray diffraction experiments, which were performed on identically produced fibril samples of recombinant uniformly labeled ^{13}C-^{15}N-Aβ(1-42) and show that the EM structure is representative of the sample. Full site-specific resonance assignments from 2D and 3D homo- and heteronuclear correlation spectra could be obtained by solid-state NMR for all 42 residues (vide infra). For most amino acid residues only one set of resonances was observed, indicative of high structural homogeneity and order.

The reconstructed fibril density and the atomic model (fig. 4.3) show two twisted protofilaments composed of Aβ(1-42) molecules stacked in a parallel, in-register cross-β structure. The separation between the parallel β-strands is well visible in the density. The peripheral β-sheets (residues 1–9 and 11–21) are tilted with respect to the fibril axis by $\approx 10°$ (fig. 4.4 C). Remarkably, the fibril does not show a C2 symmetry but instead an approximate 2_1 screw symmetry with a rise of 4.67 $\AA$, which is in excellent agreement with the strongest peak in the X-ray diffraction profile of 4.65 $\AA$ (fig. 4.7). Owing to this helical symmetry, the subunits are arranged in a staggered fashion (fig. 4.5 A). The interaction between the protofilaments is thus not true dimeric, but the subunits are stepwise shifted along the fibril axis (fig. 4.8). Such an arrangement has also been described recently for dimeric tau fibril structures [54].

A single Aβ(1-42) subunit forms an LS-shaped structure, in which the N-terminus is L-shaped and the C-terminus S-shaped (fig. 4.3 D). The C-terminus roughly resembles structures of a different polymorph of Aβ(1-42) determined recently by solid-state NMR alone, while the dimer interface is completely different (fig. 4.4, 4.9 and 4.11) [40–42]. In contrast to those NMR structures, the current structure shows the N-terminal part of Aβ(1-42) to be fully visible and part of the cross-β structure of the fibril. Secondary chemical shifts from our NMR experiments and the corresponding secondary structure calculation correlate well with the EM structure (fig. 4.17). Although we could not assign the long-range contacts unambiguously, all NMR cross-peaks, which are not due to sequential contacts, are in agreement with the cryo-EM structure (figs. 4.18 - 4.24). Recently reported chemical shift assignments of two brain seed-derived Aβ(1-42) fibril preparations differ from our chemical shifts suggesting different polymorphs [50].

Three hydrophobic clusters stabilize the subunit conformation: 1) Ala2, Val36, Phe4, Leu34, 2) Leu17, Ile31, Phe19, and 3) Ala30, Ile32, Met35, Val40. Because the hydrophobic clusters expand in the stacked subunits along the fibril axis, they

essentially contribute to fibril structure stability (fig. 4.5).
Combined analysis of NMR and cryo-EM data suggests salt-bridges between Asp1 with Lys28, Asp7 with Arg5, and Glu11 with His6 and His13 (fig. 4.9 A). The salt-bridges of Glu11 stabilize the kink in the N-terminal part of the β-sheet around Tyr10 (fig. 4.6 D). This structural feature has also been reported for fibrils of the Osaka mutant E22Δ of Aβ(1-40) [49]. In rat and mouse, which are animal species that are known not to develop Alzheimer's disease, His13 is replaced by arginine, which possibly prevents the formation of the kink around Tyr10.
Compared with previous Aβ(1-42) fibril structures, significant structural differences are observed in the turn region of residues 20 to 25, for example here only Phe19 but not Phe20 is facing the hydrophobic core (fig. 4.4 and fig. 4.11) [40–42]. This region, which forms two of the four edges of the Aβ(1-42) fibril, contains the sites of pathogenic familial mutations of Aβ: Flemish (A21G), Arctic (E22G), Dutch (E22Q), Italian (E22K), and Iowa (D23N). Furthermore, the effect of two mutants in the N-terminus at Ala2 can now be rationalized based on the fibril structure: A2T (Icelandic) might be protective against Alzheimer's disease, because threonine is more polar than alanine and could destabilize the fibril by disrupting the hydrophobic cluster Ala2, Val36, Phe4, Leu34 (fig. 4.4).
In contrast, A2V is pathogenic, which could be related to the fact that valine is more hydrophobic than alanine and would strengthen the hydrophobic interaction leading to increased fibril stability.
The staggered arrangement of the subunits has direct implications for fibril growth. Each monomer that binds to a certain fibril end sees the same interface, in contrast to a true dimeric interface (in the case of a C2 symmetry), where added monomers would alternatingly see either two identical binding sites or a curb preformed by the preceding subunit. The binding sites presented by the two fibril ends are different from each other, which leads to different binding pathways with possibly different energy barriers, and likely results in polarity of amyloid fibril growth (fig. 4.5) [109, 110]. The binding energy however has to be identical on both ends.
The subunits are not planar but instead the chain rises along the fibril axis from the N- to the C-terminus, forming grooves and curbs at the binding interface (fig. 4.5 C). We refer to the fibril ends as "groove" and "ridge", because β-strand 27–33 forms a ridge on the surface of one end of the protofilament, and a groove on the other end. The β-strands are staggered with relation to one another in a zipper-like fashion (fig. 4.5 and 4.9 C). For example, Phe4 of subunit i is in contact with Leu34 and Val36 from the subunit i-2 directly below. At both fibril ends, the binding site for addition of subunit i contains contributions of subunits i-1, i-2, i-3, i-4, and i-5, or i+1, i+2, i+3, i+4, and i+5, respectively, and very small, likely insignificant contributions from i-7 and i+7 (fig. 4.9 D). Therefore five Aβ(1-42) subunits are required to provide the full interface for monomer addition. For a fragment of six subunits, the capping subunits would have the same full contact interface as those

in an extended fibril. We define this structural element of six subunits as the minimal fibril unit.
The protofilament interface is formed by the C-termini, in contrast to previously determined solid-state NMR structures, where the C-termini are solvent exposed (fig. 4.11) [41, 42]. The interface is hydrophobic in the core and is formed by interactions between residues Val39 and Ile41 in subunit i with Val39 and Ile41 in subunits i+1 and i-1 (fig. 4.5 B). Moreover, the N-terminus of subunit i is close to the C-terminus of subunit i-3, and the salt bridge between Asp1 (subunit i), and Lys28 (subunit i-5) also stabilizes the interaction between the protofilaments (fig. 4.4 and 4.5).
Our structure agrees with a previously reported low-resolution cryo-EM structure of Aβ(1-42) fibrils, which was prepared under similar low pH conditions, but clearly differs from the polymorph observed by Schmidt et al. (111,96).
Our 4.0 $\AA$ structure provides detailed insight into the architecture of Aβ(1-42) amyloid fibrils and reveals a complete model with the backbone of all 42 residues and almost all sidechains visible and highly ordered. An in-depth illustration of a protofilament interface is achieved. The regular helical symmetry has direct implications for the mechanism of fibril elongation and results in distinct binding sites for monomeric Aβ, including contacts across different subunit layers. This high resolution structure will help to understand differences in pathogenic familial mutations, the molecular mechanism underlying fibril growth and potentially suggest ways to interfere with fibril formation and growth.

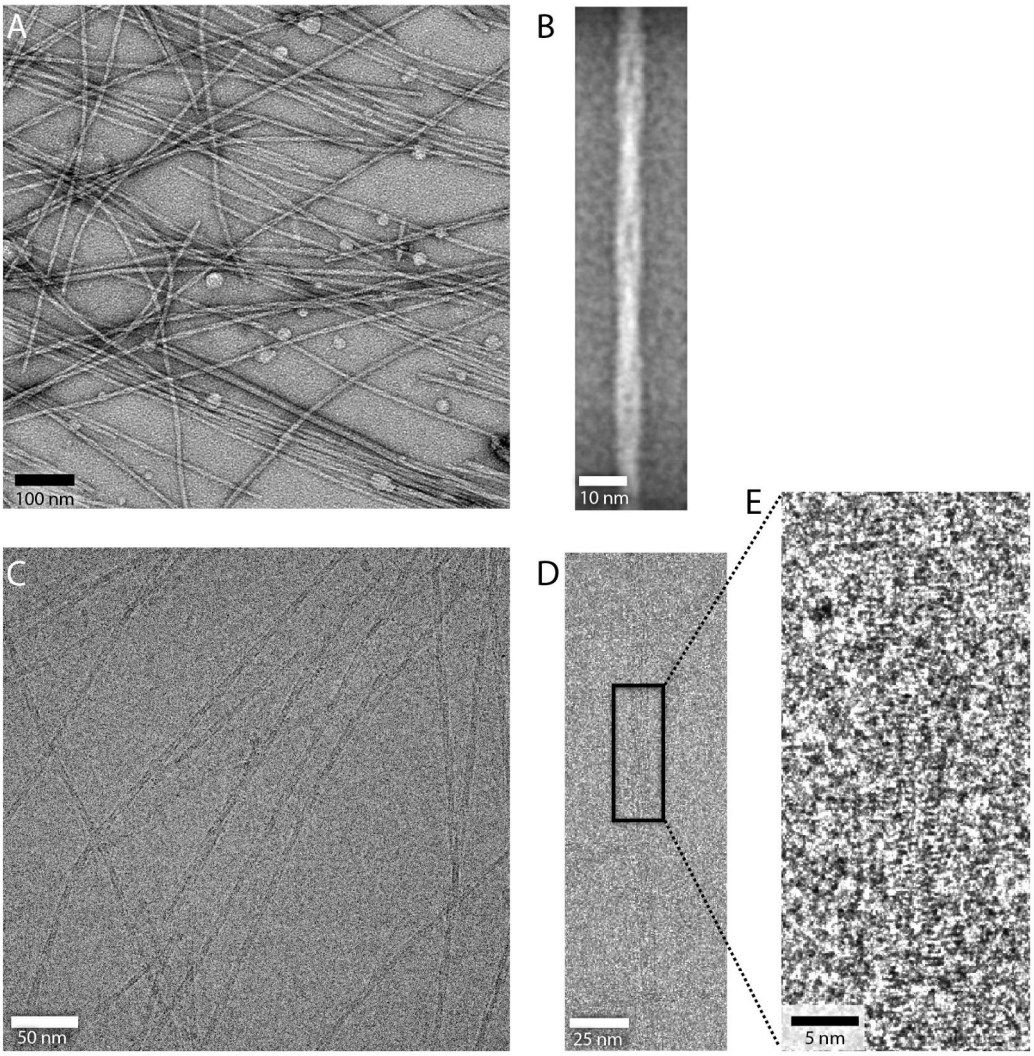

Figure 4.1: Representative micrographs of Aβ(1-42) fibrils. A) Micrograph of negative stained fibrils and B) average over three aligned fibril segments. C) Cryo-EM micrograph (defocus of 1.28 μm). In D) and E) typical density patterns from β-strands separated by ≈ 4.7 Å are visible directly in some of the micrographs at small defocus.

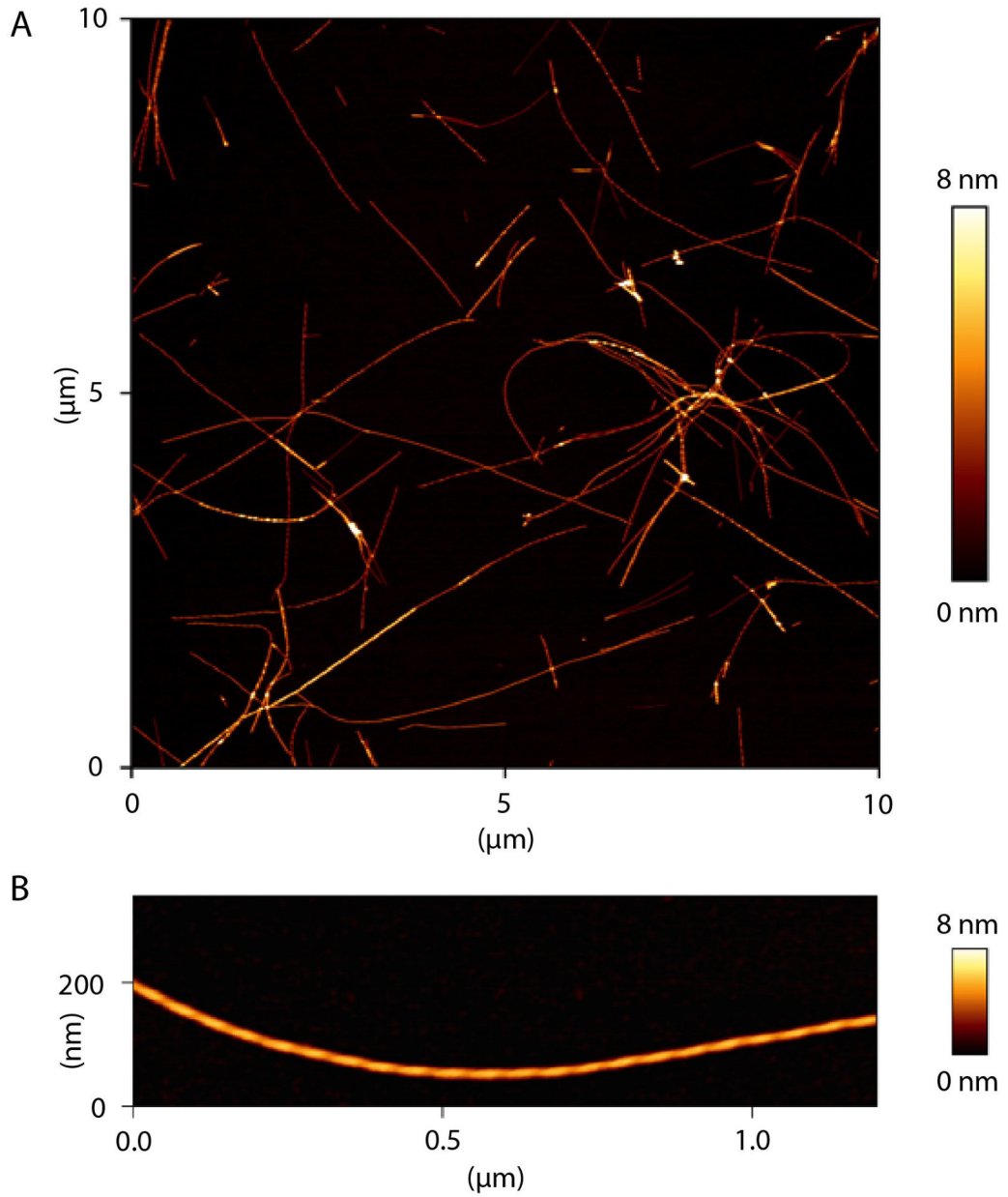

Figure 4.2: Atomic force microscopy of Aβ(1-42) fibrils. Fibrils shown in an overview A) and a representative fibril B), grown in 30 % ACN, 0.1 % TFA at a pH of 2.

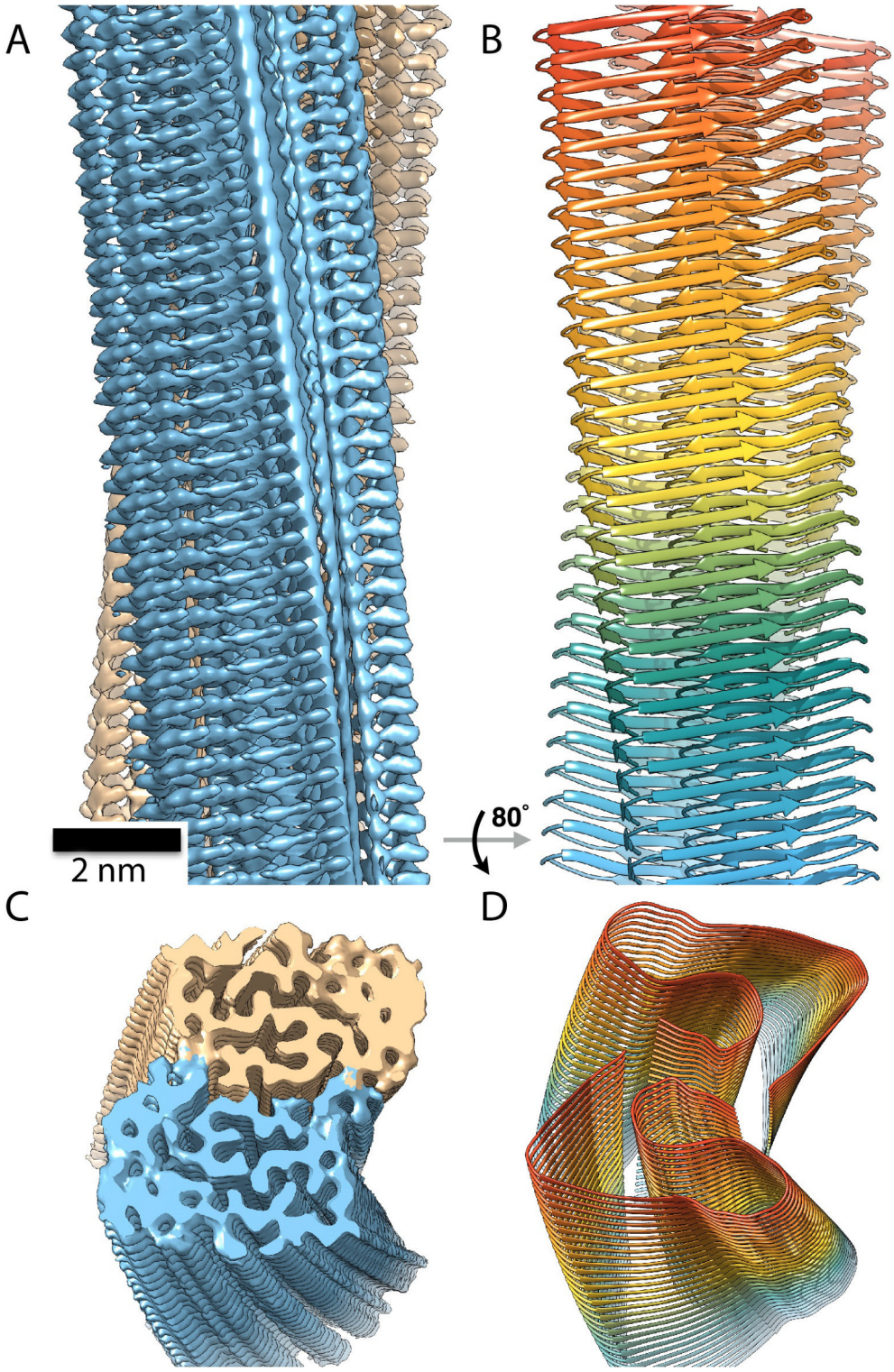

Figure 4.3: Aβ(1-42) fibril structure. A) 3D reconstruction from cryo-EM images showing density of two protofilaments (brown and blue) and the clear separation of the β-strands. B) Atomic model of the fibril with parallel cross β-structure. C) and D) show tilted views of the cross-section of the EM density and the backbone model.

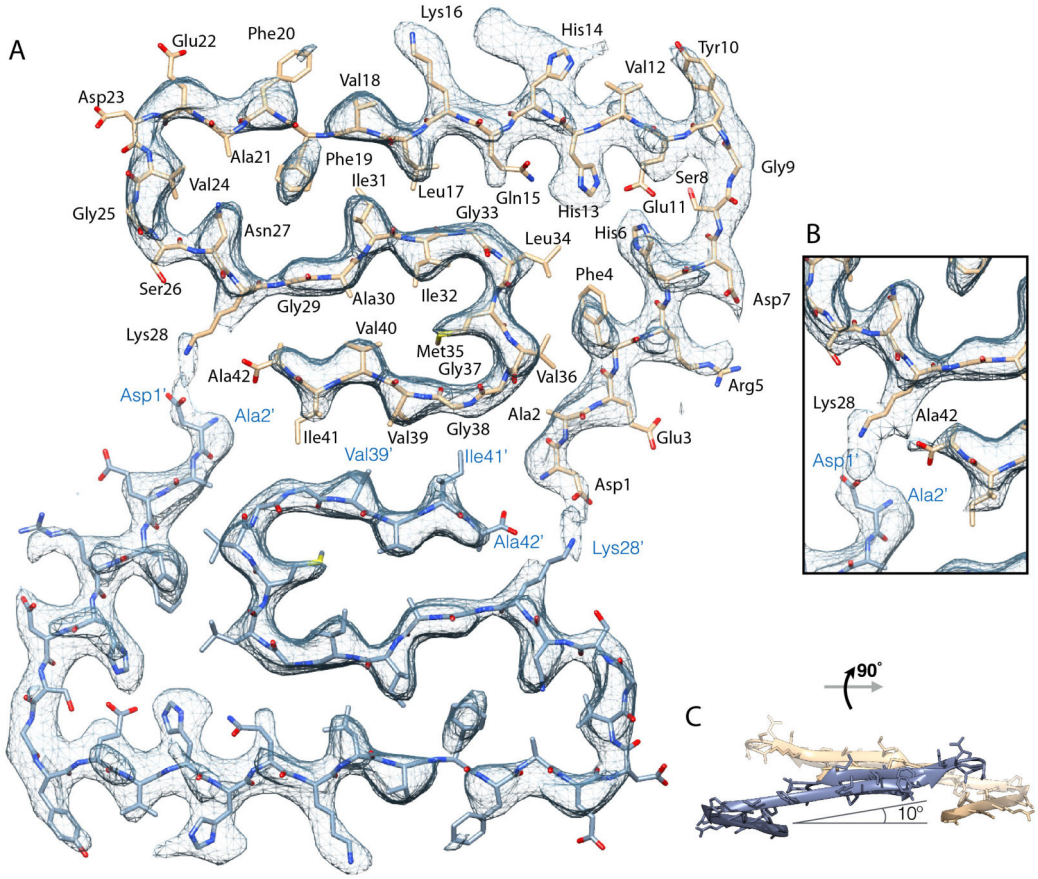

Figure 4.4: Atomic model and superimposed EM density of Aβ(1-42) fibril cross-section. A) Two subunits, one from each protofilament, are shown (blue and brown) together with the masked EM density map (at contour level of 1.5 σ). B) Detailed view of the interactions between the N- and the C-terminus and the side-chain of Lys28 (at contour level of 1 σ). C) Side view of the same two opposing subunits showing the relative orientation of the non-planar subunits. The large peripheral cross-β sheet is tilted by 10° with respect to the plane perpendicular to the fibril axis.

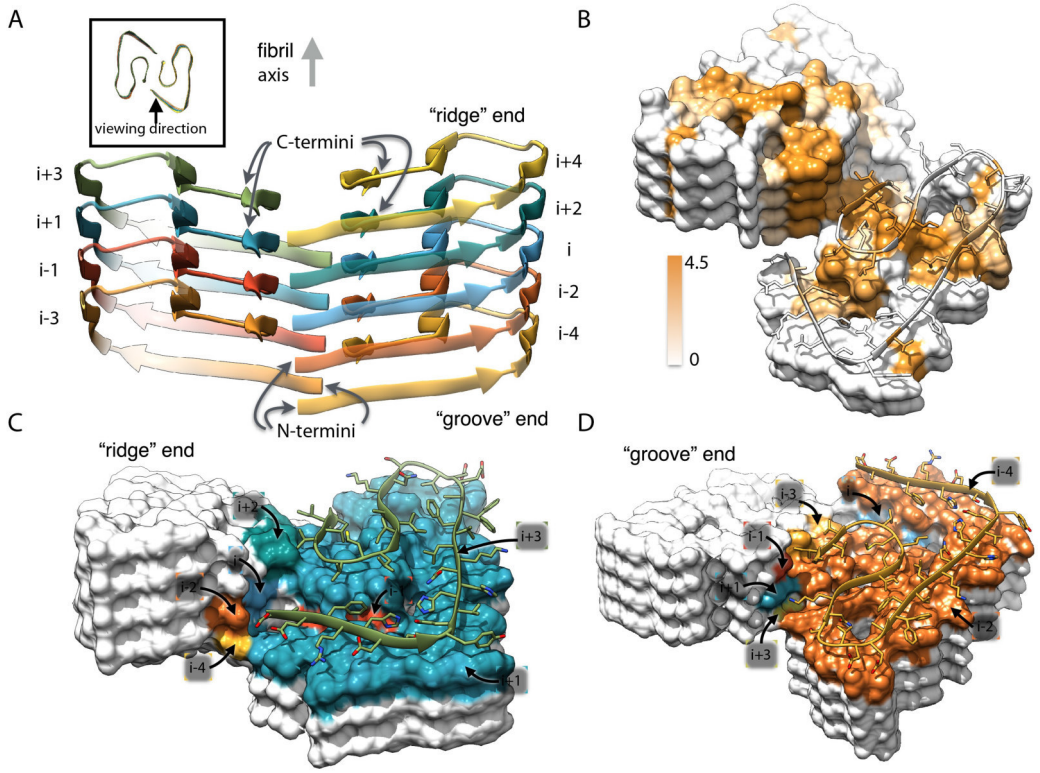

Figure 4.5: Details of the Aβ(1-42) fibril architecture. A) Side view of the atomic model showing the staggered arrangement of the non-planar subunits. B) Surface representation of a fragment of the atomic fibril model. Surface is colored according to hydrophobicity (Kyte-Doolittle scale) (gradient from brown (hydrophobic, 4.5) to white (neutral, 0.0)). View of the "ridge" C) and "groove" D) fibril ends. Only the contact surfaces of the subunits with the respective capping monomer (i+3 in C) and i-4 in D), shown as ribbon) are colored (color coding according to layer number, see A)).

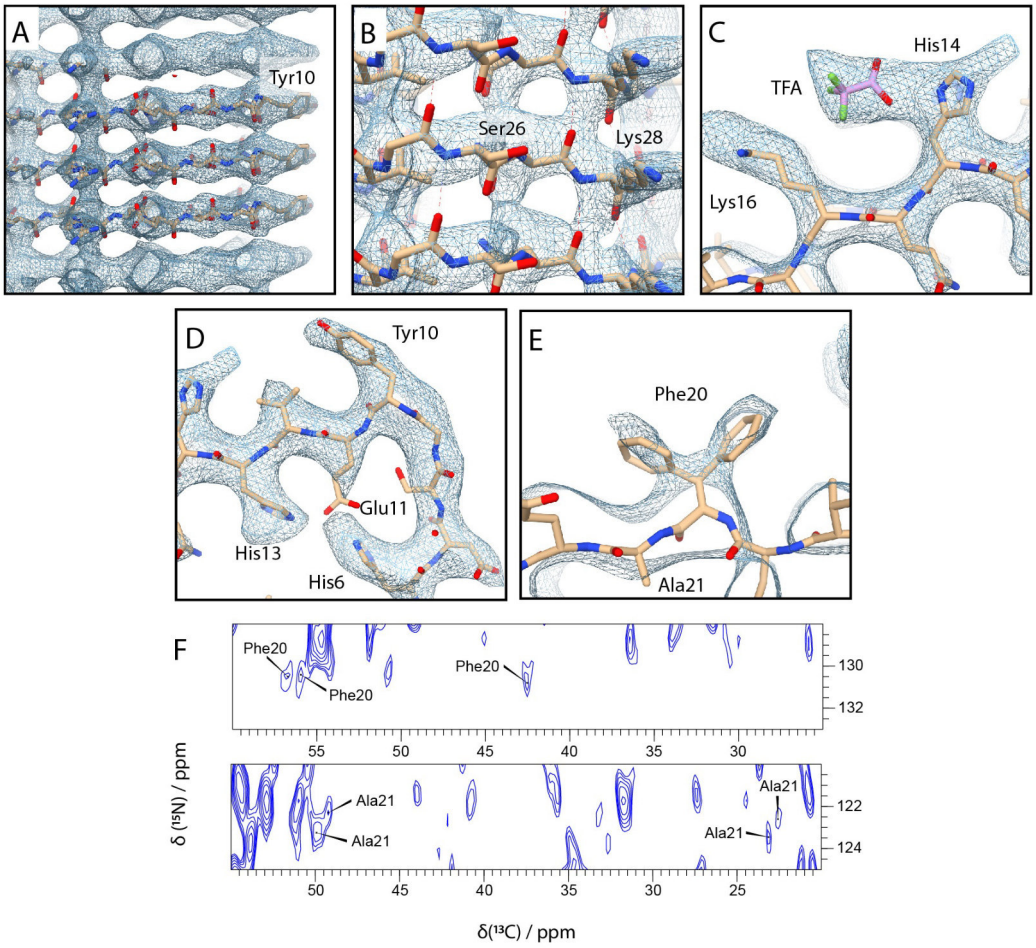

Figure 4.6: Details of atomic model and density of Aβ(1-42) fibrils. A) The density clearly resolves the separation of the individual β-strands along the fibril axis (density threshold 1 σ). B) The density of the β-strands between to Ser26 and Lys28 is not clearly separated and might indicate the presence of a (less populated) second conformer (density threshold 1 σ). C) The extra density between the two positively charged sidechains of His14 and Lys16 most likely is a negatively charged trifluoroacetic acid molecule (density threshold 1.5 σ). D) The kink in the backbone at the Tyr10 is stabilized by salt-bridges between Glu11 with His6 and His13 as supported by NMR. Rat and mouse have three residue substitutions compared to human Aβ: R5G, Y10F, H13R. Whereas residues 5 and 10 are solvent exposed, any replacement of His13 might hinder the formation of the kink around Tyr10 (density threshold 1.5 σ). E) The presence of two rotamers of Phe20 is visible in the density map (density threshold 1.5 σ), and (F) is also supported by the observed resonance doubling for Phe20 and for the neighboring residue Ala21 in the 2D NCACX correlation NMR spectrum.

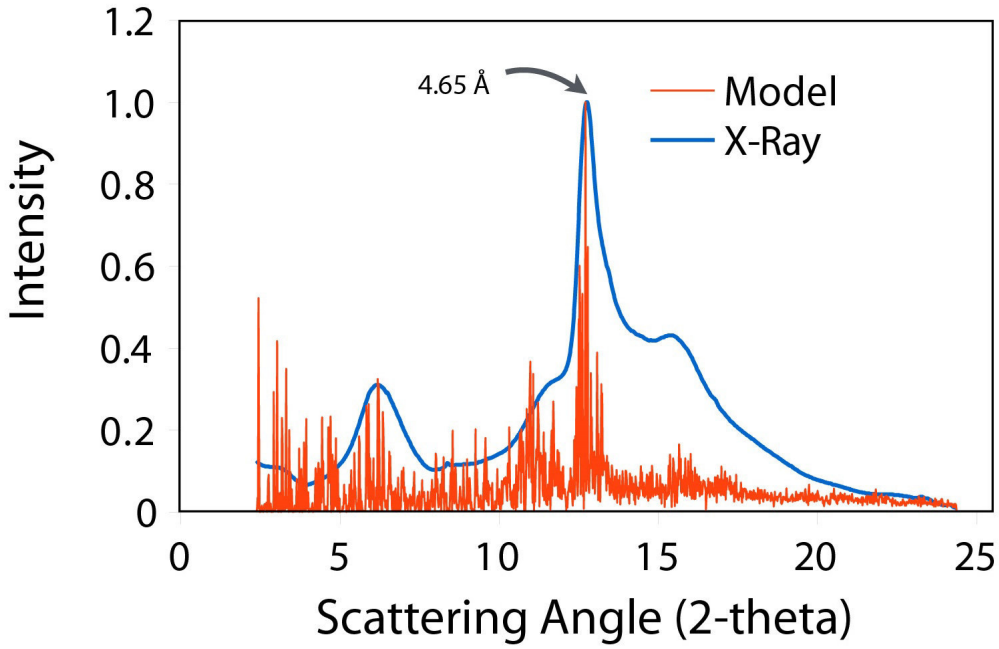

Figure 4.7: Comparison of the atomic model with X-ray diffraction data of Aβ(1-42) fibrils. Radially averaged intensity profile from an X-ray diffraction experiment of the Aβ(1–42) fibrils. The measured profile (black) fits well to the intensity profile calculated from the atomic model (red). Based on the helical rise of 2.335 Å, the shift along the fibril axis between neighboring subunit layers within one protofilament is 4.67 Å, which is in excellent agreement with the strongest peak in the X-ray diffraction profile of 4.65 Å. The radial diffraction profile simulated from the atomic model agrees well with the experimental diffraction profile, suggesting that our model is a good representation of the complete fibril ensemble.

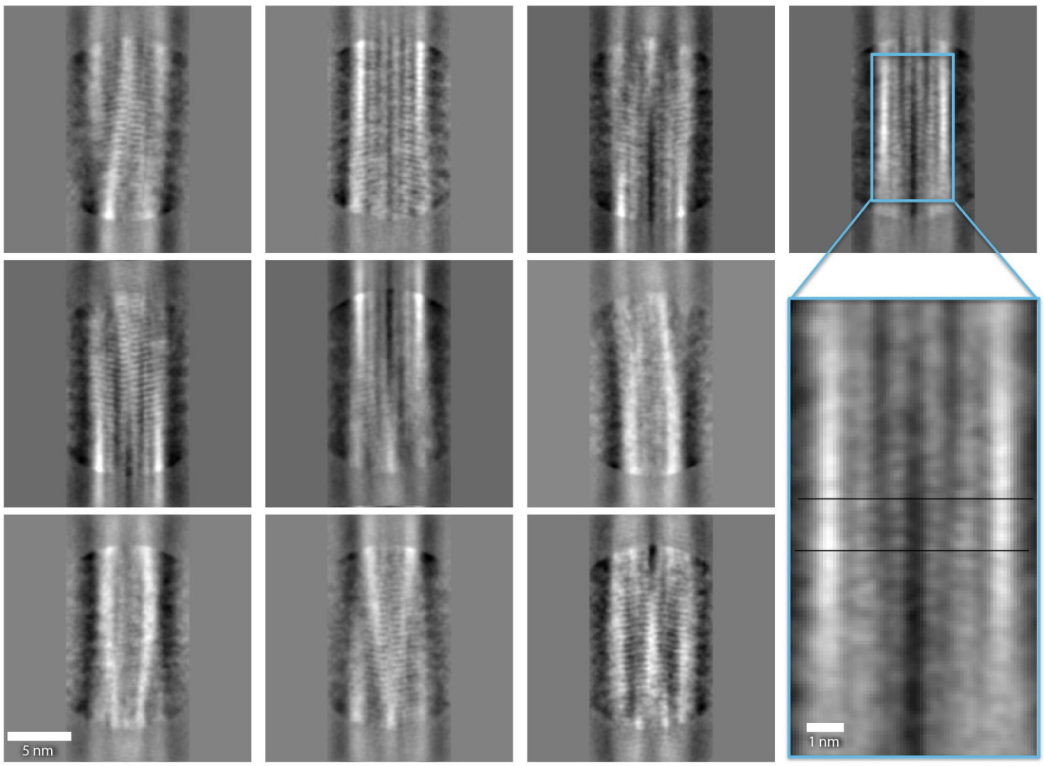

Figure 4.8: 2D Class averages of Aβ(1-42) fibrils. All 27,132 segments that were used for the final 3D reconstruction were used here for reference-free 2D class averaging with SPARX. The staggering of the subunits can clearly be seen (close-up view, bottom right).

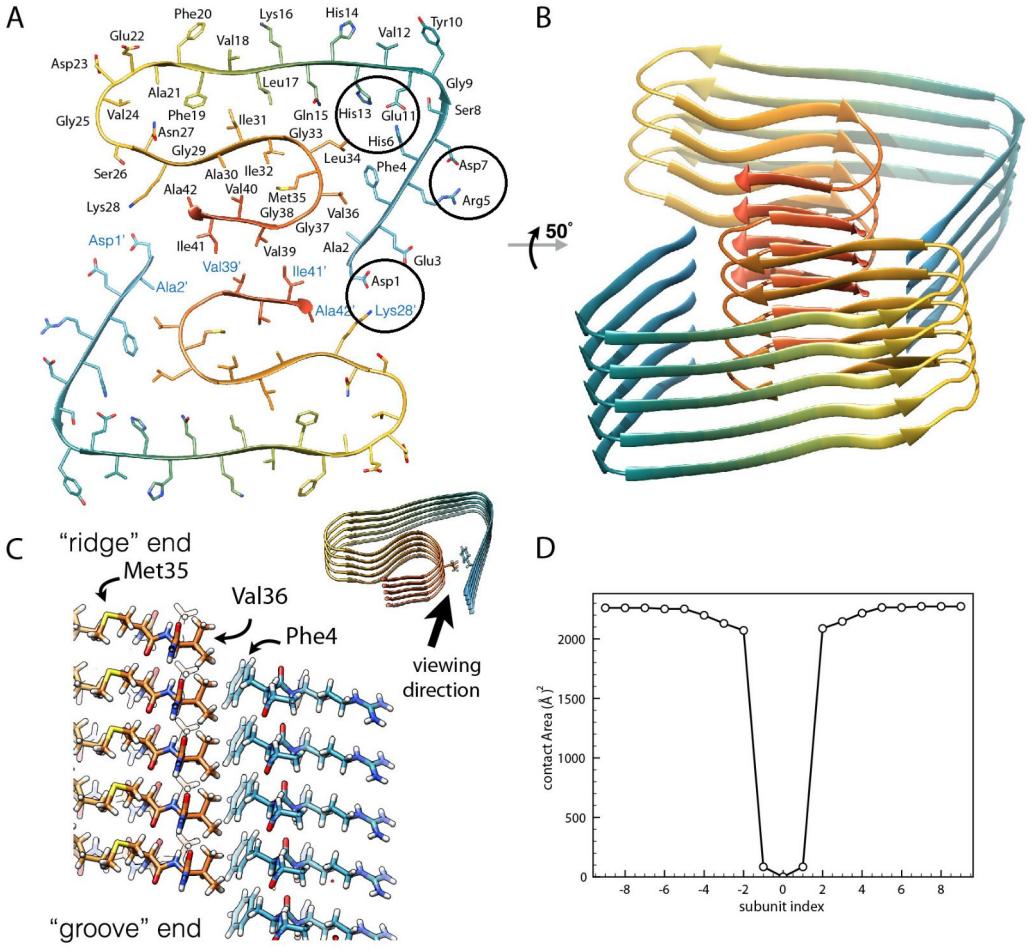

Figure 4.9: Views of the atomic model and contact area analysis of Aβ(1-42) fibrils. A) Cross-section of the Aβ(1–42) fibril showing two opposing subunits, one from each protofilament. Salt-bridge forming residues are marked with black circles. B) A view of the fragment of the fibril (comprising 9 subunits) that was used for the structure refinement (colored according to residue index). The buried surface area upon monomer addition of 2080 ± 50 $Å^2$ is the same for both fibril ends. C) Side view into one protofilament, showing the staggered arrangement of the hydrophobic residues Phe4 and Val36 within the core of the protofilament. The methyl-group of Met35 possibly forms a hydrophobic contact with the methyl-groups of Met35 in the subunits above and below along the protofilament. Similarly, the residue Gln15 and Asn27 in subunit i forms hydrogen bonds with the corresponding residues in the neighboring subunits i-2 and i+2 (the subunit labeling used here is illustrated in fig. 4.5), resulting in glutamine and asparagine ladders that further stabilize the fibril. D) The minimal fibril unit. We define the minimal fibril unit as the minimal number of subunits that provide any additional subunit the same contact interface as an extended fibril does. The plot shows the surface area of subunit i (subunit index = 0) buried upon successive addition of the respective subunit at the groove end (towards the left, negative subunit indices) or at the ridge end (towards the right, positive subunit indices).

The plot illustrates that in both potential growth directions five subunits already provide the full interface for the next (sixth) monomer addition, i.e., the minimal fibril unit has a size of six subunits. We note that this definition of a minimal fibril unit is based on the observed fibril structure, and that the size of the minimal fibril unit may be an isomorph-specific quantity.

4.2 Comparison to recent structural ssNMR models

In comparison to the latest ssNMR Aβ(1-42) fibril structures, there were several obvious differences to the structure presented in this thesis. First of all, we could detect a rigid N-terminus, being a part of the rigid fibril core. Admittedly there were several hints that it is not as rigid as the middle domain and the C-terminus as stated before, however all residues were assignable. On top of that, we could confirm the N-terminus contributed one β-sheet to the parallel in register β-sheet architecture of the fibril. Moreover, the side-chains in the N-terminus interdigitate in a steric-zipper-like fashion, supported by the finding of a hydrophobic inter-residual contact (Ala2-Val36).
With respect to the low pH value, we could detect protonated histidine ^{15}N side-chain shifts. In combination with the high likelihood of a deprotonated state of Glu11-Cδ, a salt-bridge between Glu11 and the positively charged side-chains of His6 and His13, stabilized the kink around Tyr10.
Starting from residue Leu17, our structure and the structures published by Xiao et al., Wälti et al., as well as Colvin et al., quite resembled a similar S-shape (see fig. 4.11) [40–42]. On the other hand, the side-chain orientations are different and moreover the interface region. This holds especially true for residues Phe20 to Val24 with significant chemical shift differences to previous studies (see fig. 4.10). In addition, we could detect peak doublings of Phe20, Ala21 and Ser26, indicating two steric side-chain orientations of Phe20 and slight polymorphism for Ser26, whereas both features were visible in the electron density. Since the side-chain of Phe20 is solvent exposed, which has not been described by Xiao et al., Wälti et al. or Colvin et al., the side-chain can adopt two rotameric states.
The interface region in our structure is determined by a hydrophobic self-complimentary single steric zipper. This makes it nearly impossible to distinguish between intra- and intermolecular contacts in PDSD or PAR spectra. Conversely in the two earlier published structures, the interface is formed by a hetero-zipper (Gln15, Leu17, Leu34 and Met35), making it more feasible to investigate intermolecular side-chain contacts. We tried to detect an intraresidual contact with a PAIN experiment (28Lys-Nζ-1Asp-Cγ), however due to degeneracies this did not work.
From the cryoEM data, the staggered arrangement of the dimers within one layer could be defined, establishing a relationship between a certain amount of Aβ(1-42) molecules and a complete fibril seed. Here, 6 Aβ(1-42) molecules are needed to provide the same contact interface as in a complete fibril.

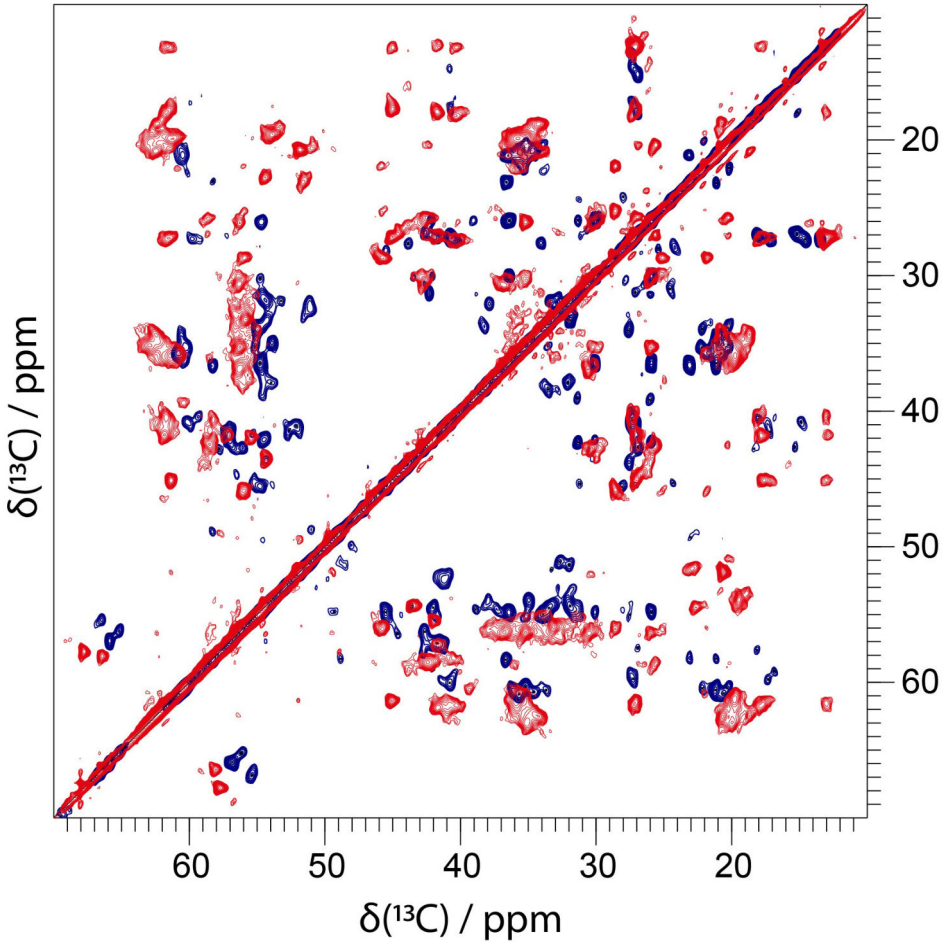

Figure 4.10: Overlay of 2D Proton-Driven Spin Diffusion (PDSD) spectra of the Aβ(1-42) fibril polymorph described by Wälti et al. (red) and the polymorph described in this publication (blue) (CCPN) [42, 98]. The red spectrum was recorded at a magnetic field strength of 14 T corresponding to a proton Larmor frequency of 600 MHz, a sample temperature of T = 0°C and a spinning speed of 13 kHz. The blue spectrum was recorded at a magnetic field strength of 18.8 T corresponding to a proton Larmor frequency of 800 MHz, a sample temperature of T = 0 ± 5°C and a spinning speed of 12.5 kHz. For homonuclear ^{13}C-^{13}C mixing, PDSD with a mixing time of 20 ms was employed in both experiments. Assignments of the blue spectrum are presented in fig. 4.12. Apparently, both spectra differ significantly, as visible by different resonance frequencies of the corresponding residues. Notably, chemical shifts of Aβ(1–42) fibrils described by Wälti et al., Colvin et al. and Xiao et al., largely coincided for residues 16-42, whereas the N-terminus was found to be flexible in these publications.

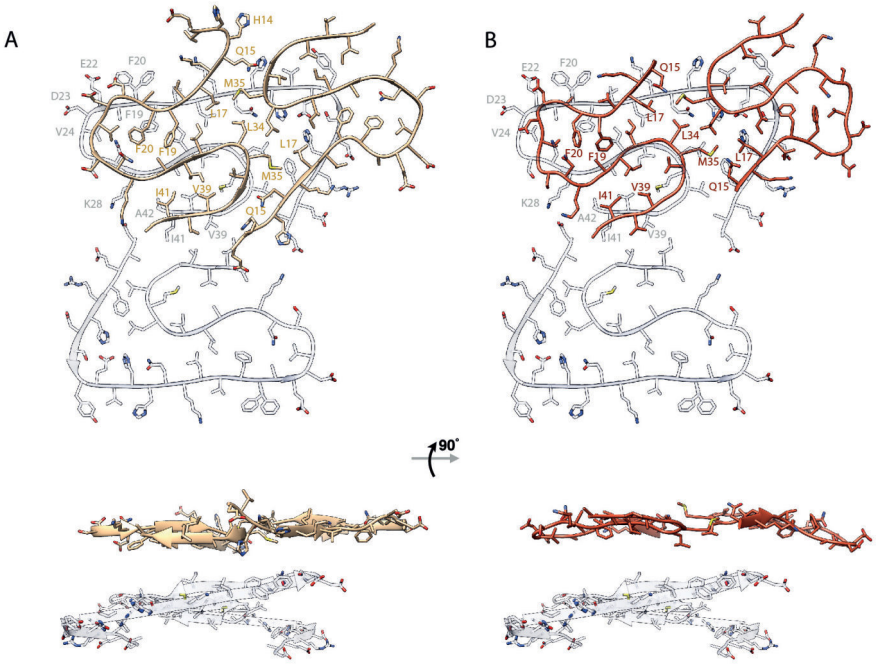

Figure 4.11: The C-terminal S-shape in the Aβ(1–42) fibril structure presented here (white) is similar to the NMR structures by (A) Colvin et al. (brown, PDB ID: 5KK3) and (B) Wälti et al. (red, PDB ID: 2NAO), however several sidechains point into different directions. The N-terminal region is not defined in the NMR structures. Side views are shown at the bottom, showing how the arrangement along the fibril axis is defined in the cryo-EM structure (white) as compared to the NMR structures (brown and red). NMR experiments cannot resolve the precise three-dimensional arrangement along the fibril axis, since they cannot assign intermolecular contacts to specific layers, the resulting models are therefore rather flat. The Cα-RMSD values (for residues 15-42 of a single subunit) between the model presented here and the structures by Colvin and Wälti are 2.9 $\AA$ and 3.2 $\AA$, respectively, while the structures by Colvin and Wälti are much more similar to each other (RMSD value of 1.8 $\AA$). Significant structural differences are also observed in the turn region of residues 20 to 25, which is also manifest in significant chemical shift differences observed in particular for residues Asp23 and Val24. While both Glu22 and Asp23 are exposed to the solvent also in the current structure, only Phe19 but not Phe20 is facing the hydrophobic core. The dimer interface is completely different in the NMR structures, where the interface is mainly formed by Gln15, Leu17, Leu34, and Met35, and the sidechains of Val39 and Ile41 make intramolecular rather than intermolecular contacts. The interfaces between one subunit with all neighboring (interacting) subunits in the different fibril models were analyzed with PDBePISA.

The estimated solvation free energy gain upon formation of the interface ΔG is -30.4 kcal/mol and -28.8 kcal/mol for the NMR structures 2NAO and 5KK3, respectively (we removed the disordered amino acid residues 1-14 from the 2NAO model). For the Aβ(1–42) fibril structure presented here, the ΔG is -36.3 kcal/mol. ΔG does not include contributions from hydrogen bonds or salt bridges and is therefore a measure for the hydrophobicity of the interface.

4.3 Chemical shift assignment and analysis

To probe the rigidity of the sample, cross-polarization based excitation schemes, which by dipolar transfer selectively excite rigid regions of the sample were complemented with an INEPT experiment where the through-bond magnetization transfer from ^{1}H to ^{13}C leads to selective excitation of mobile regions [112]. Whereas the INEPT spectrum recorded at a sample temperature of 20 ± 5°C did not show any observable signals (data not shown), in cross-polarization based spectra recorded at a sample temperature of 0 ± 5°C resonances for all 42 amino acid residues were visible. Line-widths in 2D spectra were 0.5 ppm in the carbon and 1.1 ppm in the nitrogen dimension. For sequential resonance assignment several types of multidimensional homo- and heteronuclear correlation spectra were recorded (table S1). To gather information about the ^{13}C backbone and side chain resonances, we performed proton-driven spin diffusion (PDSD) experiments with different mixing times from 20 ms to 750 ms (fig. 4.12, 4.13 and 4.18). At a mixing time of 200 ms, also sequential inter-residual correlations between side chain and backbone atoms could be obtained. To identify and confirm one-bond correlations, we recorded an additional homonuclear double quantum correlation experiment with SPC5-recoupling [113]. Inter-residual correlations could be confirmed in ^{15}N-^{13}C correlation spectra. Frequency selective polarization transfer from amide ^{15}N to ^{13}C CA or CO is achieved by specific CP [114]. Subsequently, polarization is transferred to the side-chain carbon atoms via DARR mixing or by a band selective homonuclear CP (BSH CP) with subsequent DREAM mixing [115–117].
Several NCACX and NCOCX-type spectra were used for a backbone walk (fig. 4.14). ^{15}N sidechain resonances of lysine, histidine and arginine residues could be identified from a 1D 15N CP spectrum. Long-range correlations could be obtained from a PDSD spectrum recorded with a mixing time of 750 ms as well as from a ^{13}C-^{13}C correlation spectrum obtained with Proton Assisted Recoupling (PAR) [118] (fig. 4.18 - 4.20). During all acquisition and evolution times high-power broadband proton decoupling with SPINAL phase modulation with an rf intensity of about 83 kHz was applied [100]. All spectra were processed with nmrPIPE using squared and shifted sine-bell apodization [103]. ^{13}C chemical shifts were externally referenced using an adamantane sample. The CH signal of adamantane was set to 31.4 ppm (corresponding to the DSS reference scale). ^{15}N chemical shifts were indirectly referenced to liquid NH_3 based on ^{13}C shifts and assigned in CCPN [104]. Secondary chemical shifts were referenced to acidic random coil shifts at pH 2.3 and 8 M urea [119]. We could assign all amino acids in the protein sequence (table S2, BMRB accession code 27212). Except for three residues (Phe20, Ala21 and Ser26), all amino acids only gave rise to one single set of resonances, underlining the structural homogeneity of the fibrils. Histidine ^{15}Nδ1 and ^{15}Nδ2 side-chain chemical shifts of 182.6 ppm and 176.1 ppm, respec-

tively, characteristic for biprotonated imidazole rings, were detetcted as expected at a pH value of 2 [120]. Despite the low pH, the relatively high Cγ NMR resonance shifts of the amino acid residues Asp1 and Asp7 suggest that the side chains of these residues are to a high degree deprotonated, which is consistent with salt bridge formation of Asp1 with Lys28, and Asp7 with Arg5 [121]. Likewise, the Cδ resonance shift of Glu11 indicates a predominantly deprotonated state, which supports the finding that this residue forms salt bridges with the positively charged side-chains of His6 and His13. A complete list of all assigned residues can be found in the supplement.

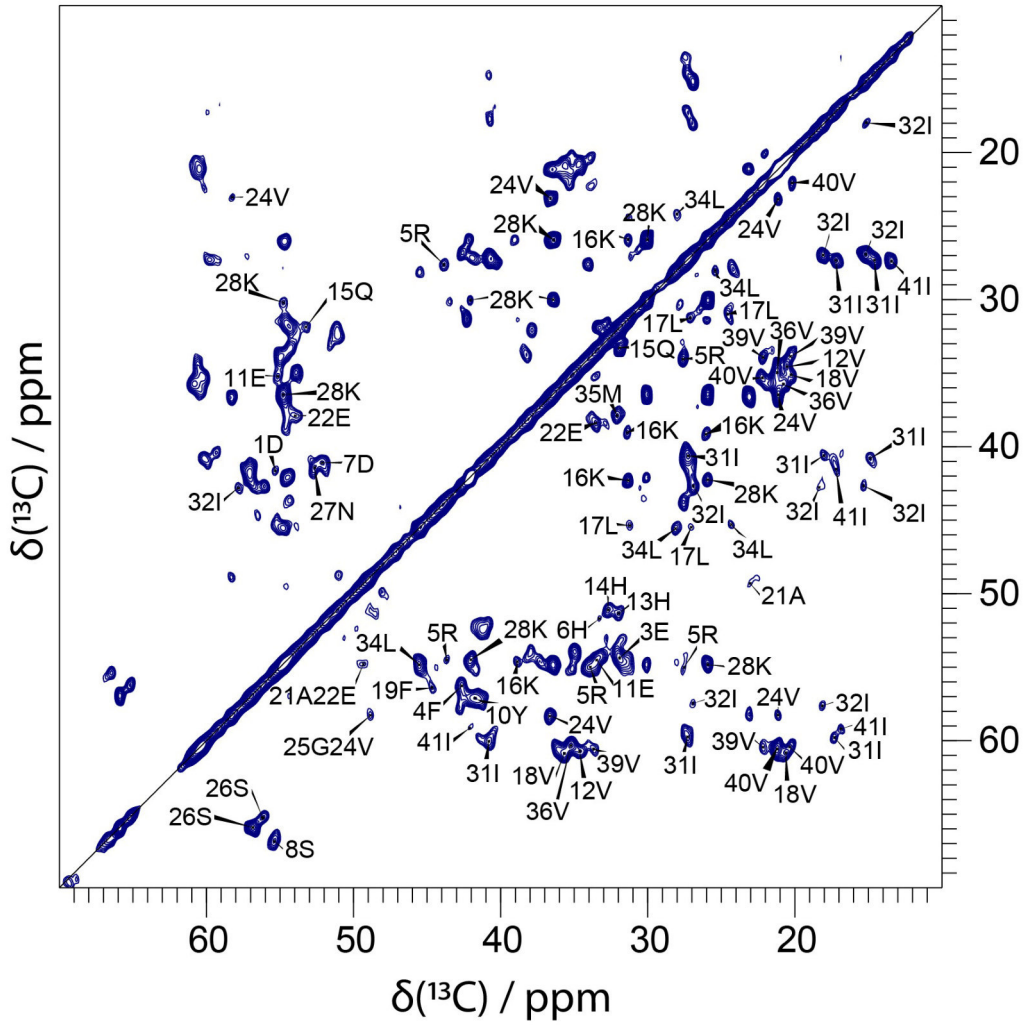

Figure 4.12: 2D Proton-Driven Spin Diffusion (PDSD) spectrum of fibrillar Aβ(1-42) (CCPN). The spectrum was recorded at a magnetic field strength of 18.8 T corresponding to a proton Larmor frequency of 800 MHz, a sample temperature of T = 0 ± 5°C and a spinning speed of 12.5 kHz. For homonuclear ^{13}C-^{13}C mixing, PDSD with a mixing time of 20 ms was employed. A squared and shifted sine bell function was used for apodization (shift of 0.3π). Assigned resonance peaks are labeled with respect to the corresponding residue, whereas the complete assignment resulted from several homo- and heteronuclear spectra.

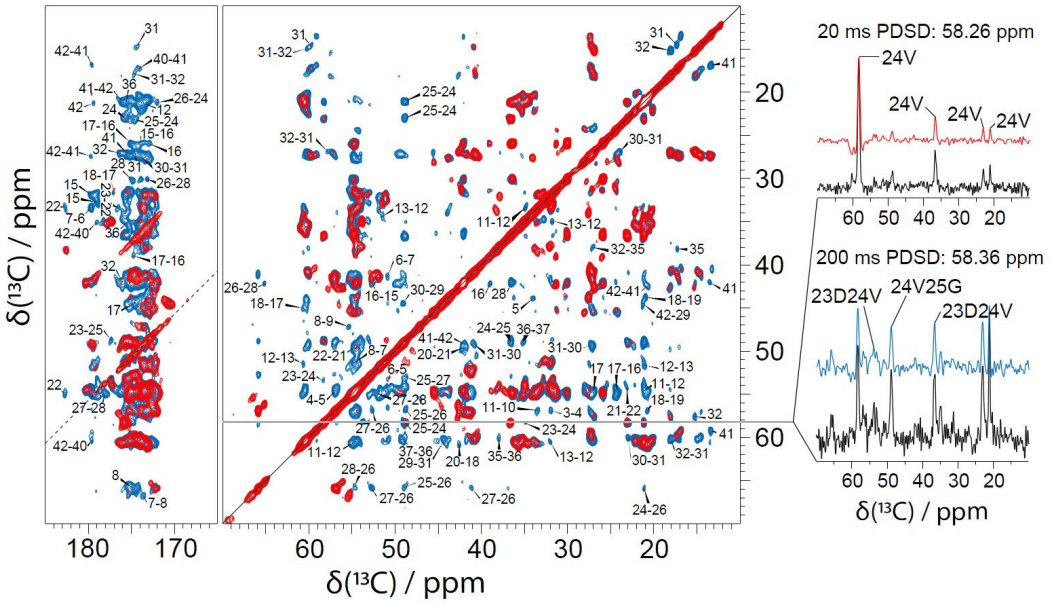

Figure 4.13: Overlay of Proton-Driven Spin Diffusion (PDSD) spectra of fibrillar Aβ(1-42) (CCPN). Both spectra were recorded at a magnetic field strength of 18.8 T corresponding to a proton Larmor frequency of 800 MHz, a spinning speed of 12.5 kHz and a sample temperature of T = 0 ± 5°C. For homonuclear ^{13}C-^{13}C mixing, PDSD with a mixing time of 20 ms (red contours) and 200 ms (blue contours) was employed. The spinning speed was chosen close to the rotational resonance (R2) condition and facilitates magnetization transfer between Cα and CO of neighboring amino acid residues. Sequential information is provided via cross-peaks of amino acids in close spatial proximity. A squared and shifted sine bell function was used for apodization (shift of 0.3π for the 20 ms spectrum and 0.28π for the 200 ms spectrum). Contour levels increase by successive factors of 1.2. Representative 1D slices taken from the processed (red and blue traces, respectively) and from the corresponding unprocessed (black traces) 2D spectra are displayed at 58.26 ppm for the 20 ms spectrum and at 58.36 ppm for the 200 ms spectrum.

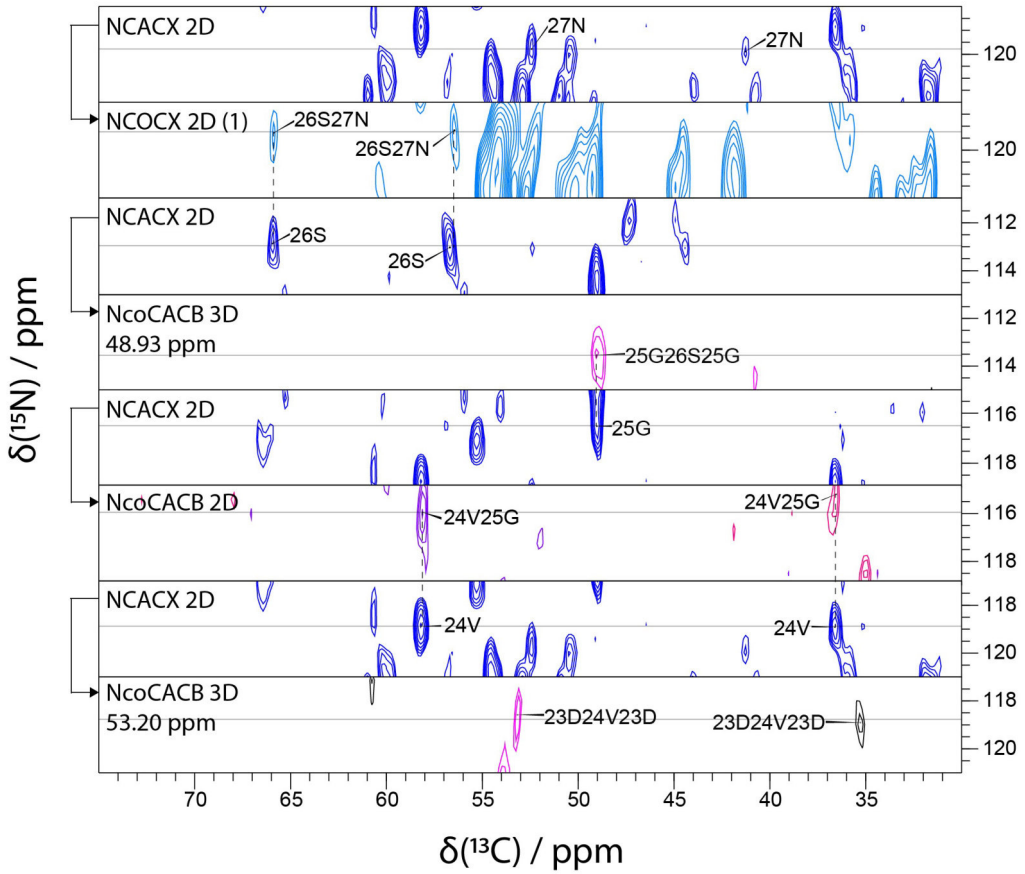

Figure 4.14: Representative strip plot of 2D NcoCX (light blue), 2D NcaCX (dark blue) and 2D/3D NcoCACB (purple/pink) spectra illustrating the resonance assignment of amino acids Asp23 to Asn27 (CCPN). All spectra, except for the NCOCX 2D, were recorded at a magnetic field strength of 18.8 T corresponding to a proton Larmor frequency of 800 MHz, a sample temperature of T = 0 ± 5°C and a spinning speed of 18 kHz. The NCOCX 2D was recorded at a magnetic field strength of 14.1 T corresponding to a proton Larmor frequency of 600 MHz, a sample temperature of T = ± 5°C and a spinning speed of 14 kHz. A squared and shifted sine bell function was used for apodization (shift between 0.28π and 0.33π.

4.4 Sample reproducibility

According to the protocol, described in section 3.1, a second sample was purified and fibrillated by Patrick Meckelburg under supervision of Lothar Gremer. However, for the second sample, we centrifuged ~10 mg sample pellet directly into a 3.2 mm Bruker rotor. Afterwards, we compared 20 ms PDSD and NCα spectra of both samples, shown in figures 4.15 and 4.16, respectively. Interestingly, there were some resonance signals showing up in the reproduced PDSD spectrum which were undetectable in the reference spectrum, but these signals reappeared with longer mixing times (200 ms).
Since the majority of the resonance signals of both sample preparations coincided, we could conclude both samples shared the same molecular conformation. Intensity changes could be attributed to the different 90° pulse lengths, as well as decoupling powers and CP conditions. In case of the NCα spectra, the spinning speed and the acquisition parameters were varied, too. A longer acquisition time in the indirect dimension of the reference NCα spectrum explains the enhanced resolution compared to the more recent spectrum of reproduced fibrils.
Nonetheless, it was not clear if the peak doubling of Phe20-Cα and Ala21-Cα was reproduced. Since the correlation signals of Phe20-N-Cα and Ala21-N-Cα exhibited broader line-widths in the spectrum of the reproduced fibrils, the peak doublings could not be resolved (fig. 4.6 and 4.16). Here, it would be necessary to repeat the measurement with more increments in the indirect dimension, to check if the peak doubling is still observable. Additionally, there was one most likely inter-residual peak detectable. The chemical shift value of 50 ppm was quite unique and indicated alanine Cα correlations. His-Cα correlations would have exceeded the assignment tolerance of 1 ppm and were thus less likely. For these reasons, the peak seemed to be caused by an inter-residual correlation between Lys28-N and Ala30-Cα.
On the whole, we could prove the reproducibility of our results, whereupon the fibril adopts a highly conserved structure.

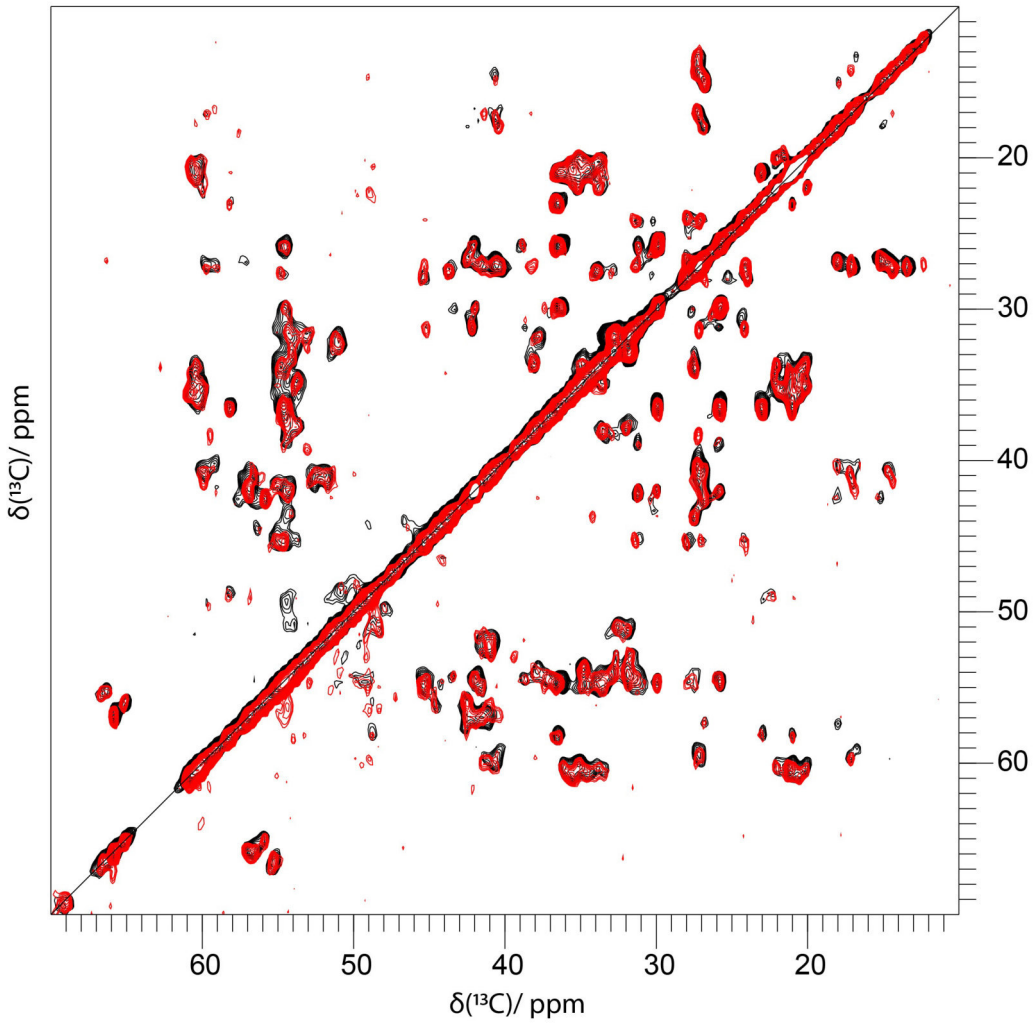

Figure 4.15: Overlay of Proton-Driven Spin Diffusion (PDSD) spectra of two samples of fibrillar Aβ(1-42) (CCPN). Both spectra were recorded at a magnetic field strength of 18.8 T corresponding to a proton Larmor frequency of 800 MHz, a spinning speed of 12.5 kHz and a sample temperature of T = 0 ± 5°C with the same amount of scans (80). For homonuclear ^{13}C-^{13}C mixing, PDSD with a mixing time of 20 ms was employed. A squared and shifted sine bell function was used for apodization (shift of 0.35π). The majority of resonance signals of both spectra coincide, with a slightly enhanced resolution in the spectrum of the second sample (red contours), related to a stronger decoupling field.

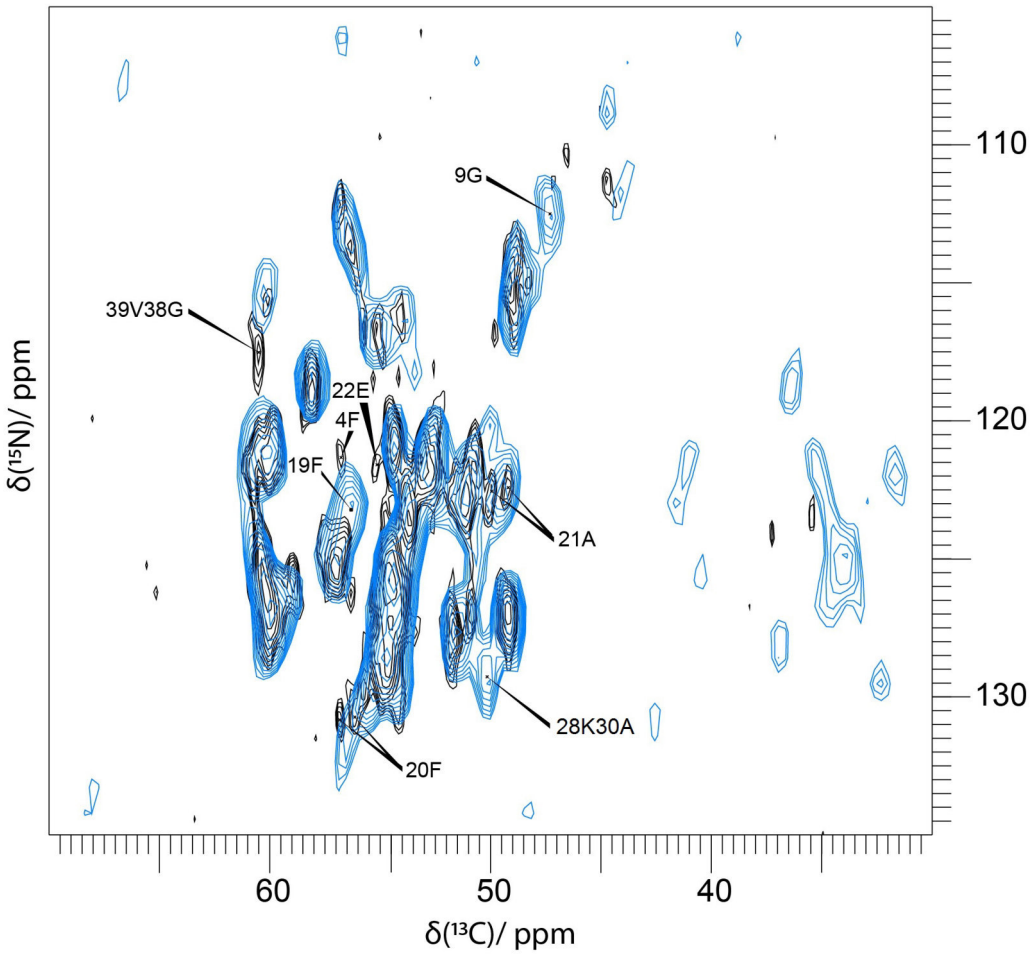

Figure 4.16: Overlay of NCα spectra of two samples of fibrillar Aβ(1-42) (CCPN). Both spectra were recorded at a magnetic field strength of 18.8 T corresponding to a proton Larmor frequency of 800 MHz, a sample temperature of T = 0 ± 5°C and a spinning speed of 18 kHz and 256 scans (black contours) or a spinning speed of 20 kHz and 736 scans (blue contours), respectively. For heteronuclear ^{15}N-^{13}C mixing, specific CP was employed in the spectrum with black contours and a Hartmann-Hahn CP in the spectrum with blue contours, respectively [114, 122]. A squared and shifted sine bell function was used for apodization (shift of 0.30π) for both spectra. Most of the resonance peaks of both spectra coincided, with a slightly enhanced resolution in the spectrum of the first sample (black contours). Thus, two peaks of Phe20-Cα, as well as Ala21-Cα were detectable in the reference spectrum. Remarkably, an inter-residual correlation signal was detected between Lys28-N and Ala30-Cα. Furthermore, additional peaks showed up in the blue spectrum, caused by the increased number of scans. Hence, even Cβ signals are observed in the blue spectrum, ranging from 30 to 40 ppm. Lastly, depending on the CP condition, the intensity of certain resonance peaks varied.

4.5 Secondary structure analysis

As mentioned before, secondary chemical shifts were referenced to acidic random coil shifts to guarantee comparability [119]. Since chemical shifts are highly sensitive towards molecular conformations, deviations from the random coil values are indicative for certain secondary structure motifs [123–125]. Differences were calculated with the following formula:

$$\Delta\delta_f = (\delta C\alpha_m - \delta C\alpha_{rc}) - (\delta C\beta_m - \delta C\beta_{rc}) \tag{4.1}$$

Here, δCx_m represents the measured Cx value, whereas δCx_{rc} stands for the random coil value. If $\Delta\delta_f$ of three consecutive amino acids exceeds a negative value of 1.4 ppm, the residues are most likely to adopt a β-strand conformation. As expected for an amyloid fibril, there is a high amount of β-strand content in the primary sequence (table 4.1). Surprisingly, this is also true for the N-terminus. Interestingly, in other studies investigating the structure of other Aβ(1-42) fibril polymorphs, these polymorphs exhibited an unstructured N-terminus [40–42].
In total, there were 6 predicted β-strands, based solely on the secondary chemical shifts (navy arrows) (fig. 4.17). A secondary structure calculation by TALOS-N resulted in 4 β-strands [108]. Protein backbone torsion angles were empirically predicted and a measure of β-strand probability was displayed, indicating the position of the β-strands in TALOS-N (shown in the table, vide infra). There were no structural predictions for the first and last amino acid of the peptide. If the β-strand probability of a certain residue exceeded a threshold of 75%, this certain residue was considered to adopt a β-strand conformation. The threshold values were indicative of four β-strands, where the peripheral β-strands of the secondary chemical shift analysis were confirmed. The C-terminal β-strand, predicted by TALOS-N, comprising residues Lys28 to Val36, seemed to be shorter in the cryoEM structure. Since there was a kink starting at residue Leu34, the β-strand had to be shorter to fit into the electron density. Besides, this particular β-strand was divided into 3 smaller ones in the secondary chemical shift prediction, because of the glycines at position 29 and 33. Interestingly, the β-strand at the very end of the C-terminus was also conserved in the TALOS-N prediction. The same applied for the cryoEM based secondary structure calculation, where both N-terminal β-strands and the last C-terminal β-strand remained. On the contrary to the TALOS-N prediction, the β-strand comprising residues Asn27 to Gly33, predicted by the cryoEM data, took into account the two kinks at Ser26 and Leu34. On the whole, the three independent secondary structure calculation methods yielded agreeing results for the positions of the β-strands in the fibril.

1				5					10					15					20
D	A	E	F	R	H	D	S	G	Y	E	V	H	H	Q	K	L	V	F	F
33	75	82	96	97	92	66	49	82	93	98	98	98	97	96	98	99	99	97	96

				25					30					35					40		
A	E	D	V	G	S	N	K	G	A	I	I	G	L	M	V	G	G	V	V	I	A
94	93	86	74	44	33	82	92	89	88	97	98	98	98	99	99	92	68	88	99	97	33

Table 4.1: β-strand probability of residues in Aβ(1-42) fibrils in percentage predicted by TALOS-N. Residues beneath the threshold of 75% are colored in red.

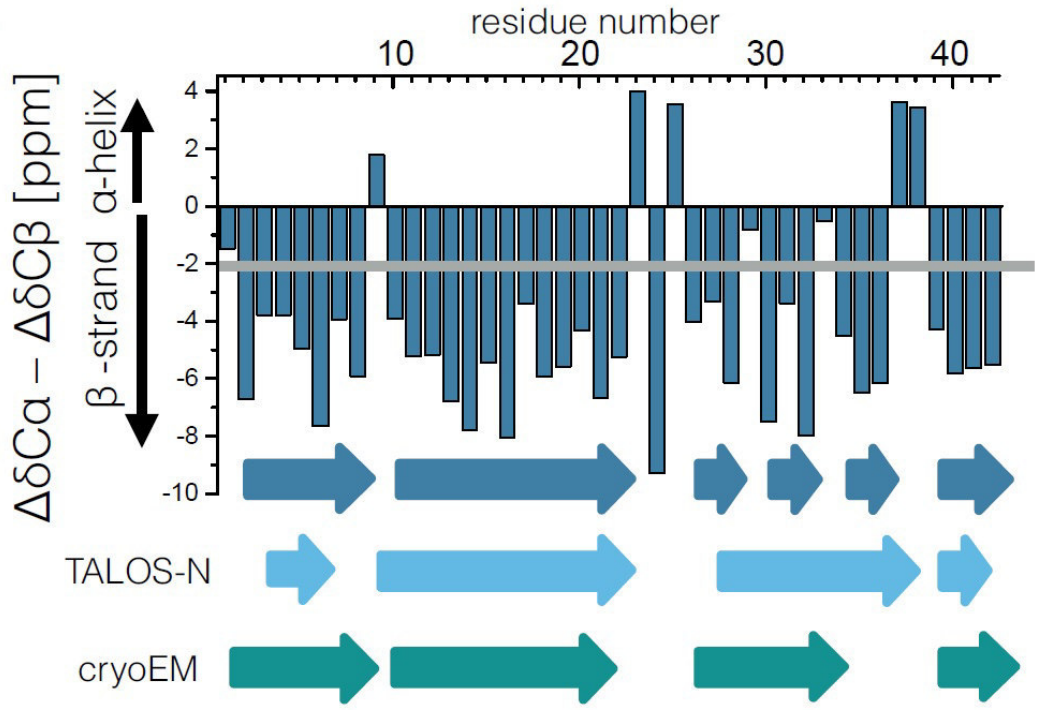

Figure 4.17: Secondary structure plot based on ssNMR, TALOS-N and cryoEM data. Secondary chemical shifts calculated from assigned resonance shifts and random coil values predicting β-strand regions (difference exceeds -2 ppm) are shown in dark blue. For Gly residues, only the Cα secondary chemical shifts are plotted. Additionally, β-strands calculated by TALOS-N and β-sheets from the cryo-EM derived atomic model are displayed [98, 108].

4.6 Long-range connectivity experiments

4.6.1 Homonuclear

Close side-chain contacts of residues located in steric zippers and on the periphery of the fibril could also be observed in a PDSD spectrum with 750 ms mixing time (fig. 4.18 & 4.19) and a PAR spectrum (fig. 4.20). These resonance peaks, which were not due to sequential contacts, were in agreement with the cryoEM structure. In detail, we could find resonances corresponding to middle and long-range contacts between: Gly33-Met35, Met35-Gly37, Ile32-Met35, Val12-His14, Gly29-Ala42, Ala2-Val36, Ile32-Val40 and Lys28-Ala42, whereas sequential and intraresidual peaks (up to 7 bonds), which have been assigned previously are marked with crosses in figures 4.18 and 4.20, respectively. In figure 4.19, correlation signals found in the aromatic- and CO-region of the 750 ms mixing time PDSD, are presented. Peaks, which have not been observed in the 200 ms PDSD (fig. 4.13), were assigned in the spectrum: Glu3-Phe4, Phe4-Arg5, Tyr10-Val12, Glu11-His13, Val12-His13, His13, Val18-Phe20, Phe19-Ala21, Lys28-Gly29, Gly29-Ile31, Gly38-Ile41 and Val40-Ile41. The correlation between Gly38-CO and Ile41-Cδ1 was most likely caused by an intermolecular polarization transfer, since this particular distance (~ 7 $\AA$) would be shorter than the intramolecular distance (~ 13 $\AA$).
Degenerated peaks were assigned with asterisks.

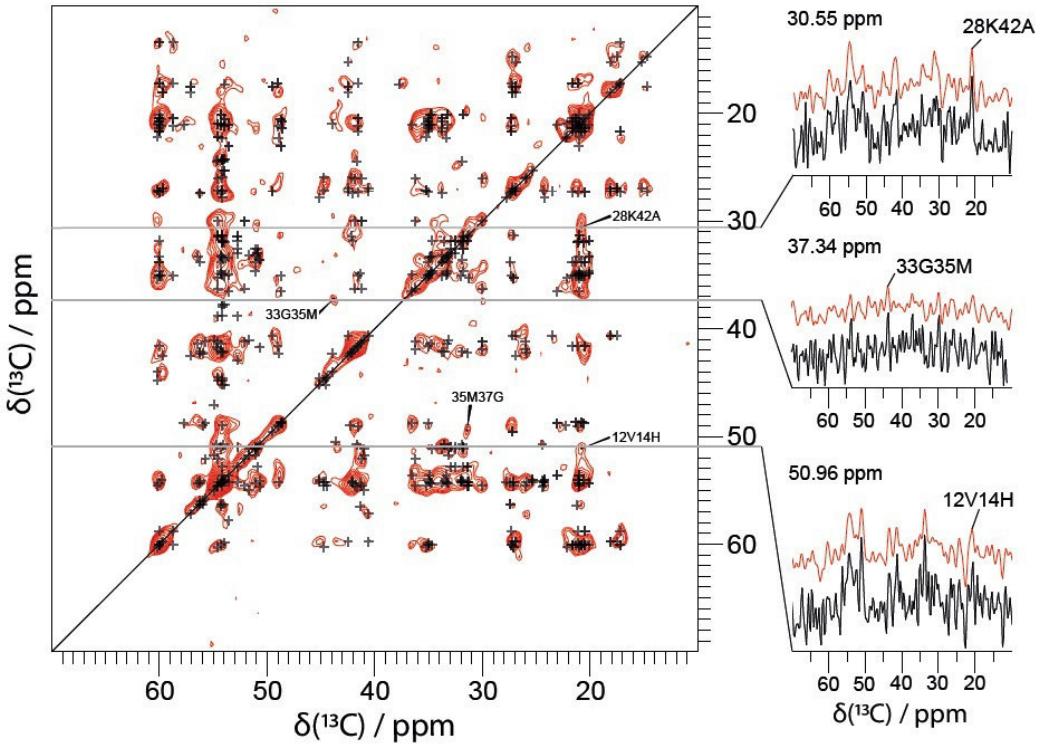

Figure 4.18: Proton-driven spin diffusion (PDSD) spectrum showing ^{13}C-^{13}C correlations of fibrillar Aβ(1-42) (CCPN). The spectrum was recorded at a magnetic field strength of 14.1 T corresponding to a Larmor frequency of 600 MHz, a sample temperature of T = 0 ± 5°C and a spinning speed of 15 kHz. For homonuclear ^{13}C-^{13}C mixing, PDSD with a mixing time of 750 ms was employed. Sequential and structural information is provided via cross-peaks of amino acids in close spatial proximity, and additional contacts not shown previously are assigned in the spectrum. Black crosses indicate intraresidual and sequential cross-peaks, predicted up to 7 bonds between neighboring amino acids (only labels for cross-peaks which can be observed in the spectrum are displayed). A squared and shifted sine bell function was used for apodization (shift of 0.40π). Contour levels increase by successive factors of 1.2. 1D slices taken from processed (red trace) and unprocessed (black trace) 2D spectra are displayed at 30.55 ppm, 37.34 ppm and 50.96 ppm, respectively.

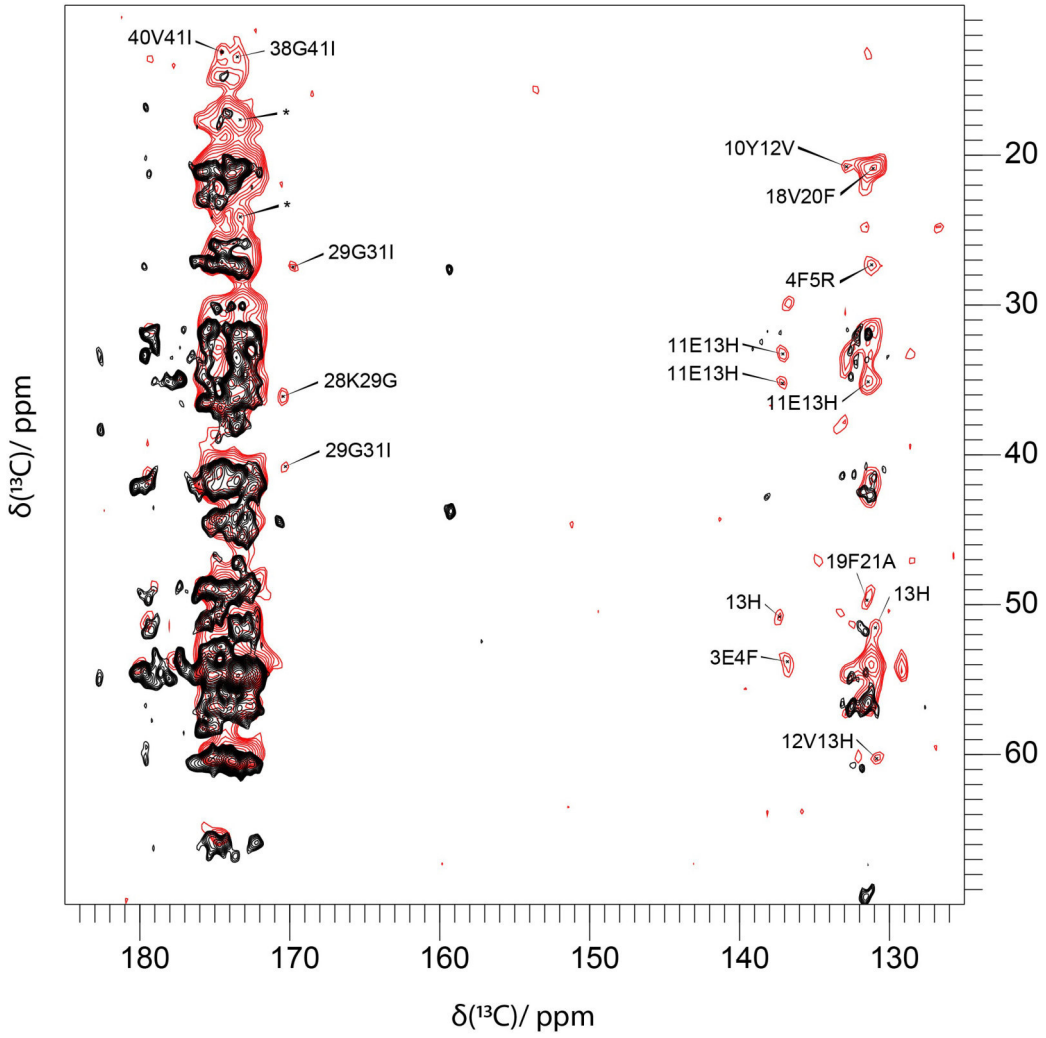

Figure 4.19: Overlay of Proton-driven spin diffusion (PDSD) spectra showing ^{13}C-^{13}C correlations of fibrillar Aβ(1-42) (CCPN). The black spectrum was recorded at a magnetic field strength of 18.8 T corresponding to a proton Larmor frequency of 800 MHz and a spinning speed of 12.5 kHz, whereas the red spectrum was recorded at a magnetic field strength of 14.1 T corresponding to a Larmor frequency of 600 MHz and a spinning speed of 15 kHz, respectively. Both spectra were recorded at a sample temperature of T = 0 ± 5°C. For homonuclear ^{13}C-^{13}C mixing, PDSD with a mixing time of 200 ms (black contours) and 750 ms (red contours) was employed. Sequential information is provided via cross-peaks of amino acids in close spatial proximity. Additional contacts not observed in the 200 ms PDSD (black) were assigned in the red 750 ms mixing time spectrum. Degenerated peaks were assigned with asterisks. A squared and shifted sine bell function was used for apodization (shift of 0.40π).

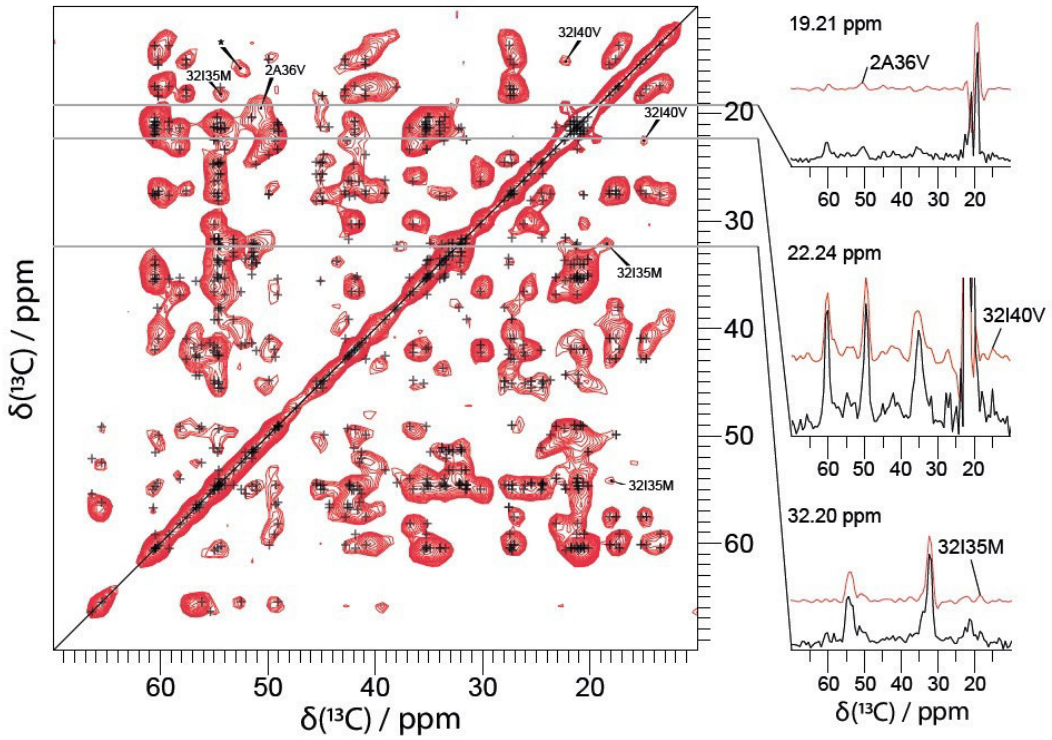

Figure 4.20: Proton-Assisted Recoupling (PAR) spectrum showing ^{13}C-^{13}C correlations of fibrillar Aβ(1-42) (CCPN). The PAR spectrum was recorded at a magnetic field strength of 14.1 T corresponding to a proton Larmor frequency of 600 MHz, a sample temperature of T = 10 ± 5°C and a spinning speed of 20 kHz. For homonuclear ^{13}C-^{13}C mixing, PAR with a mixing time of 15 ms was employed. Sequential and structural information is provided via cross-peaks of amino acids in close spatial proximity. Assignments for additional contacts not shown in figure 4.18 are indicated in the PAR spectrum. Black crosses indicate intraresidual and sequential cross-peaks, predicted up to 7 bonds between neighboring amino acids (only labels for cross-peaks which can be observed in the spectrum are displayed). A squared and shifted sine bell function was used for apodization (shift of 0.30π). Contour levels increase by successive factors of 1.2. 1D slices taken from processed (red trace) and unprocessed (black trace) 2D spectra are displayed at 19.21 ppm, 22.24 ppm and 32.30 ppm, respectively.

4.6.2 Heteronuclear

To measure long-range contacts between sidechain nitrogen atoms and sidechain carbon atoms in turn regions of the fibril, proton assisted insensitive nuclei cross polarization (PAIN CP) experiments were employed [126]. These experiments are based upon a CP step with subsequent through space mixing, exploiting a coupling to an additional third proton spin. By using a mixing time of 15 ms, contacts between nitrogen- and carbon side-chain atoms of inter-digitating residues could be examined. Here, the nitrogen irradiation points were chosen to match either the Lys28 or the Arg27 side-chain nitrogen atoms, respectively. Accordingly, the carbon irradiation points were chosen to match either the aliphatic or the carboxyl region.
Conveniently, there were much less sequential and intraresidual peaks in these spectra, compared to PAR and PDSD spectra. Furthermore, we focused on the detection of long-range correlations exclusively, which could have vanished into the noise due to dipolar truncation in the previous experiments.

Asn27-N correlation with aliphatic carbons: In fig. 4.21, the correlation peaks between Val24-Cγ1 and Asn27-Nδ2, as well as Val24-Cβ and Asn27-Nδ2 can clearly be observed. The irradiation point in the nitrogen dimension was set to 110 ppm (Asn27 sidechain nitrogen) and the irradiation point in the carbon dimension was set to 21 ppm (Val-Cγ carbons), to excite this correlation as much as possible.
Both residues, Asn27 and Val24, are closely related in space, since the sidechains are closely spaced in the turn region between residues Ala22 and Ser26. Additionally a contact between Asn27-Nδ2 and Gly25-Cα could be observed.

Lys28-N correlation with aliphatic and carboxyl carbons: Furthermore, by setting the irradiation point to the Lys28 nitrogen sidechain atom (33 ppm), the spatial proximity of the N- and C-terminal residues could be probed (fig. 4.22 and 4.23). Two spectra were acquired, using irradiation points of 42 ppm and 175 ppm in the carbon dimension, respectively. Unfortunately, due to degenerated peaks (Ala42-CO and Asp1-Cγ shared the same chemical shift value), it was unclear if the cross-peak in the CO-region was intra- or intermolecular. It was either a cross-peak between Lys28-Nζ and Asp1-Cγ, or Ala42-CO, respectively. Conversely in the aliphatic region, there was one particular intramolecular cross-peak observable, between Lys28-Nζ and Ala42-Cβ. The other non-trivial cross-peak showed the same degenerated behavior and could be caused by intraresidue lysine sidechain interaction (Lys16 or Lys28) or an inter-molecular Asp1-Cβ-Lys28-Nζ correlation, which is however less likely.

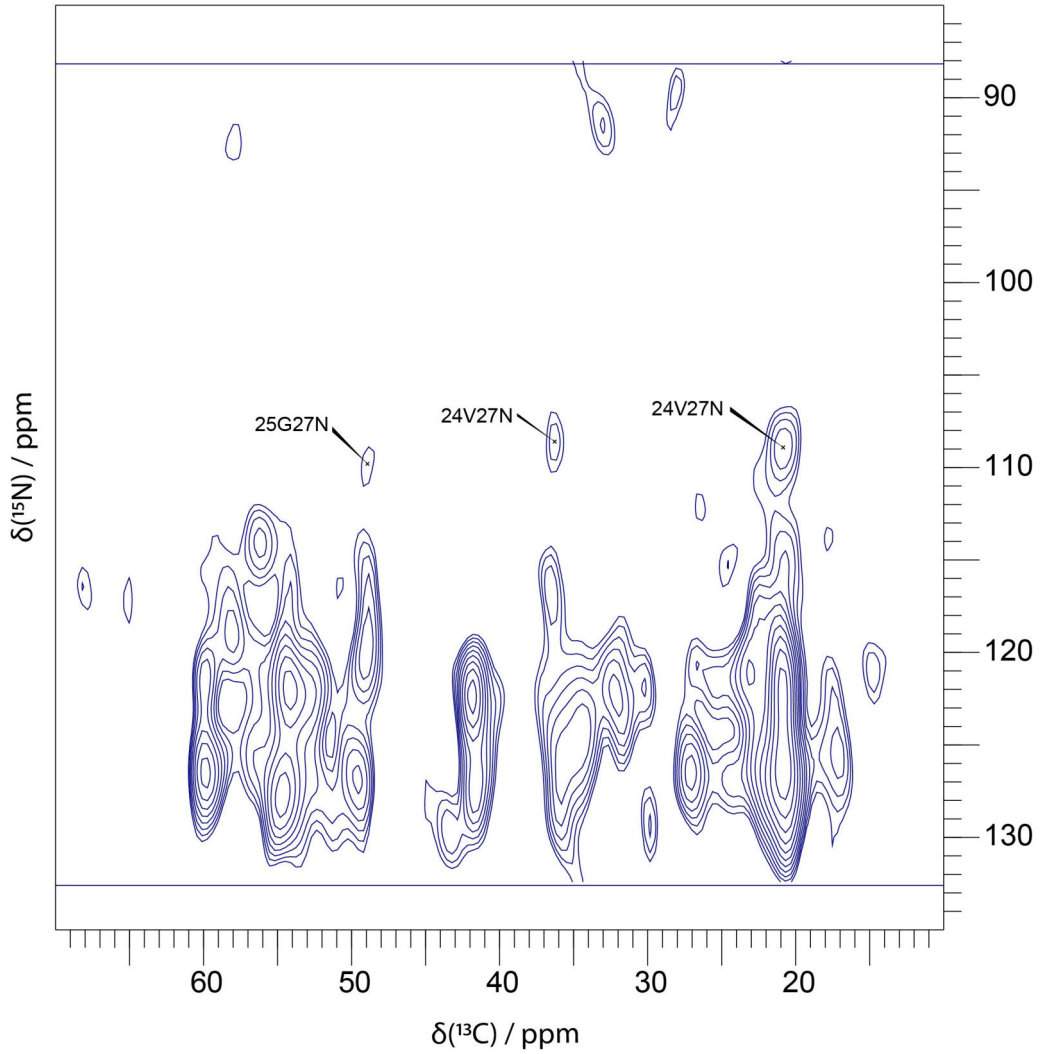

Figure 4.21: Proton-Assisted Insensitive Nuclei (PAIN) cross polarization spectrum showing ^{15}N-^{13}C correlations of fibrillar Aβ(1-42) (CCPN). The PAIN spectrum was recorded at a magnetic field strength of 14.1 T corresponding to a proton Larmor frequency of 600 MHz, a sample temperature of T = 0 ± 5°C and a spinning speed of 15 kHz. For heteronuclear ^{15}N-^{13}C mixing, PAIN CP with a mixing time of 15 ms was employed. Sequential and structural information is provided via cross-peaks of amino acids in close spatial proximity. Assigned peaks show nitrogen- to carbon inter-residual sidechain correlation within the steric zipper of the fibril, which have not been observed before. Contacts between Asn27-Nδ2 and Val24-Cβ, similar Val24-Cγ1, as well as Gly25-Nα were observable. Furthermore, correlation signals assigned in the sequential ^{15}N-^{13}C spectra can be seen (fig. 4.14). A squared and shifted sine bell function was used for apodization (shift of 0.50π).

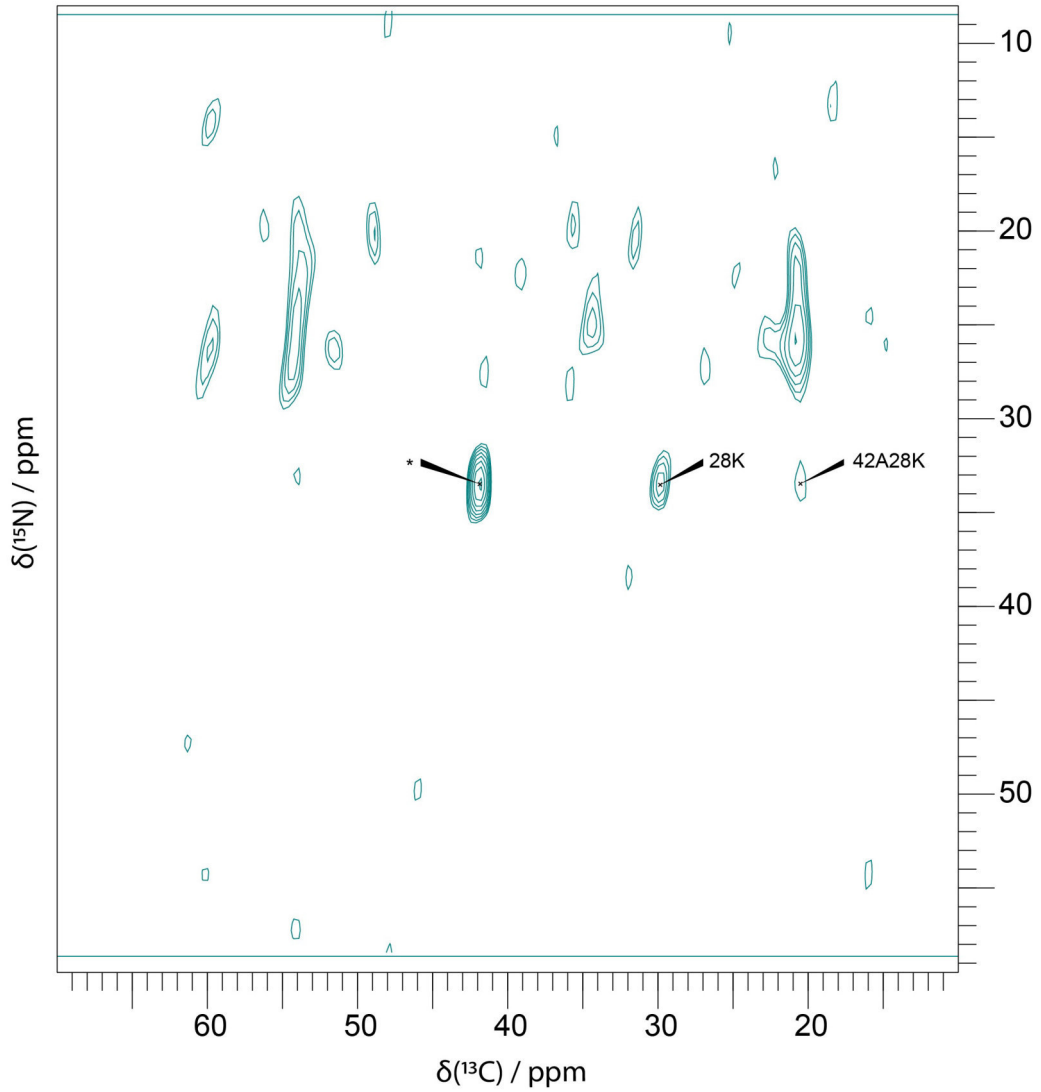

Figure 4.22: Proton-Assisted Insensitive Nuclei (PAIN) cross polarization spectrum showing ^{15}N-^{13}C correlations of fibrillar Aβ(1-42) (CCPN). The PAIN spectrum was recorded at a magnetic field strength of 14.1 T corresponding to a proton Larmor frequency of 600 MHz, a sample temperature of T = 0 ± 5°C and a spinning speed of 15 kHz. For heteronuclear ^{15}N-^{13}C mixing, PAIN CP with a mixing time of 15 ms was employed. Sequential and structural information is provided via cross-peaks of amino acids in close spatial proximity. The assigned signals showed a nitrogen- to carbon inter-residual sidechain correlation, connecting the N- and/or C-terminus with Lys28, which had not been observed before. A contact between Lys28-Nζ and Ala42-Cβ was observable. Due to degeneracies of Lys28-Nζ and Lys16-Nζ, as well as Lys28-Cϵ, Lys16-Cϵ and Asp1-Cβ, one resonance signal was assigned with an asterisk. Furthermore, sequential correlation signals were folded-in, detectable from 10 to 30 ppm in the nitrogen dimension. A squared and shifted sine bell function was used for apodization (shift of 0.30π).

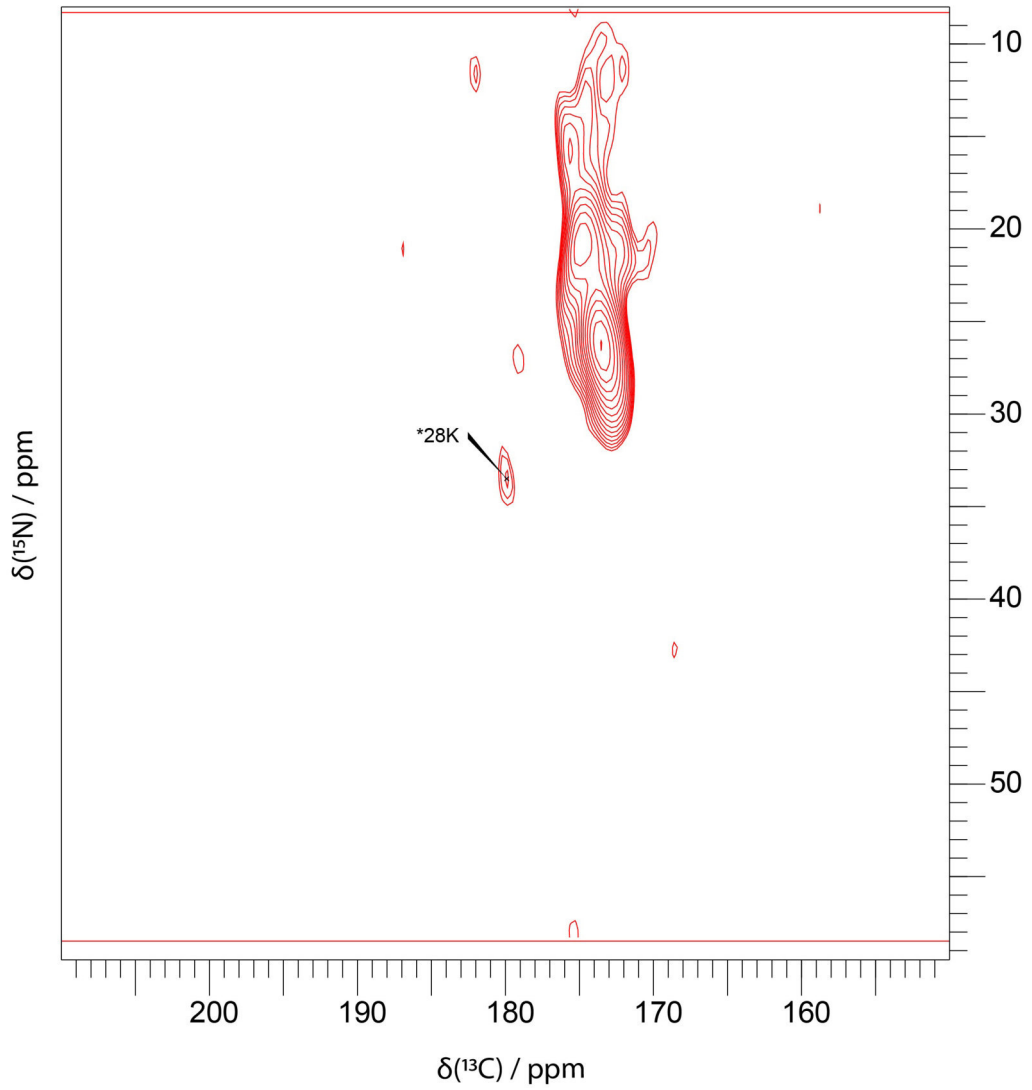

Figure 4.23: Proton-Assisted Insensitive Nuclei (PAIN) cross polarization spectrum showing ^{15}N-^{13}C correlations of fibrillar Aβ(1-42) (CCPN). The PAIN spectrum was recorded at a magnetic field strength of 14.1 T corresponding to a proton Larmor frequency of 600 MHz, a sample temperature of T = 0 ± 5°C and a spinning speed of 15 kHz. For heteronuclear ^{15}N-^{13}C mixing, PAIN CP with a mixing time of 15 ms was employed. Sequential and structural information is provided via cross-peaks of amino acids in close spatial proximity. The assigned signal showed a nitrogen- to carbon inter-residual sidechain correlation, connecting the N- and/or C-terminus with Lys28, which had not been observed before. Due to degeneracies of Ala42-CO and Asp1-Cγ, this resonance signal was assigned with an asterisk. Furthermore, sequential correlation signals were folded-in, detectable from 10 to 30 ppm in the nitrogen dimension. A squared and shifted sine bell function was used for apodization (shift of 0.35π).

4.6.3 Found interresidual contacts mapped on the structure

As observed from the PDSD, PAR and PAIN spectra, several long-range interactions could be detected. The observed contacts were mapped onto the structure for better understanding of the neighborly relations (fig. 4.24). Most contacts were found in the S-shaped hydrophobic C-terminal region of the fibril, related to the amount of interdigitating side-chains. Contacts between the N- and C-terminus, including Lys28, remained partially elusive, due to degeneracies. The interface between the two monomers, formed by a self-complimentary single steric zipper, was not unambiguously detectable, since intra- and intermolecular correlations could not be distinguished. One hint for finding an intermolecular contact would be the shorter through-space distance between Gly38 and Ile41, compared to the longer intramolecular distance.

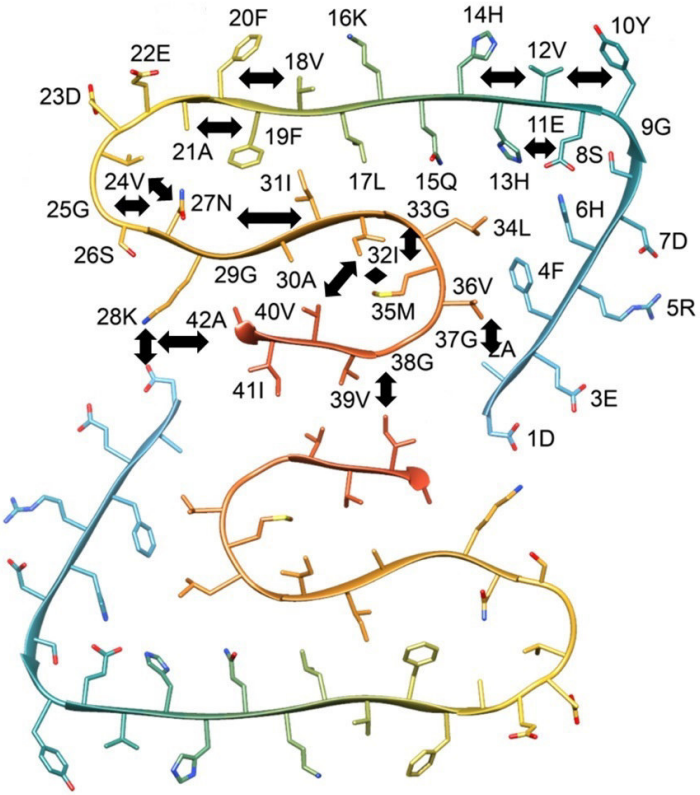

Figure 4.24: Results of 2D PDSD, PAR and PAIN spectra showed non-sequential contacts, represented by black arrows in the dimer structure. Interesidual contacts between Lys28-Ala42, Gly33-Met35 and Val12-His14 could be found in the PDSD spectrum. The PAR spectrum exhibited contacts between Ala2-Val36, Ile32-Val40, as well as Ile32-Met35. Hampered by degenerated chemical shifts, only three unambiguous contacts could be found in the PAIN spectra: Val24-Asn27, Gly25-Asn27 and Lys28-Ala42. A possible contact between Asp1 and Lys28, as well as Gly38 and Ile41 could not be assigned unambiguously.

4.7 DNP experiments

4.7.1 Sample preparation comparison

In the beginning, we compared two different sample preparation techniques, focusing on enhancement of the 600 and 800 MHz spectrometer, respectively. Here, we tried to settle the question, which sample preparation protocol is superior, under consideration of the highest enhancement. To achieve this goal, we prepared a sample similar to the common "DNP juice" (deuterated glycerol/deuterated ACN/D_2O/H_2O/TFA 40/30/20/10/0.1 % v/v/v/v/v) with an AMUPol concentration of $\sim$ 3 m$\frac{mol}{l}$. The glycerol was used as a cryoprotectant, hampering the formation of ice and forming a glassy mixture.
Since we could observe a phase separation between deuterated ACN and deuterated glycerol, there was an accumulation of the biradical AMUPol (red color) in the ACN phase. A second sample without glycerol [D_2O/deuterated ACN/H_2O/TFA (60/30/10/0.1% v/v/v/v)] and an AMUPol concentration of $\sim$ 5 m$\frac{mol}{l}$ was prepared subsequently. Both sample buffers resembled the native fibril buffer in their amount of deuterated ACN (30 %) and TFA (0.1 %). In addition, both DNP samples contained the same amount of protonated water (10 %).
In the literature there was a study published by Lopez del Amo et al., which studied the effect of different static magnetic fields on resolution of highly ordered Aβ(1-40) fibrils under low temperature conditions [127]. By employing the biradical TOTAPOL (30 m$\frac{mol}{l}$), they could obtain an enhancement factor of 20 at a 400 MHz DNP spectrometer in a 3.2 mm rotor.
First and foremost, we compared our results to the published results by Lopez del Amo et al. Here we could obtain the same enhancement factor at a 600 MHz spectrometer with a biradical concentration reduced by one order of magnitude.
In detail, we reproduced an enhancement factor of 20 at a 600 MHz spectrometer with an AMUPol concentration of 3 m$\frac{mol}{l}$ in a glycerol-containing sample. Lopez del Amo et al. measured the same enhancement factor with a TOTAPOL concentration of 30 m$\frac{mol}{l}$ at a 400 MHz spectrometer. Although the efficiency gain by using AMUPol was documented before, our sample outperformed the previously described enhancement factors [85]. Especially, by taking into account the reduced cross-effect efficiency in a higher static magnetic field. The improved efficiency of AMUPol compared to TOTAPOL could be related to a longer electron relaxation time and a stronger electron-electron dipolar coupling.
Furthermore, the enhancement factor of the glycerol-containing "DNP juice" sample was $\sim$ 4 times higher, even with reduced AMUPol concentration (fig. 4.25). Two enhanced glycerol signals could be detected in the CP spectrum of sample 1, at 65 and 75 ppm, respectively. The lower enhancement factor in the second sample could partially be attributed to the higher D_2O concentration, favoring the development of ice microcrystals, which could not be detected during the freezing

process with the naked eye. Thus, the polarization transfer facilitated by uniformly distributed biradicals around the fibrils would be hampered.
Additionally, the lower enhancement factor could be explained by the higher AMUPol concentration in the second sample favoring an increased paramagnetic relaxation enhancement [128].
To investigate, if the AMUPol concentration determined the lower enhancement factor of the glycerol-free sample, we tried to increase the AMUPol concentration of the glycerol-containing sample to 5 m$\frac{mol}{l}$. During this process the rotor had to be reopened and unfortunately an indefinite amount of sample was lost.
Thus, a reproduction of these measurements was not possible.
To study the effects of enhancement and resolution of the glycerol-free sample in a native-like buffer under DNP conditions, we continued our measurements with the second glycerol-free sample. The results of measuring 1D and 2D spectra with the same sample under the same experimental conditions in a 600 and an 800 MHz DNP spectrometer are presented in the next section.

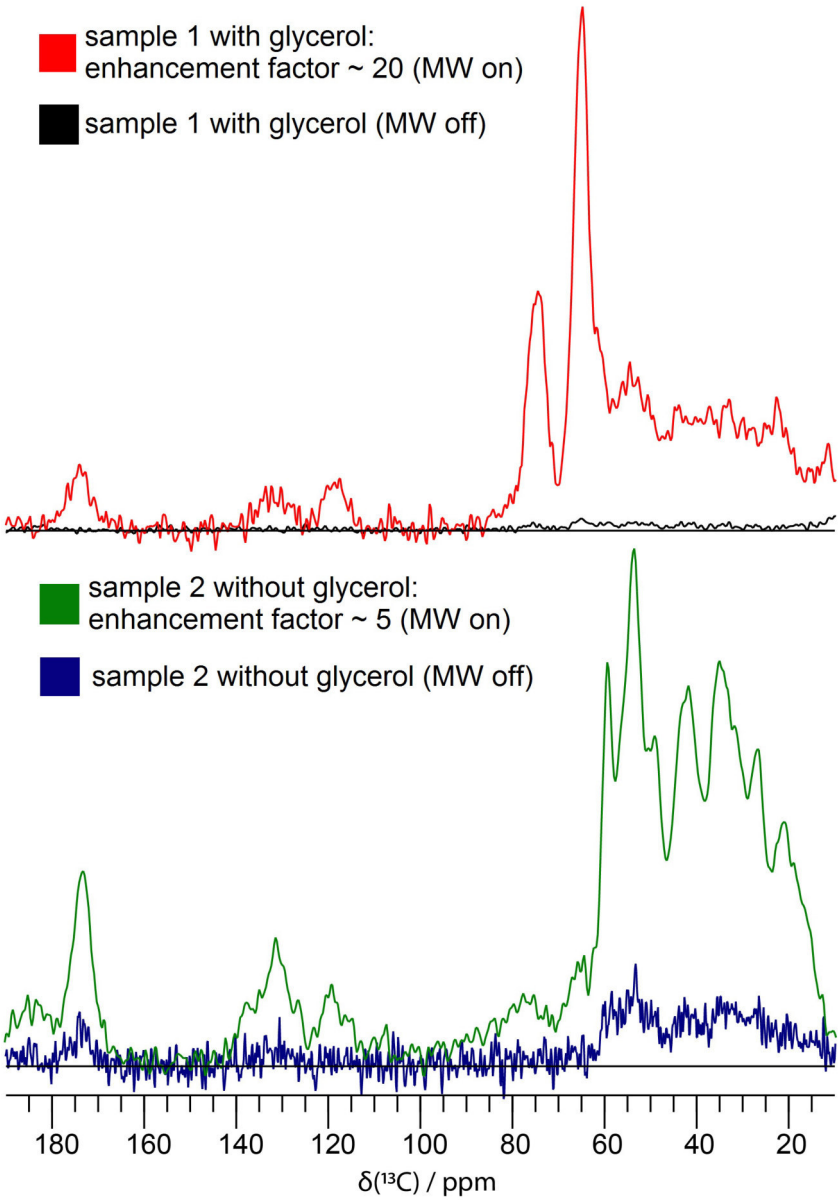

Figure 4.25: Overlay of cross polarization (CP) spectra of two DNP samples of fibrillar Aβ(1-42) (CCPN). All spectra were recorded at a magnetic field strength of 14.1 T corresponding to a proton Larmor frequency of 600 MHz, a sample temperature of T = 100 K and a spinning speed of 8 kHz. Sample 1 contained glycerol and sample 2 was glycerol free, as deducible by the glycerol peaks at 65 and 75 ppm in the red spectrum, respectively. An enhancement factor of 20, for a sample containing 3 m$\frac{mol}{l}$ AMUPol and 40 % glycerol, could be obtained, upon switching on the microwave (MW) irradiation. The enhancement factor of the glycerol-free sample was 5. Due to differing numbers of scans in the red and the black spectrum (32 and 512 respectively), the red spectrum was rescaled. In the green and the blue spectrum, the same number of scans was aquired (128). A squared and shifted sine bell function was used for apodization (shift of 0.40π for all spectra).

4.7.2 600 and 800 MHz DNP comparison

After comparing two different sample preparation techniques, we started to investigate the magnetic field dependence of the enhancement factor and the resolution of the glycerol-free DNP sample. In the previously cited study by Lopez del Amo et al., it was shown that a higher static magnetic field improved the resolution, despite measuring at low temperatures. In theory, sample heterogeneity like the presence of several different molecular orientations and conformations contributed to inhomogeneous line-broadening, compromising the resolution at low temperatures. However, by increasing the static magnetic field, homonuclear contributions are scaled down.
Our intention was to check, if previously published results could be transferred to our glycerol-free Aβ(1-42) fibrils DNP sample. We employed 1D CP measurements and 2D PDSD measurements to compare enhancement factors and resolution at magnetic fields of 14.1 (600 MHz) and 18.8 T (800 MHz), respectively.
Conclusively, we could detect a slight decrease in enhancement with increased static magnetic field, like expected for cross-effect DNP. Furthermore, losses in resolution could be partially restored by measuring at a higher static magnetic field.

Enhancement factors of 600 and 800 MHz

We tested the enhancement factors in a 600 and 800 MHz static magnetic field. The literature reported decreasing enhancement factors with increasing static magnetic fields for cross-effect DNP [85–87]. This could be confirmed (fig. 4.26). In fact, the enhancement is diminished from a factor of 5.4 to 4 for a glycerol-free sample.
For the CP spectra, the acquisition parameters were quite similar and the number of scans was the same. Comparing both identically processed spectra with active microwave irradiation already showed an improved resolution in the 800 MHz DNP spectrum, which was afterwards investigated in 2D PDSD spectra.

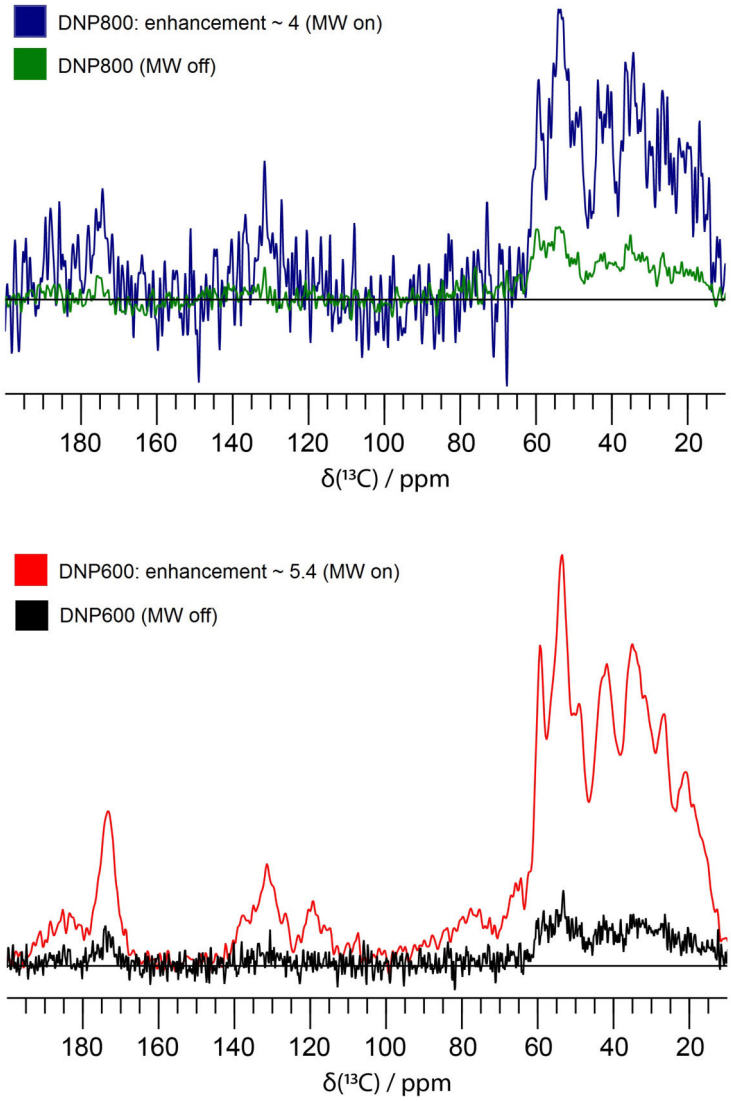

Figure 4.26: Overlay of cross polarization (CP) spectra of one DNP sample of fibrillar Aβ(1-42) in two different static magnetic fields (CCPN). The red and black spectra, shown at the bottom, were recorded at a magnetic field strength of 14.1 T corresponding to a proton Larmor frequency of 600 MHz, a sample temperature of T = 100 K, a spinning speed of 8 kHz and an equal number of scans (128). The green and blue spectra, shown at the top, were recorded at a magnetic field strength of 18.8 T corresponding to a proton Larmor frequency of 800 MHz, a sample temperature of T = 100 K and a spinning speed of 11 kHz. The blue spectrum was recorded with eight scans and the green one with 128 scans, respectively. Enhancement factors of 5.4 at 600 MHz and 4 at 800 MHz for a glycerol-free sample containing 5 m$\frac{mol}{l}$ AMUPol could be reached, upon switching on the microwave (MW) irradiation. Due to similar acquisition parameters and the same amount of scans, an enhanced resolution could be observed in the 800 MHz DNP spectrum. A squared and shifted sine bell function was used for apodization (shift of 0.40π for all spectra).

Resolution

To compare the effect on spectral resolution in two different static magnetic fields, we acquired PDSD spectra with 20 ms mixing time, the same amount of scans and the same processing parameters at the 600 and 800 MHz DNP spectrometer, respectively. Obviously, as shown in figure 4.27, the resolution improved significantly, as previously suggested by Lopez del Amo et al. [127]. Here, we could obtain a partial restoration of resolution. We could show the narrowing of the diagonal, as well as line-narrowing of Val-Cα-Cβ (4.5 to 3 ppm), Val-Cα-Cγ (4 to 2.7 ppm) and Val-Cβ-Cγ correlations (4.9 to 3.2 ppm), marked with boxes in figure 4.27 and shown in 1D slices. Moreover, peak splittings were resolved.
Here, we could again observe the vanishing of the alanine peaks in the spectrum of the 800 MHz spectrometer. This seemed to be related to the field strength and experimental conditions, matching a rotational resonance condition, as this feature has been observed in the room temperature spectra, too.
In fact, rotational resonance in the 600 MHz spectrum equals to 53.3 ppm ($8000Hz/\frac{150Hz}{ppm}$), whereas it reached 60 ppm in the 800 MHz spectrum ($12000Hz/\frac{200Hz}{ppm}$). A multiple of the 800 MHz rotational resonance (120 ppm) nearly recoupled the Ala-Cα ($\sim$ 50 ppm) and Ala-CO ($\sim$ 175 ppm) resonances.
Despite the higher resolution, the enhancement factor for the cross effect was diminished, manifested in the higher noise level in the 800 MHz DNP spectrum.

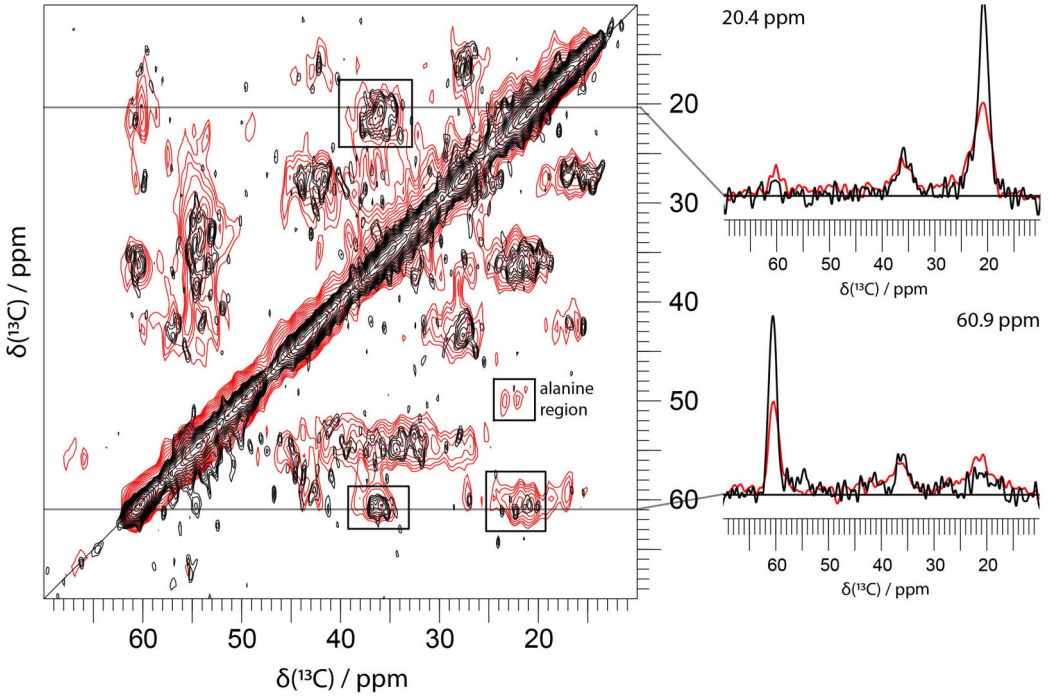

Figure 4.27: Overlay of Proton-Driven Spin Diffusion (PDSD) spectra of fibrillar Aβ(1-42) under DNP conditions at different field strengths (600 MHz, red) and (800 MHz, black) (CCPN). The black spectrum was recorded at a magnetic field strength of 18.8 T corresponding to a proton Larmor frequency of 800 MHz, a sample temperature of T = 100 K and a spinning speed of 12 kHz. The red spectrum was recorded at a magnetic field strength of 14.1 T corresponding to a proton Larmor frequency of 600 MHz, a sample temperature of T = 100 K and a spinning speed of 8 kHz. For homonuclear ^{13}C-^{13}C mixing, PDSD with a mixing time of 20 ms was employed. Both spectra were acquired with the same amount of scans and processed with the same parameters (shift of 0.30π). Conclusively, we could observe a narrowing of the diagonal, as well as line-narrowing of Val-Cα-Cβ (4.5 to 3 ppm), Val-Cα-Cγ (4 to 2.7 ppm) and Val-Cβ-Cγ correlations (4.9 to 3.2 ppm), marked with boxes and shown in 1D slices. Moreover, peak splittings were resolved. Alanine peaks seemed to vanish, which is a reproducible feature at 800 MHz spectrometers and caused by a rotational resonance effect.

4.7.3 Correlation of resolution and temperature

Lopez del Amo et al. hypothesized that the resolution of highly-ordered amyloidogenic proteins and peptides would not be compromised at low temperatures, since the structural heterogeneity would not dominate the achievable resolution [127].
On the other hand, two other studies from different work groups showed a loss of resolution of a protonated protein or a protonated fibril with decreasing temperatures, respectively [129, 130]. Interestingly, the more recently published study could detect a site-specific line-broadening in the fibril sample, determined by the position of the residue. Apparently, solvent-exposed residues were broadened, whereas the hydrophobic fibril core residues were still detectable and suffered from less line-broadening. Remarkably, the sample did not contain any cryo-protectant nor any radical, it was just measured in a cryo probe.
Our sample consisted of $\sim$ 40 μl sample pellet of Aβ(1-42) fibrils, suspended in D_2O/ACN/H_2O/TFA (60/30/10/0.1% v/v/v/v) with a biradical concentration of $\sim$ 5 m$\frac{mol}{l}$ (AMUPol). DNP measurements were carried out at a temperature of 100K. During the freezing process, sidechain orientations could freeze out in an ensemble of different conformations, maintaining only rigid regions above the noise threshold in the spectra. This effect led to inhomogeneous line-broadening, because each conformation preserved its very own resonance freuquency after the freezing process.
As expected, residues with long side-chains, like Asp, Glu, Lys and Ile, showed significant intensity losses and line-broadening (fig. 4.28). Obviously, auto-correlation signals (diagonal) and the carboxyl region of the spectrum were broader indicating a lower resolution in the DNP spectrum. Similarly, Val-Cβ-Cγ resonances were broadened from 2.9 ppm in the room temperature spectrum to 3.7 ppm in the DNP spectrum, measured in the direct dimensions of both spectra. Line-broadening in regions characteristic for Ile signals, could also be attributed to a variety of possible rotameric states [131].
Vanishing signals of side-chains of acidic amino acids were observable in the CO region of the spectrum, in particular Glu22-Cγ-Cδ and Asp-Cβ-Cγ. Additionally, the resonance signal of the C-terminus of Ala42 became undetectable, too. Interestingly, the well defined resonance signals of Val24 also vanished, indicating that these resonances do not represent one predominant rigid side-chain orientation at room temperature. However, one has to keep in mind that methyl resonances are typically weak at 100 K [132].
In brief, we could definitely observe a compromised resolution at 100K. Lopez del Amo et al. reported line-widths below 1 ppm at room temperature, as well as at 100 K, with only a slight resolution loss (130 to 160 Hz). This result could not be reproduced with our sample. However, the loss in intensity of residues with long side-chains, like Ile, Leu and Lys, could be reproduced. Observing the same

line-widths at room temperature and 100 K seemed to be hampered by inhomogeneous line-broadening, which could possibly be circumvented by addition of a cryo-protectant. The cryo-protectant would have assured that solvent-exposed areas of high mobility do not get freeze trapped during the cooling process. These results most likely verified our hypothesis that ice microcrystals developed in the glycerol-free sample, as the lower enhancement factor, compared to a glycerol containing sample, supported this result. In the future, these experiments should be reproduced with a glycerol-containing sample to prove, if a better resolution and a higher enhancement could be achieved.
Since Bauer et al. found weak temperature-dependent decays for core-residues, we tried to confirm these results [130]. Interestingly, our results indeed showed line-broadening of solvent-exposed (Asp1, Asp7, His14, Glu22, Ser26, Lys28), but moreover decays of core residues (His13, Leu17, Val24, Ile31, Leu34, Ala42), too.
Bauer et al. hypothesized the intensity loss of solvent-exposed residues would be highly influenced by the diminished mobile water layer upon freezing, however we observed line-broadening of residues located in steric zippers of the fibril core, too.

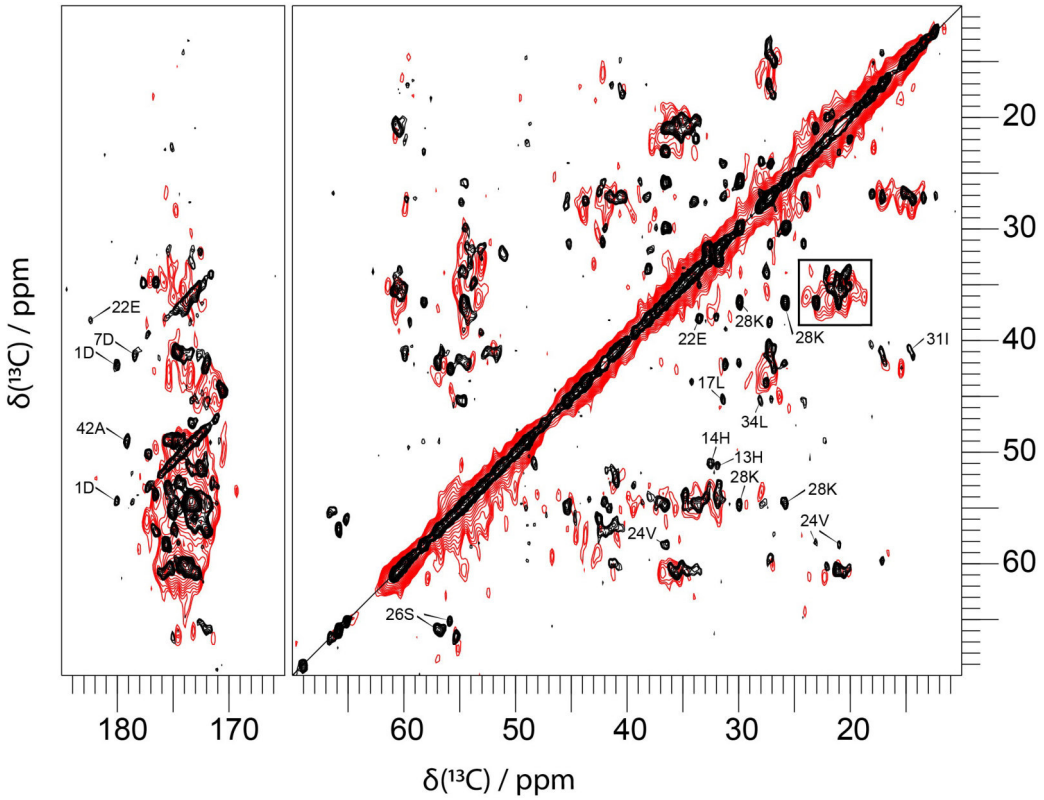

Figure 4.28: Overlay of Proton-Driven Spin Diffusion (PDSD) spectra of fibrillar Aβ(1-42) under DNP conditions (100 K, red) and at 263 K (black) (CCPN). Both spectra were recorded at a magnetic field strength of 18.8 T corresponding to a proton Larmor frequency of 800 MHz with a spinning speed of 12 kHz and 144 scans (red spectrum) or 12.5 kHz and 80 scans (black spectrum), respectively. For homonuclear ^{13}C-^{13}C mixing, PDSD with a mixing time of 20 ms was employed. In the aliphatic region, slight chemical shift deviations in the Ile region became obvious. Even more evident were the missing 24Val-Cβ-Cγ signals. Likewise, Val-Cβ-Cγ resonances were broadened from 2.9 ppm in the room temperature spectrum to 3.7 ppm in the DNP spectrum (black rectangle). In the aliphatic and the carboxyl region of the spectrum, sidechain signals of residues with long side-chains dropped below the noise threshold (Ile, Asp, Glu, Lys). Disappearing correlations were assigned. Most obvious observations for a degraded resolution were the broadening of the diagonal and the carboxyl region of the spectrum. A squared and shifted sine bell function was used for apodization (shift of 0.30π for both spectra).

4.8 ^{13}C-T_ρ^1 experiments

Studying molecular motion of proteins can be facilitated by ssNMR, opening a detection range of motions covering several timescales [133]. In particular, measurements of the spin-lattice relaxation time in the rotating frame (T_ρ^1) of ^{15}N nuclei allow for the detection of motions with correlation times spanning a ns to ms range [134, 135]. Probing this structural flexibility can be carried out by using an incremented spin-lock pulse incorporated in standard 2D experiments [136, 137]. In this time regime, the modulation of ^{1}H-^{15}N couplings by molecular motions and/ or the CSA of ^{15}N affect the ^{15}N-T_ρ^1 relaxation, causing differences in the detected intensities.

At this point, two different processes have to be accounted for: incoherent processes, caused by stochastic modulations of local fields by molecular motions, our observable, and coherent processes, like dipolar dephasing, which have to be suppressed [138]. To avoid the presence of coherent contributions during the T_ρ^1 measurement, rotary resonance and the HORROR condition should be avoided [139–141]. Besides, an elimination of coherent effects could be shown for ^{15}N-T_ρ^1 measurements, without proton decoupling during the spin-lock pulse, under complying to defined experimental conditions (spinning speed above 45 kHz and spin-lock field above 10 kHz for the fully protonated protein GB1) [138].

While ^{15}N-T_ρ^1 experiments are useful for the detection of backbone motions, ^{13}C-T_ρ^1 experiments provide sensitivity towards backbone, as well as side-chain motions, due to the higher abundance of ^{13}C nuclei. We used spin-lock edited ^{13}C-PDSD and ^{13}C-SPC5 spectra to investigate side-chain flexibility in relation to the according position in the fibril. Obviously, these homonuclear transfer mechanisms do not work properly at spinning speeds exceeding 45 kHz, due to stronger averaged proton couplings in the PDSD- and hardware limitations in the SPC5 case. Moreover, there was no probe available, which would have allowed for such high spinning speeds.

To minimize coherent effects caused by dipolar couplings to protons, due to the slower spinning speed, full power proton decoupling was applied during the incremented T_ρ^1-spin lock pulse.

Our main goal was to support our previous finding of a slightly less rigid N-terminus, compared to the middle domain and C-terminus of the fibril. Since the efficiency of the spin lock pulse is hampered by molecular motions, we expected to find a decreased relaxation time in the rotating frame (T_ρ^1) for these flexible residues. Consequently, we measured the decay of isolated unambiguously assigned resonances, located in several domains of the protein. To evaluate the spectra quantitatively, we integrated the resonance peaks in the software Sparky [101]. Afterwards, normalized integrated peak intensities were exported to Origin and plotted against the applied spin lock times. Subsequently, the data points were

fitted with a monoexponential decay function ("ExpDec1"). Because we could not follow the full magnetization decay, for several signals a significant amount of magnetization was still left. The complete data acquisition and analysis is explained in the two following subsections. All fit parameters, including the constants $I(\infty)$ and A, were listed in supplement table 4.3 and 4.4 in the appendix.

4.8.1 PDSD-^{13}C-T_ρ^1-experiment

PDSD-T_ρ^1 spectra were aquired as time series with increasing spin lock times. The reference spectrum was a PDSD experiment with a spin lock time of 0 ms. During the incrementation of the spin lock time, the resonance signals of mobile parts of the fibril lost intensity in the spectrum. In figure 4.29, a reference spectrum is shown. For a better understanding of the procedure, representative 1D slices, showing the intensity decay of Ala42-Cα- and Cβ correlations for different spin lock times, is shown in figure 4.30. In this figure, the reference spectrum is shown in light-grey, representing the maximum intensity, whereas the darker the 1D spectrum got, the more advanced was the spin lock time. All assigned peaks were integrated in each spectrum of the time series and afterwards normalized with the maximum integral value. Finally, the normalized integrated peak intensities were plotted against the spin lock time and fitted with a mono-exponential decay function (fig. 4.31-4.36).
Due to the instrinsic limitations of the experiment, being influenced by possible spin diffusion during the spin lock, a relatively low SNR and residual magnetization, the presented results are only discussed qualitatively.
Alanine residues, except 42-Cα-Cβ, displayed similar decay times around 10 ms with good fit quality (fig. 4.31). The Ala42 sidechain resonance seemed to decay slower, since the level of magnetization did not decay significantly between 2.5 and 5 ms, which could be attributed to residual magnetization and/or spin diffusion.
Val24 resonances showed similar decay times, whereas solvent-exposed carboxyl groups of Glu22 and Asp23 decayed rather fast (fig. 4.32).
Likewise, the N-terminal residue Ser8-Cα-Cβ displayed a relatively fast decay, which clearly differed from the decay times of Ser26-Cα-Cβ and Ser26-Cβ-CO (fig. 4.33).
^{13}C-T_ρ^1 times of Lys28 and Gly29 resonances demonstrated the expected mono-exponential decay without a detection of outliers or a strong influence of residual magnetization (fig. 4.34).
In contrast, for isoleucine resonances, which are located in the S-shaped core of the fibril, outliers not lying on the fit curve prevented the fitting of measurement points with the fitting function. Nonetheless, two Ile31 and one Ile32 side-chain resonances could be fitted with relatively long decay times (fig. 4.35).
On the other hand, N-terminal Arg5 resonances displayed rather fast decay times (fig. 4.36).

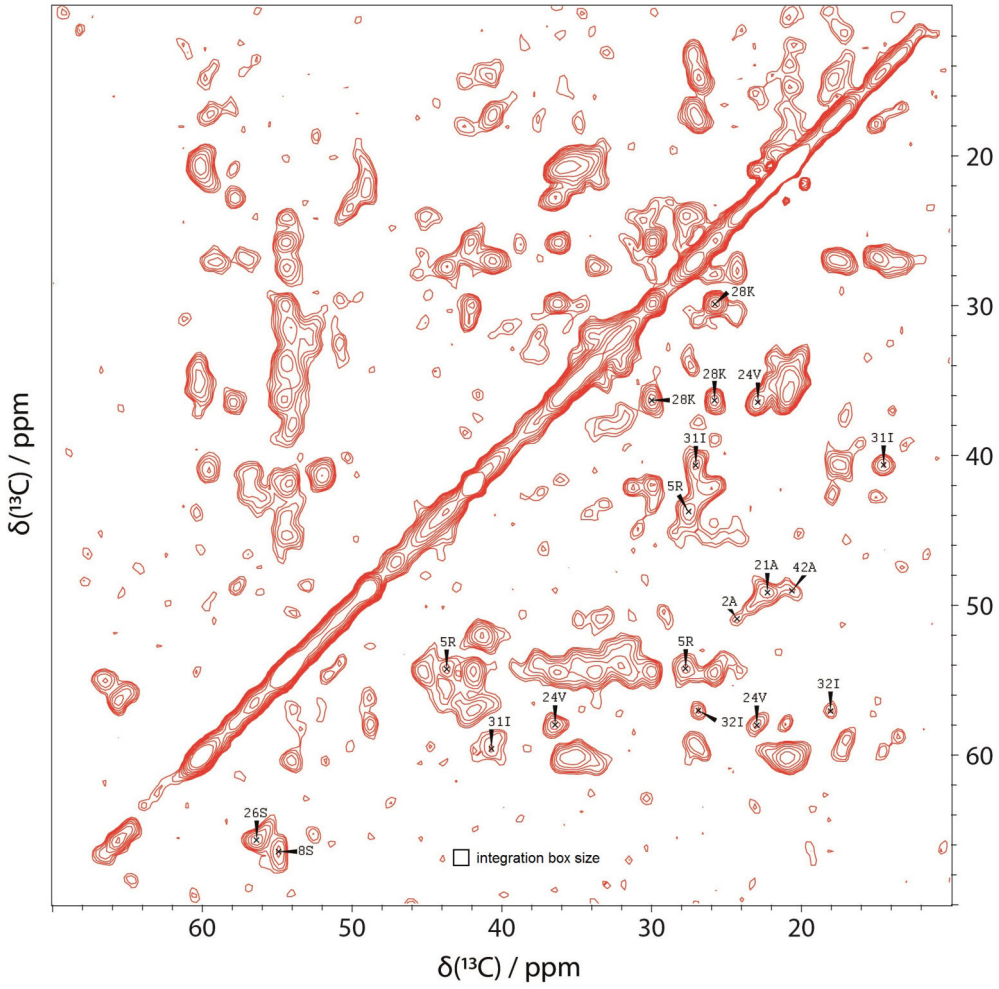

Figure 4.29: 2D Proton-Driven Spin Diffusion (PDSD)-T_ρ^1 reference spectrum of fibrillar Aβ(1-42) (spin lock time = 0 ms) (SPARKY). The spectrum was recorded at a magnetic field strength of 14.1 T corresponding to a proton Larmor frequency of 600 MHz, a sample temperature of T = 0 ± 5°C and a spinning speed of 15 kHz. For homonuclear ^{13}C-^{13}C mixing, PDSD with a mixing time of 50 ms was employed. A squared and shifted sine bell function was used for apodization (shift of 0.35π). Assigned resonance peaks were integrated in each spectrum of the spin lock time series. An integration box is displayed in the bottom of the spectrum, covering an area of 1ppm · 1ppm.

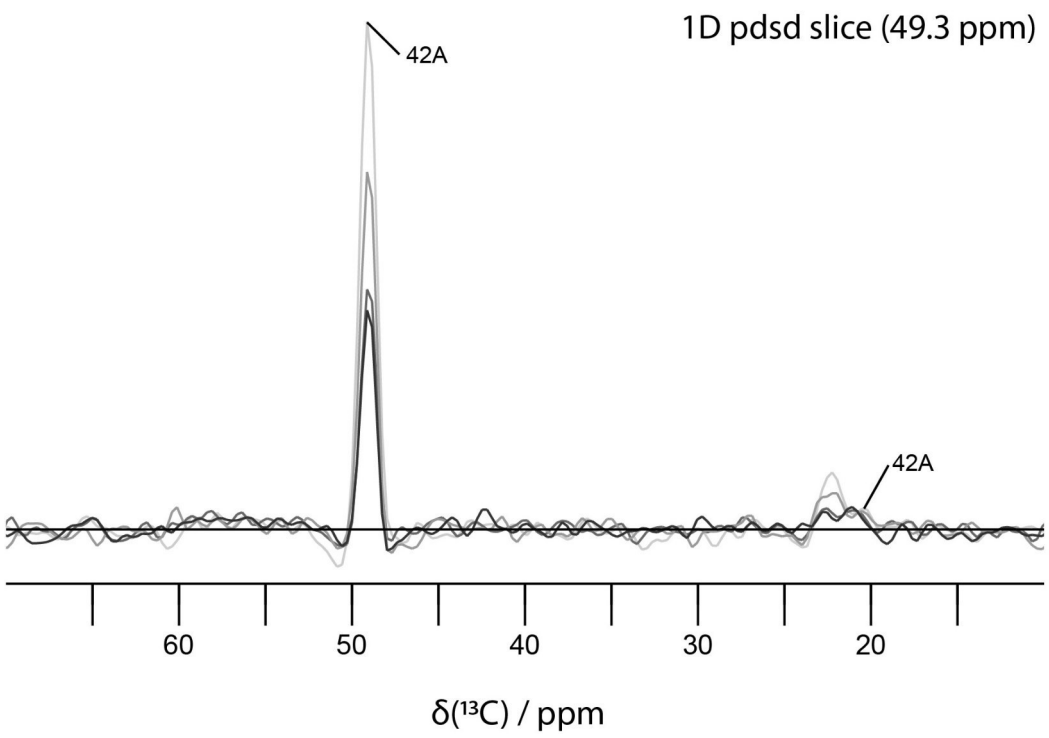

Figure 4.30: Representative 1D overlay plot of Proton-Driven Spin Diffusion (PDSD)-T_ρ^1 spectra of fibrillar Aβ(1-42) (CCPN). The spectra were recorded at a magnetic field strength of 14.1 T corresponding to a proton Larmor frequency of 600 MHz, a sample temperature of T = 0 ± 5°C, a spin lock field of 37.5 kHz and a spinning speed of 15 kHz. For homonuclear ^{13}C-^{13}C mixing, PDSD with a mixing time of 50 ms was employed. A squared and shifted sine bell function was used for apodization (shift of 0.35π). In the reference 1D slice (light-grey) (spin lock time = 0 ms) taken out of a plane of the original 2D spectrum at 49.3 ppm, Ala42-Cα (49 ppm) and Ala42-Cβ (21 ppm) resonance peaks are assigned. Darker 1D slice colors indicate longer spin lock times (0, 2.5, 5 and 10 ms (black), respectively). From the overlayed 1D slices one can clearly observe the intensity loss of Ala42-Cα. For the final data analysis, resonance signals in 2D spectra were integrated.

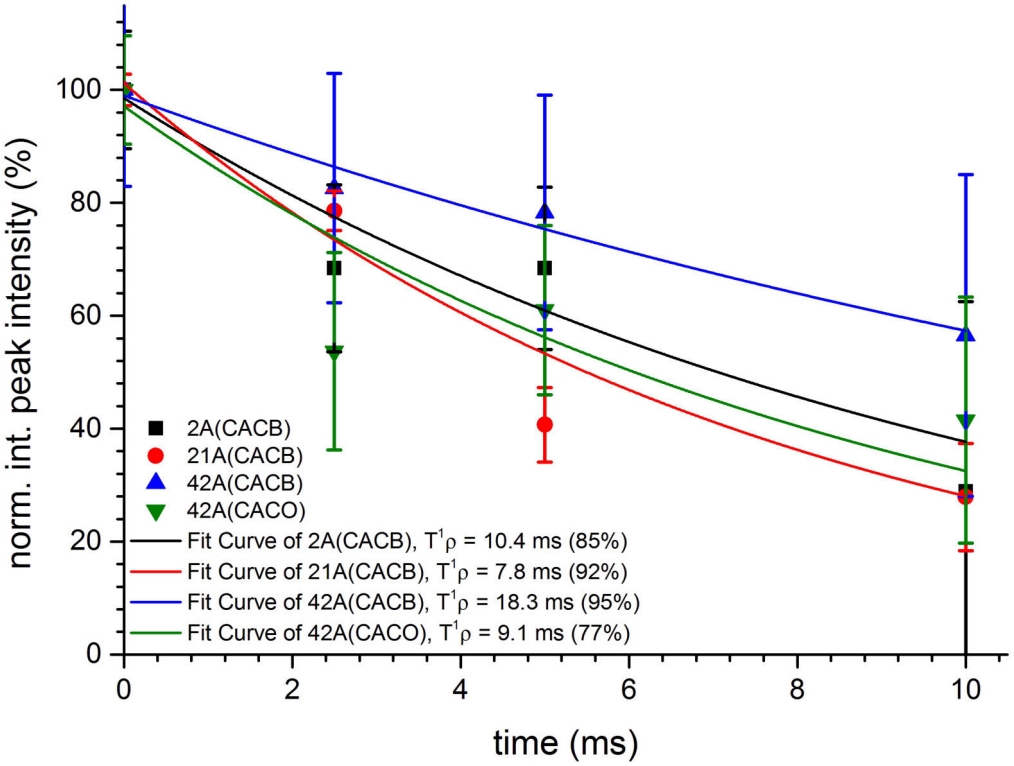

Figure 4.31: Results from PDSD-T_ρ^1-experiments plotted as normalized peak integral of the observed alanine resonances versus the spin lock time (ORIGIN). ^{13}C-T_ρ^1 represents the decay time of each residue during the spin lock. Alanine resonances exhibited similar decay times, whereas Ala42-Cα-Cβ exposed a constant level of magnetization in between 2.5 and 5 ms spin lock time. R^2_{adj}-values (adjusted coefficient of determination) are given in parenthesis and indicate the quality of the fit.

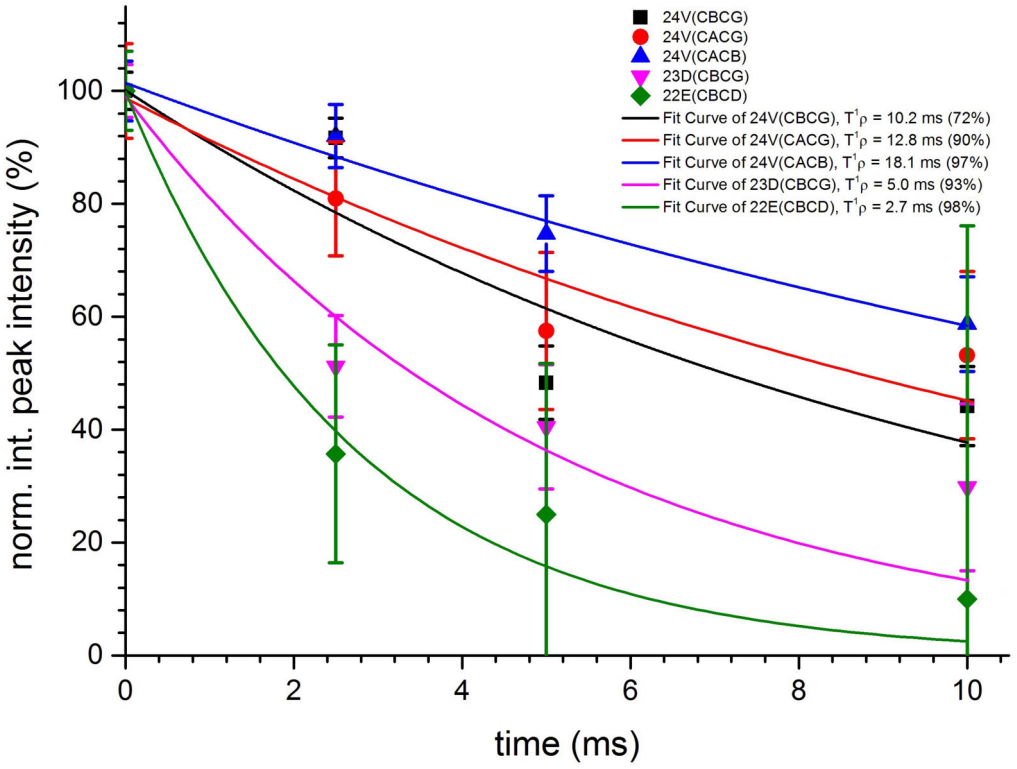

Figure 4.32: Results from PDSD-T_ρ^1-experiments plotted as normalized peak integral of decaying neighboring residues located in a turn region of the middle domain versus the spin lock time (ORIGIN). ^{13}C-T_ρ^1 represents the decay time of each residue during the spin lock. Val24 resonances exhibited similar decay times, clearly exceeding the decay times of the solvent prone terminal resonances of Glu22 and Asp23, respectively. R^2_{adj}-values (adjusted coefficient of determination) are given in parenthesis and indicate the quality of the fit.

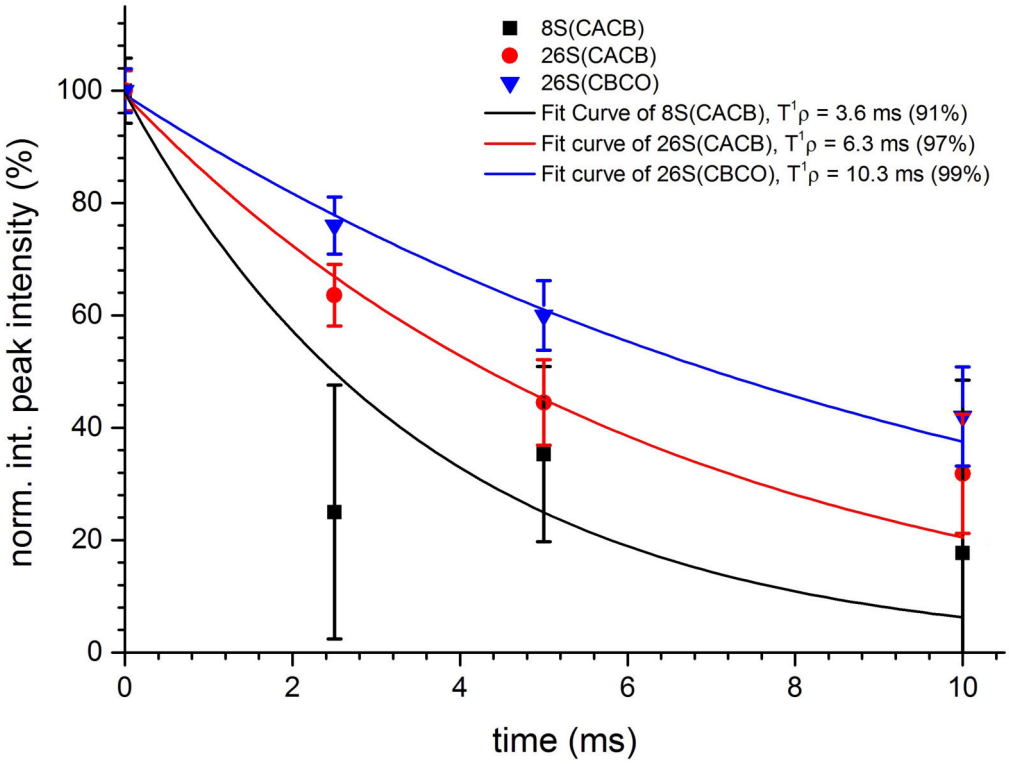

Figure 4.33: Results from PDSD-T_ρ^1-experiments plotted as normalized peak integral of the decaying serine resonances versus the spin lock time (ORIGIN). ^{13}C-T_ρ^1 represents the decay time of each residue during the spin lock. The N-terminal Ser8-Cα-Cβ resonance decayed relatively fast, due to the data point at 2.5 ms. The solvent-exposed Ser26 resonances, near the Lys28-Asp1-Ala42 salt bridge decayed slower. R^2_{adj}-values (adjusted coefficient of determination) are given in parenthesis and indicate the quality of the fit.

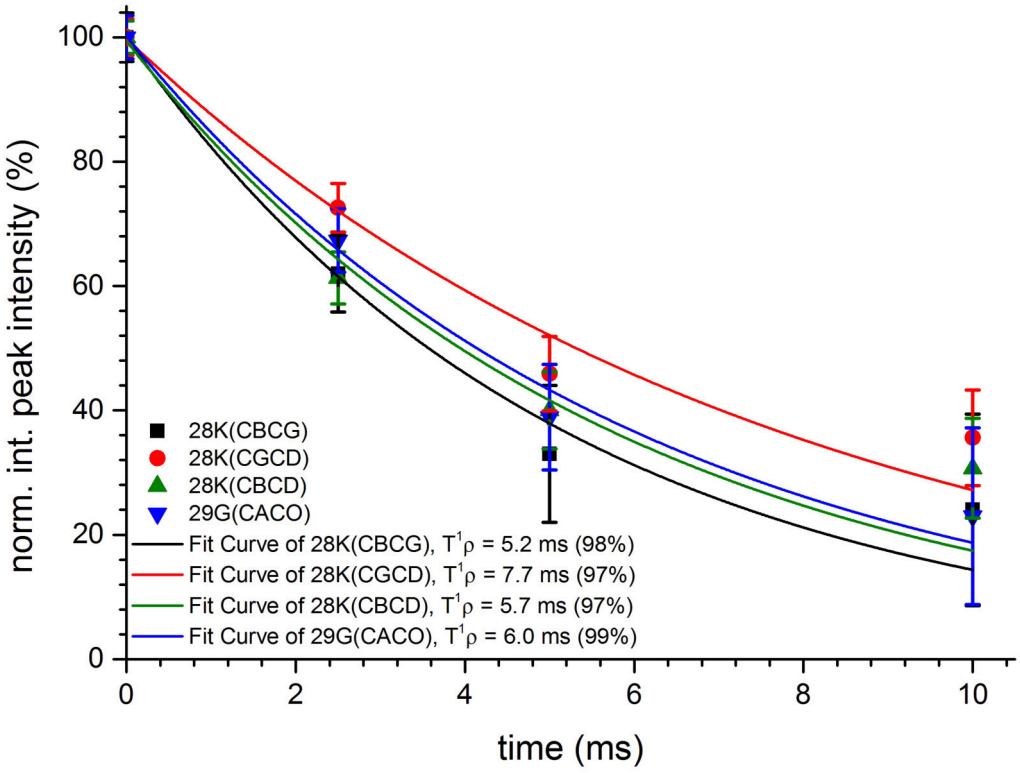

Figure 4.34: Results from PDSD-T_ρ^1-experiments plotted as normalized peak integral of the decaying neighboring residues Lys28 and Gly29 versus the spin lock time (ORIGIN). ^{13}C-T_ρ^1 represents the decay time of each residue during the spin lock. Lys28 and Gly29 displayed similar decay times. R^2_{adj}-values (adjusted coefficient of determination) are given in parenthesis and indicate the quality of the fit.

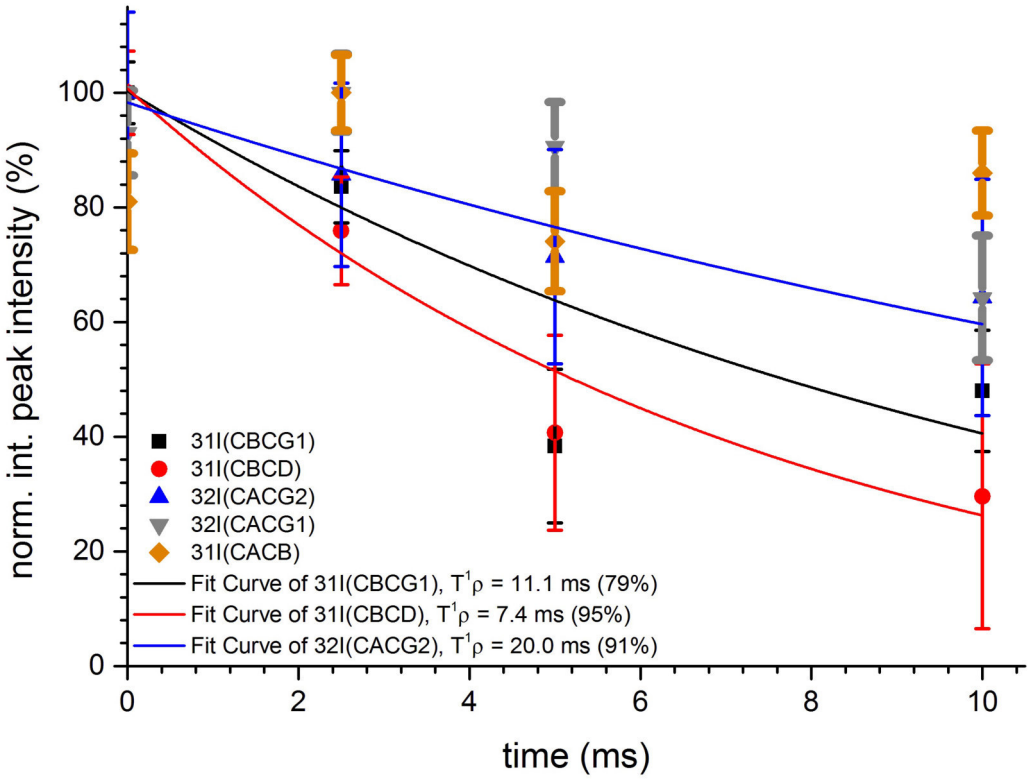

Figure 4.35: Results from PDSD-T_ρ^1-experiments plotted as normalized peak integral of the observed decaying isoleucine resonances versus the spin lock time (ORIGIN). ^{13}C-T_ρ^1 represents the decay time of each residue during the spin lock. Remarkably, due to outliers, not all buried isoleucine resonances could be fit with a mono-exponential decay. Nonetheless, the fits of Ile31- and Ile32-sidechain resonances displayed rather long decay times. R^2_{adj}-values (adjusted coefficient of determination) are given in parenthesis and indicate the quality of the fit.

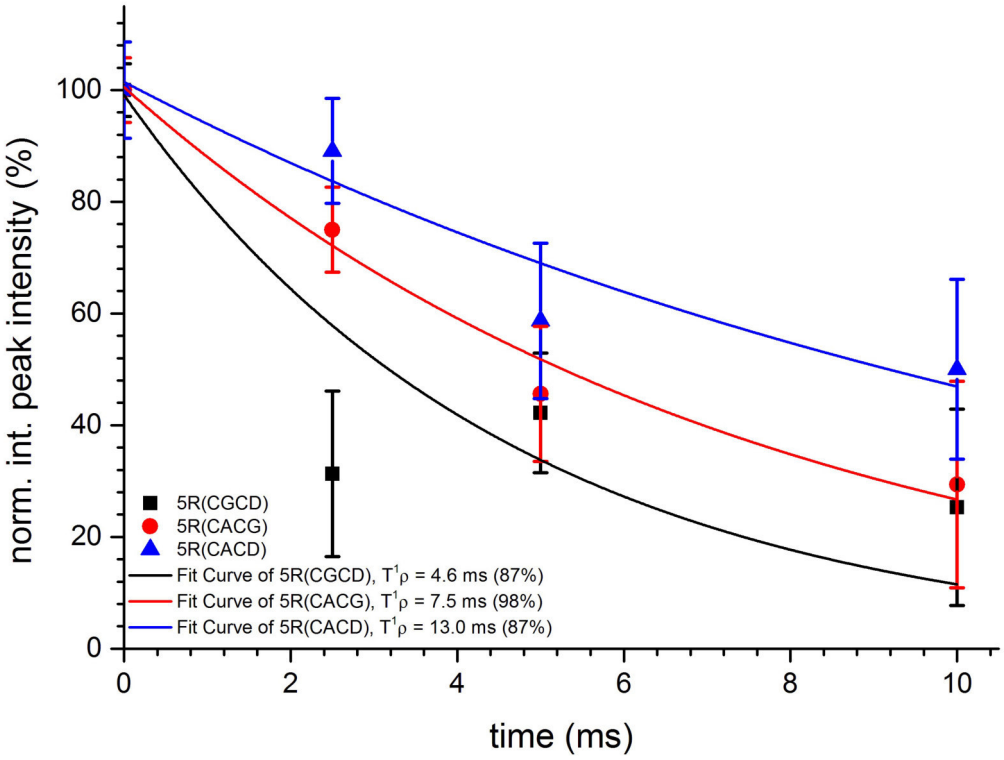

Figure 4.36: Results from PDSD-T_ρ^1-experiments plotted as normalized peak integral of the observed decaying arginine resonances versus the spin lock time (ORIGIN). ^{13}C-T_ρ^1 represents the decay time of each residue during the spin lock. Solvent-exposed Arg5 resonances displayed similar and rather short decay times. R^2_{adj}-values (adjusted coefficient of determination) are given in parenthesis and indicate the quality of the fit.

4.8.2 SPC5-^{13}C-T_ρ^1-experiment

Although suffering from a lower signal to noise ratio compared to PDSD experiments, SPC5 experiments can yield a higher resolution and only show direct contacts of side-chain ^{13}C atoms within one particular residue. During this recoupling method, strong dipolar couplings are exploited instead of the proton network like in PDSD. We used this experiment type to investigate the behavior of several proximal residues in the middle domain of the fibril (Ala21, Val24, Ser26 and Lys28) and the reference spectrum (spin lock time = 0) is shown in figure 4.37. A representative overlay of 1D slices, extracted from the 2D SPC5 spectra at 60.9 ppm, shows the decay of Val24-Cα and Val24-Cβ, respectively (fig. 4.38). From the figure the worse SNR is evident, especially in comparison to the 1D slices of the PDSD spectra (fig. 4.30).
Nonetheless, decay times of Ala21, Val24, Ser26 and Lys28 could be obtained and fitted with a mono-exponential decay, according to the procedure described in the previous subsections.
Interestingly, PDSD and SPC5 measurements showed similar results. As evident from figure 4.39, we found decay times ranging from 3.1 to 11.8 ms. In addition, compared to each other, Ala21, Val24 and Lys28 exhibited similar decay times around 10 ms. Only Ser26 exhibited a faster decay of 3.1 ms. All mono-exponential decay curves exhibited a good reliability towards representing the data, indicated by R^2_{adj} values exceeding 79 %.

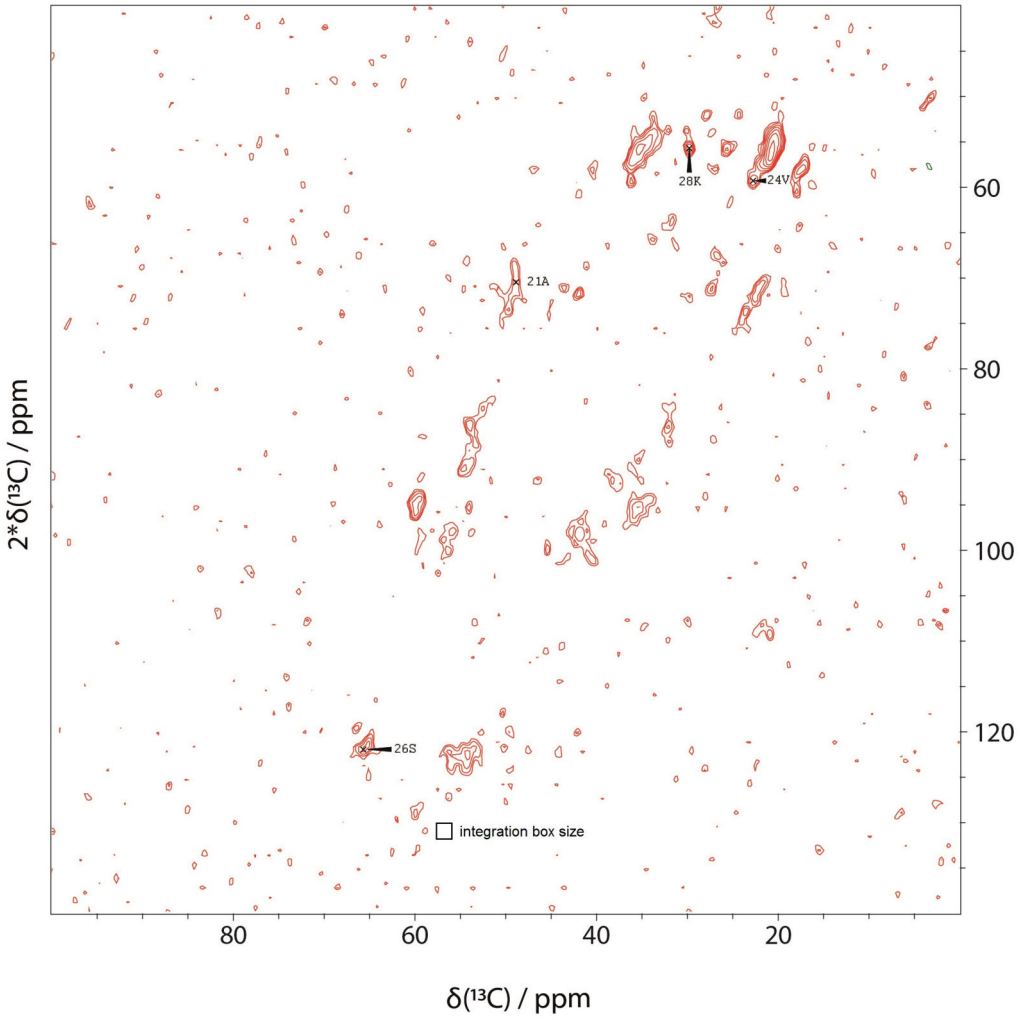

Figure 4.37: 2D SPC5-T_ρ^1 reference spectrum of fibrillar Aβ(1-42) (spin lock time = 0 ms) (SPARKY). The spectrum was recorded at a magnetic field strength of 14.1 T corresponding to a proton Larmor frequency of 600 MHz, a sample temperature of T = 0 ± 5°C and a spinning speed of 8 kHz. For homonuclear ^{13}C-^{13}C mixing, SPC5 was employed. A squared and shifted sine bell function was used for apodization (shift of 0.35π). Assigned resonance peaks were integrated in each spectrum of the spin lock time series. An integration box is displayed in the bottom of the spectrum, covering an area of 1ppm · 1ppm.

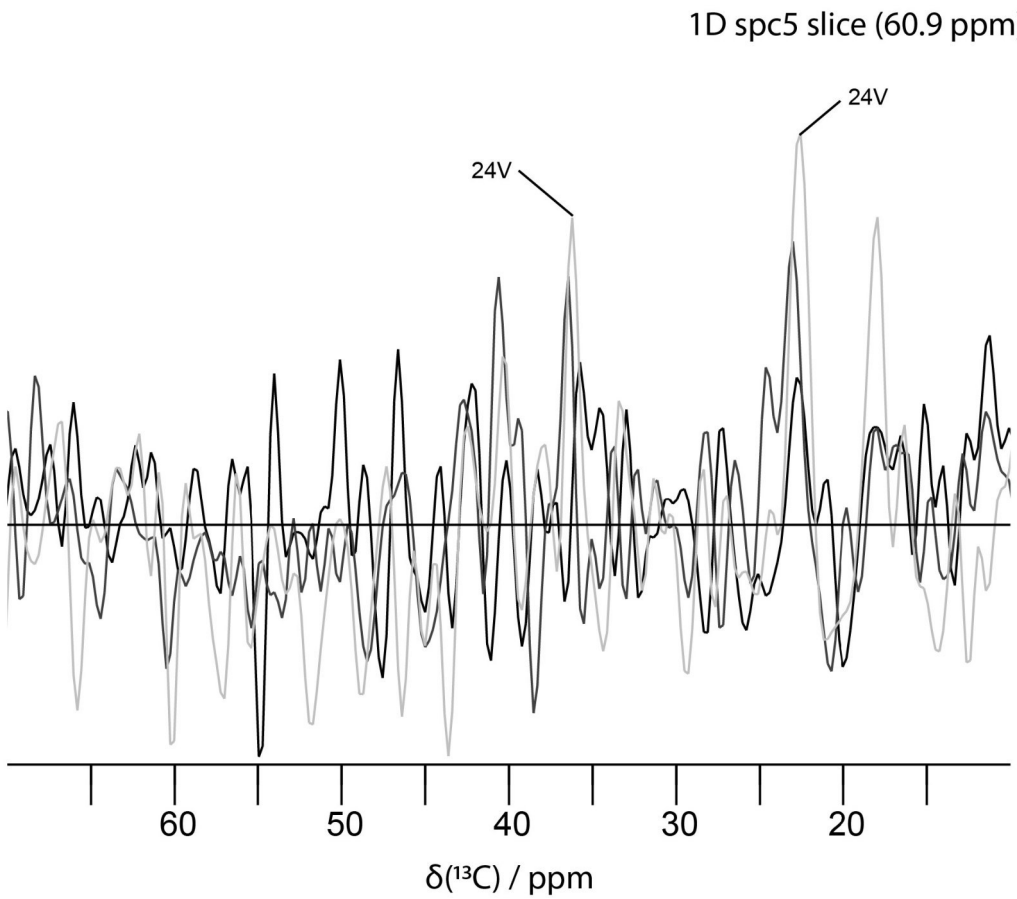

Figure 4.38: Representative 1D overlay plot of SPC5-T_ρ^1 spectra of fibrillar Aβ(1-42) (CCPN). The spectra were recorded at a magnetic field strength of 14.1 T corresponding to a proton Larmor frequency of 600 MHz, a sample temperature of T = 0 ± 5°C, a spin lock field of 36 kHz and a spinning speed of 8 kHz. For homonuclear ^{13}C-^{13}C mixing, SPC5 was employed. A squared and shifted sine bell function was used for apodization (shift of 0.35π). In the reference 1D slice (light-grey) (spin lock time = 0 ms) taken out of a plane of the original 2D spectrum at 60.9 ppm, Val24-Cβ (35 ppm) and Val24-Cγ (21 ppm) resonance peaks are assigned. Darker 1D slice colors indicate longer spin lock times (0, 4 and 8 ms (black), respectively). From the overlayed 1D slices one can clearly observe the intensity loss of Val24-Cβ and Val24-Cγ, laying very near the noise threshold in the black slice (8 ms mixing time). For the final data analysis, resonance signals in 2D spectra were integrated.

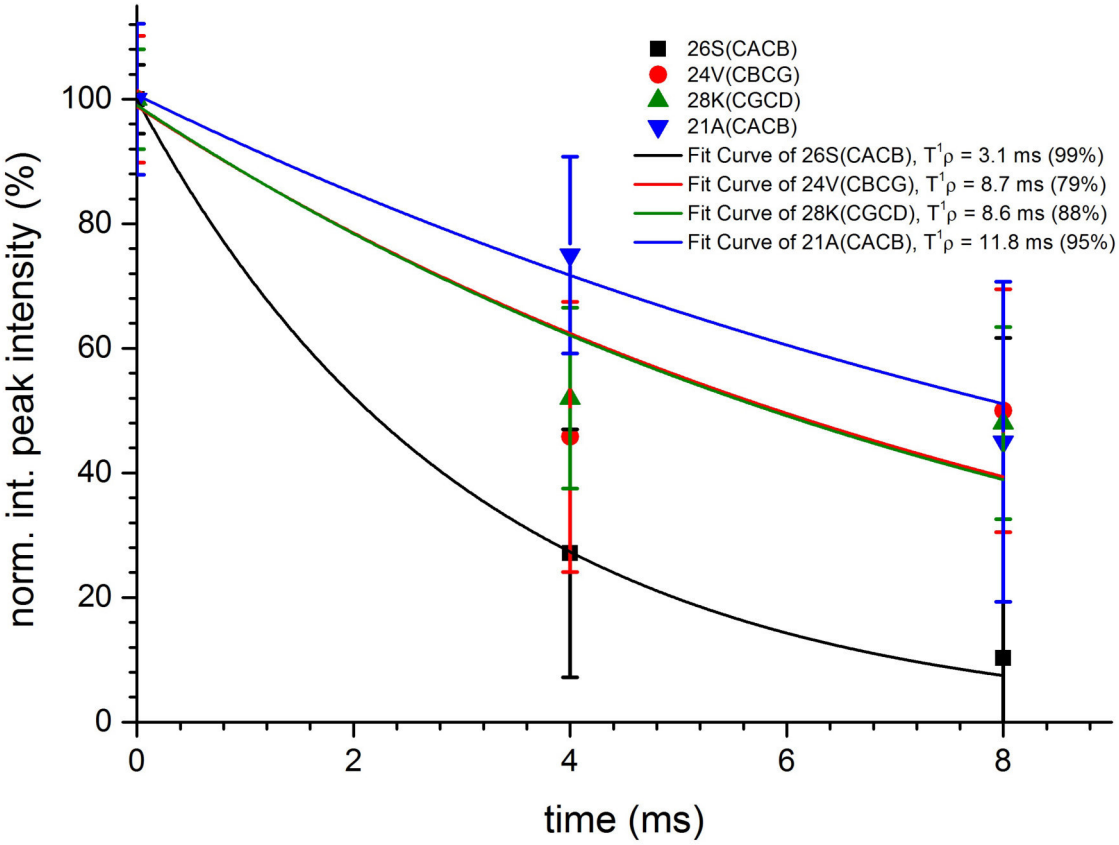

Figure 4.39: Results from SPC5-T_ρ^1-experiment plotted as normalized peak integral of the observed residues versus the spin lock time (ORIGIN). Apparently, Ala21, Val24 and Lys28 shared similar decay times around 10 ms. The Ser26 resonance decayed fast within 3.3 ms. All fitting curves, except for Lys28 (67 %), agreed well with the data (R^2_{adj} values above 90 %).

4.8.3 Discussion

In table 4.2, ^{13}C-T_ρ^1 times of all measurements were presented, color-coded matching to their location in the sequence [N-terminal (blue), middle domain (black), C-terminal (red)]. Additional fitting constants were listed in table 4.3 and 4.4 in the supplement.

2A	**5R**			**8S**
Cα-Cβ	Cα-Cγ	Cα-Cδ	Cγ-Cδ	Cα-Cβ
10.4 ms (85 %)	7.5 ms (98 %)	13.0 ms (87 %)	4.6 ms (87 %)	3.6 ms (91 %)

21A	22E	23D	24V			26S		28K			29G
Cα-Cβ	Cβ-Cδ	Cβ-Cγ	Cα-Cβ	Cα-Cγ	Cβ-Cγ	Cα-Cβ	Cβ-CO	Cβ-Cγ	Cβ-Cδ	Cγ-Cδ	Cα-CO
10.4 ms (85 %) **[11.8 ms, 95** %]	2.7 ms (98 %)	5.0 ms (93 %)	18.1 ms (97 %)	12.8 ms (90 %)	10.2 ms (72 %) **[8.7 ms, 79** %]	6.3 ms (97 %) **[3.1 ms, 99** %]	10.3 ms (99 %)	5.2 ms (98 %)	5.7 ms (97 %)	7.7 ms (97 %) **[8.6 ms, 88** %]	6.0 ms (99 %)

31I		**32I**	**42A**	
Cβ-Cγ1	Cβ-Cδ	Cα-Cγ2	Cα-Cβ	Cα-CO
11.1 ms (79 %)	7.4 ms (95 %)	20.0 ms (91 %)	18.3 ms (95 %)	9.1 ms (77 %)

Table 4.2: PDSD- and SPC5-^{13}C-T_ρ^1 fitting paramaters derived from the fitted decay curves, indicating T_ρ^1-relaxation times. SPC5 derived data were indicated in square brackets and bold, including the adjusted coefficient of determination (R^2_{adj}). R^2_{adj} indicated the quality of the fit. In general, most of the fitting parameters reached reliabilities exceeding 90 %. The color coding matched the position of the particular residue in the sequence (N-terminus blue, middle domain black, C-terminus red). Additional fitting constants were listed in table 4.3 and 4.4 in the supplement.

Apparently, by comparing the average values of all three domains of the protein, a possible trend towards a more rigid C-terminus could be suggested, indicated by the following average values: N-terminus 7.8 ms, middle domain 8.3 ms and C-

terminus 13.2 ms. Nonetheless, slow and fast decay times could be observed in all domains. Furthermore, residual magnetization and spin diffusion during the spin lock times most likely compromised the reliability of the experiments.
Thus, even within the same residue a relatively broad range of decay times could be sampled by intra-residual correlations (Val24 and Arg5).
As derived from the assignment, N-terminal residues were typically low intense in the spectra, requiring a higher number of scans.
In the middle domain, the average ^{13}C-T_ρ^1 did not significantly exceed the average of the N-terminus. However, some solvent-exposed side-chains displayed rather short decay times, congruent with our expectation of an enhanced mobility (Glu22, Asp23, Lys28).
The C-terminal residues Ile31-Cα-C$C\beta$ and Ile32-Cα-C$C\gamma$1 resonances located in the hydrophobic S-shaped core displayed build-up of magnetization and could not be fitted with a mono-exponential decay function. The majority of isoleucine residues, which could be fitted, displayed a range of decay times. Same held true for the two C-terminal Ala42 resonances displaying one rather slow and one intermediate decay time.
Similar decay times in the PDSD and SPC5 experiments could be obtained for Ala21, Val24 and Lys28, within the errors of the experiment. For Ser26-Cα-Cβ, the detected decay times differed slightly more.
For future experiments, coherent effects should be further suppressed by spinning frequencies exceeding 45 kHz, utilizing fast-MAS probes. Furthermore, measuring at higher static magnetic fields would ensure a higher resolution leading to more unambiguous assignments and more measurement sites to study trends in the three different compartments of the fibril. In this study, the majority of observed residues were residues with isolated and unique shifts.
Moreover, it could be advantageous to employ longer spin lock times, to measure the complete decay of the intensities. Finally, it would be interesting to study the effects of coherent processes and their contribution to the measurements in dependence of spinning speed, spin lock field strength and proton decoupling. Here, it could be advantageous to employ deuterated samples, which would reduce the number of highly coupled protons. Lastly, it could be advantageous to measure the decay curves at different spin lock fields and different spinning speeds.

4.9 Water-edited experiments

After the cryoEM measurements were analyzed and revealed the complete structure of fibrillar Aβ(1-42), we discussed the possibility of observing surface near residues in ssNMR spectra. To achieve this goal, we employed water-edited CP, PDSD and SPC5 experiments, augmented with a selective proton dephasing, refocussing and longitudinal mixing step, as previously mentioned in section 3.2.3.
We adapted the approach utilized by C. Ader et al. to study membrane proteins and adjusted the applied pulse sequence to our needs, yielding a water-edited CP (1D and 2D), PDSD and SPC5 experiment [102].
An interesting feature about lysine side-chains could be investigated in a more recent study, supported by data investigating the effect of magnetization transfer by proton exchange: It has been proposed that fast lysine side-chain exchange rates are induced by a fast chemical exchange rates between amine and water protons, exceeding the rate between amide and water protons [142,143]. This led to an even faster polarization of solvent-exposed lysine side-chains, compared to the backbone atoms. In addition, two studies could indepently prove that water molecules can be discriminated into at least two types: bulk and crystal water [144,145]. Both water types exhibit different polarization transfer characteristics. Even though bulk water surrounds a lot of surface residues, it does not contribute significantly to spin diffusion, resulting in slow transfer rates [144, 146]. Highly coordinated crystal water on the other hand, has a larger contribution. Keeping these features in mind, we started setting up our experiments.
In the beginning of the experiments, proton spins were excited with an initial 90° pulse. Afterwards a spin echo followed, dephasing all proton spins by dipolar dephasing. Remarkably, only spins with strong dipolar couplings were dephased in the echo periods (τ) lasting 500 µs (fig. 3.1). Consequently, mobile water protons maintained their polarization. Next, there was no cross polarization signal detectable on the heteronucleus ^{13}C.
By augmenting the pulse sequence with a longitudinal proton mixing step, the residual polarization on mobile water protons was transferred to protons with strong dipolar couplings, namely protons most likely associated or coordinated by solvent-exposed side-chains of the fibril. A subsequent CP step transferred polarization from the coordinated protons to the fibril ^{13}C nuclei, located on the periphery of the fibril. By increasing the proton mixing time, we could measure build up curves of carbon resonances located close to the fibril surface.
To find out the required mixing time, to observe all resonances present in the un-edited CP, we started with 1D CP measurements. We found out, after approximately 6.5 ms all signals could be detected in the CP spectrum (fig. 4.40 and 4.41). However, this time period only indicated a fraction of the original intensity found in the un-edited CP, far away from the maximum intensity. Afterwards we

acquired a 2D ^{1}H-^{13}C correlation experiment, to identify residues being in direct contact with both buffer solvents H_2O and ACN, respectively (fig. 4.42). Subsequently, we acquired water-edited PDSD-, as well as SPC5-spectra for the detection of resonance-specific build-up curves, similar to the procedure utilized in the ^{13}C-T_ρ^1 analysis. Likewise, as for the 2D PDSD and SPC5 spectra in the previous section, the normalized peak intensities of the assigned residues were integrated in Sparky and plotted against the proton mixing time.

4.9.1 Water-edited CP

1D

To examine the necessary proton mixing time to observe all resonance signals detected in CP spectra without water-editing, we acquired proton mixing time arrays (see fig. 4.40). Here, we could observe a restored CP spectrum after ~ 6.5 ms, although only at ~ 30% of the intensity of the unedited CP spectrum (see fig. 4.41). From that time on, only small intensity changes of aliphatic, aromatic and carboxyl resonances could be observed, which could be attributed to the relative low amount of scans (16), which were the same in each 1D water-edited CP spectrum.
Afterwards, the water-edited CP was compared to a reference CP experiment with the same number of scans (16), to check if the same resonance signals were detectable after 6.5 ms. This could be confirmed, since the same resonance signals could be resolved as previously obtained in the reference CP spectrum without water-editing (see fig. 4.41). However, the SNR was worse in the water-edited CP, due to the short proton mixing period.
These experiments laid the foundation for the detection of the initial points of water-build-up curves.

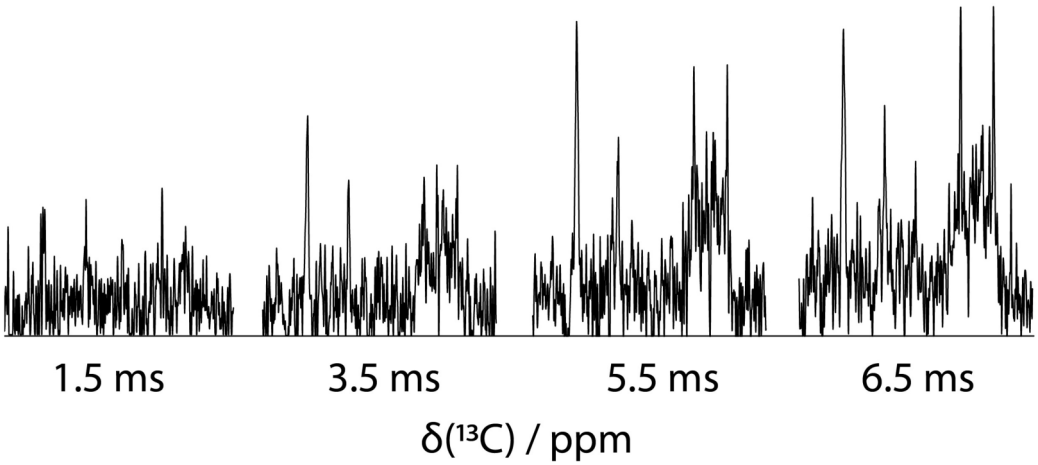

Figure 4.40: Water-edited CP spectra of fibrillar Aβ(1-42). The spectra were recorded at a magnetic field strength of 14.1 T corresponding to a proton Larmor frequency of 600 MHz, a sample temperature of T = 0 ± 5°C and a spinning speed of 11 kHz. For homonuclear ^{1}H- ^{1}H mixing, longitudinal mixing with an incremented mixing time was employed. A squared and shifted sine bell function was used for apodization (shift of 0.5π). CP spectra with increasing proton mixing times are shown side by side and scaled to the same noise level by hand, since the number of scans was the same in each spectrum. The proton mixing time to replenish the signal on ^{13}C, in order to detect the same signals as observed in CP spectra without water editing, was obtained to be roughly 6.5 ms (see fig. 4.41).

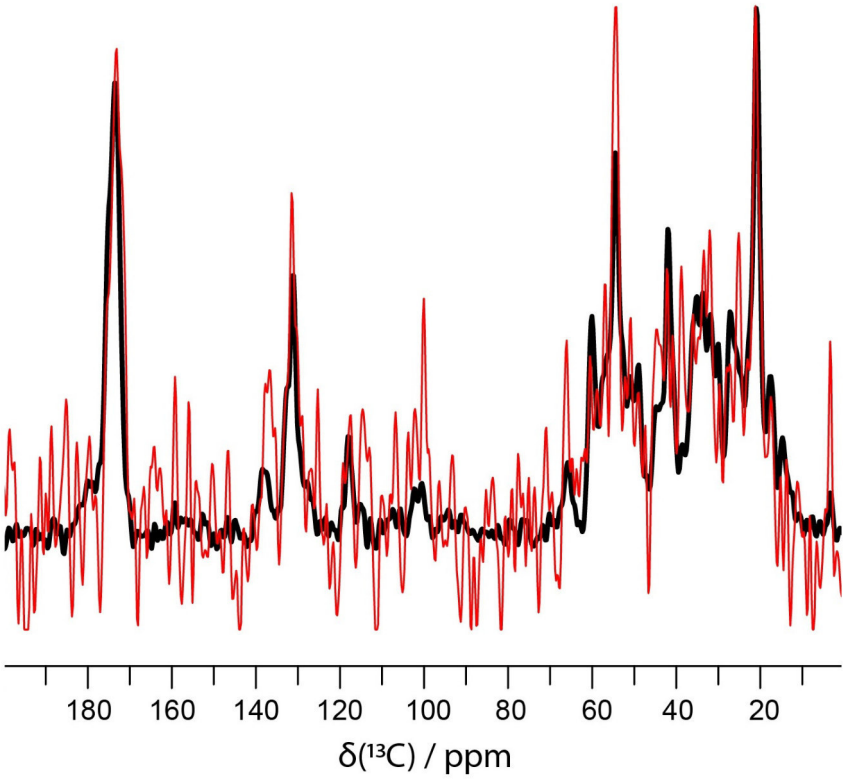

Figure 4.41: Water-edited CP spectrum (red) and reference CP spectrum without water-editing (black) of fibrillar Aβ(1-42). The spectra were recorded at a magnetic field strength of 14.1 T corresponding to a proton Larmor frequency of 600 MHz, a sample temperature of T = 0 ± 5°C and a spinning speed of 11 kHz with 16 scans. For homonuclear ^{1}H- ^{1}H mixing in the water-edited CP spectrum (red), longitudinal mixing with 6.5 ms mixing time was employed. A squared and shifted sine bell function was used for apodization (shift of 0.5π) for both spectra. Upon comparison, the same resonance signals could be observed in the red spectrum, as previously observed in the black reference spectrum. Obviously, the SNR was worse in the red spectrum (~ 70% less), due to the short longitudinal proton mixing.

2D

After we compared different proton mixing times, we continued with a ^{1}H-^{13}C 2D correlation experiment. In this experiment, we wanted to observe if all carbon regions were in contact with the solvent interface after a proton mixing time of 6.5 ms (see fig. 4.42). Furthermore, we wanted to investigate, which solvent molecules transferred the most polarization to the protein ^{13}C-nuclei.
We could detect cross-peaks with the water at ~ 4.5 ppm, as well as with acetonitrile (ACN) at ~ 1.8 ppm. Corresponding to our expectation of observing all ^{13}C-resonances after a proton mixing time of ~ 6.5 ms, aliphatic, aromatic and carboxyl resonances were detectable. Even the Cζ-side-chain resonances of Arg5 and Tyr10 could be observed at ~ 159 ppm. In regards to the ACN line, which was approximately 20 times weaker in intensity compared to the H_2O-line, only weak aliphatic and carboxyl correlations could be obtained. Apparently, proton exchange, hydrogen bonds and coordination of water molecules around charged residues facilitated the polarization transfer.
In addition, the amount of ACN was originally 30% by volume in the buffer and could have decreased since the filling of the rotor due to evaporation. To conclude, we could confirm the result of the previous measurements, identifying the protein being in contact with the surrounding solvents.

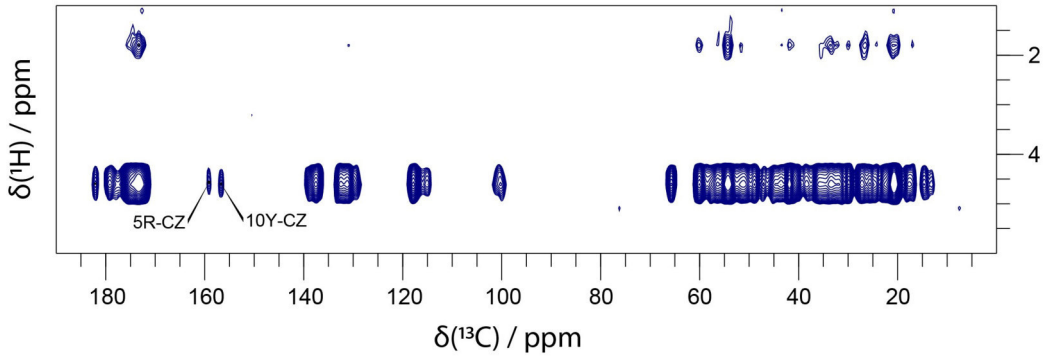

Figure 4.42: Water-edited HC 2D correlation spectrum of fibrillar Aβ(1-42). The spectrum was recorded at a magnetic field strength of 14.1 T corresponding to a proton Larmor frequency of 600 MHz, a sample temperature of T = 0 ± 5°C and a spinning speed of 11 kHz. For homonuclear proton-proton mixing, longitudinal mixing with a mixing time of 6.5 ms was employed. A squared and shifted sine bell function was used for apodization (shift of 0.35π). The water line, visible at ~ 4.5 ppm shows cross-correlations to carbon resonances in the aliphatic, aromatic and carboxyl region, as expected from the 1D CP spectra recorded previously. Moreover the Arg5- and Tyr10-Cζ-resonances were detectable. On the ACN line, visible at ~ 1.8 ppm, only aliphatic and carboxyl resonances were visible related to the much lower SNR, due to the lower amount of ACN in the solvent.

4.9.2 Water-edited PDSD

Water-edited PDSD spectra were acquired as time series with increasing proton mixing times. The reference spectrum was a PDSD experiment with a proton mixing time of 3.25 ms (fig. 4.43). During the incrementation of the proton mixing time, the resonance signals of solvent-exposed residues gained intensity, observable in an intensity build-up. For a better understanding of the build-up, representative 1D strip plots showed the intensity gain of Glu3-Cα and -Cβ correlations (fig. 4.44). In this figure, three different spectra were shown, with increasing proton mixing times. The darker the 1D slice got, the more advanced was the proton mixing time, leading to a signal build-up. All assigned peaks were integrated in each spectrum of the time series and afterwards normalized with the maximum integral value. Finally, the normalized integrated peak intensities were plotted against the proton mixing time.
Since the maximum mixing time ended at 10 ms, reliable trends could not be derived [142]. Furthermore, low SNRs aggravated the significance of the results.
Quantitatively, we could detect strong Lys28 signals in the spectra, whereas the measured trajectories of the detected correlations were not indicative of the expected build-up (fig. 4.45).
Likewise, resonance signals of Glu3, Arg5, Asp7 and Ser26 (fig. 4.46), did not show a build-up in the very short proton mixing time range.
Keeping in mind the contribution of the two different water pools, we continued with the acquisition of water-edited SPC5 recoupled experiments. Here, we expected a less dominant effect of longitudinal mixing, due to the different recoupling method.
Moreover, this approach was intended to validate the conclusions derived from the PDSD experiments.

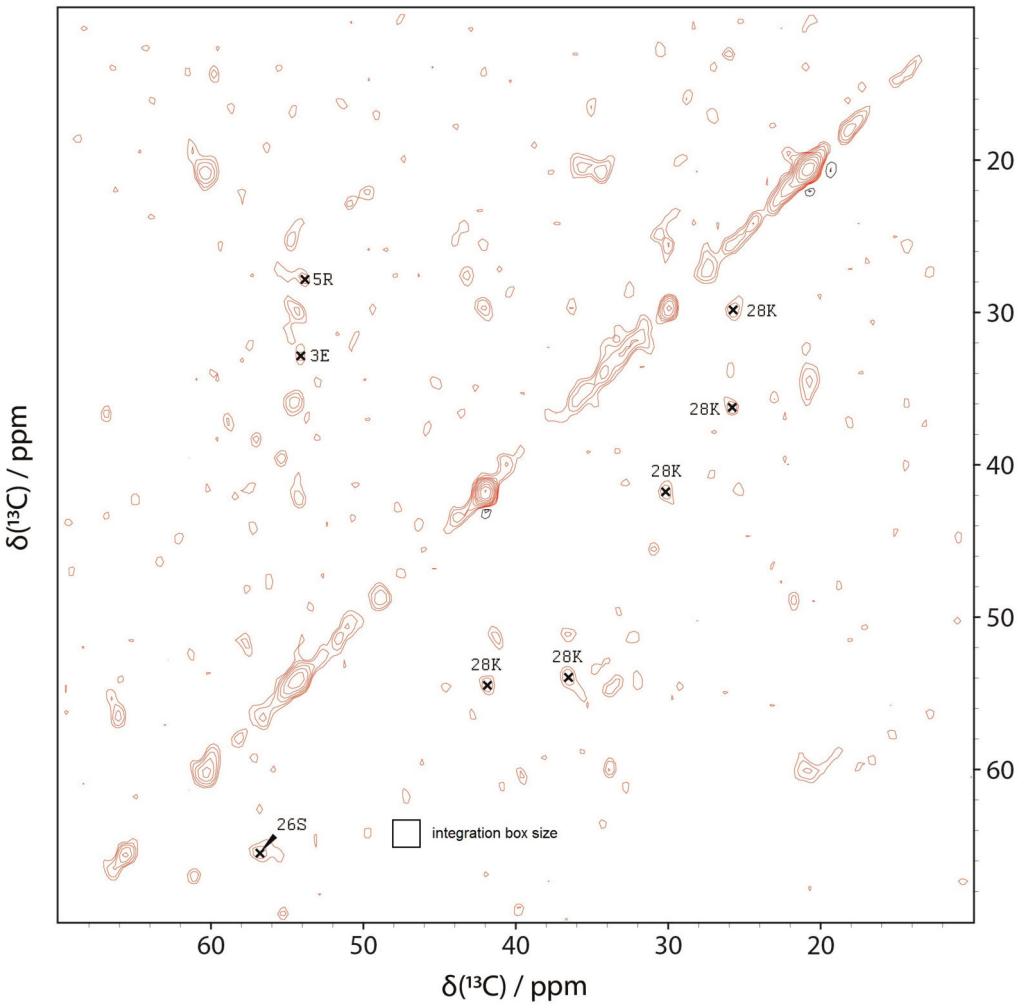

Figure 4.43: 2D Proton-Driven Spin Diffusion (PDSD)-water-edited spectrum of fibrillar Aβ(1-42) (SPARKY). The spectrum was recorded at a magnetic field strength of 14.1 T corresponding to a proton Larmor frequency of 600 MHz, a sample temperature of T = 0 ± 5°C, a spinning speed of 11 kHz and a longitudinal proton mixing time of 3.25 ms. For homonuclear ^{13}C-^{13}C mixing, PDSD with a mixing time of 50 ms was employed. A squared and shifted sine bell function was used for apodization (shift of 0.35π). Assigned resonance peaks were traced over the incremented proton mixing time and were afterwards integrated.

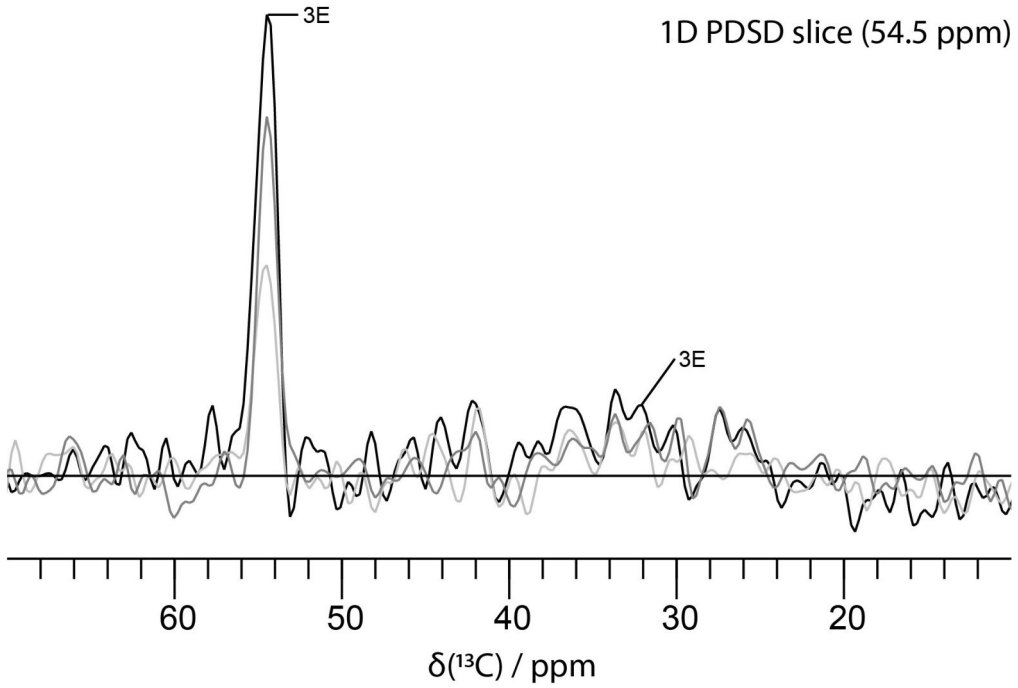

Figure 4.44: Representative 1D overlay strip plot of water-edited Proton-Driven Spin Diffusion (PDSD) spectra of fibrillar Aβ(1-42) (CCPN). The spectra were recorded at a magnetic field strength of 14.1 T corresponding to a proton Larmor frequency of 600 MHz, a sample temperature of T = 0 ± 5°C and a spinning speed of 11 kHz. For homonuclear ^{13}C-^{13}C mixing, PDSD with a mixing time of 50 ms was employed. A squared and shifted sine bell function was used for apodization (shift of 0.35π). In the reference 1D slice (light-grey) (proton mixing time = 3.25 ms) taken out of a plane of the original 2D spectrum at 54.5 ppm, Glu3-Cα (54.5 ppm) and Glu3-Cβ (32 ppm) resonance peaks are assigned. Darker 1D slice colors indicate longer proton mixing times (3.25, 6.5 and 10 ms (black), respectively). From the overlayed 1D slices one can clearly observe the intensity gains of Glu3-Cα and Glu3-Cβ. For the final data analysis, resonance signals in 2D spectra were integrated.

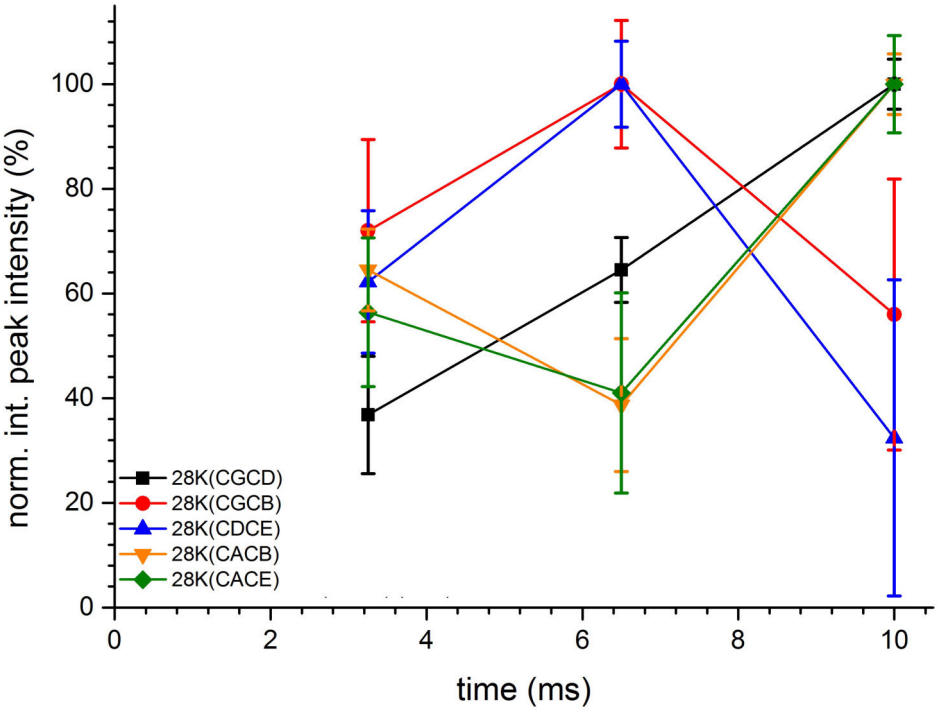

Figure 4.45: Results from water-edited PDSD experiments plotted as normalized peak integral of the observed residues versus increasing proton mixing times (ORIGIN), lines were only intended to guide the eye. The highest-measured intensity of each signal, which was detected in the series of three experiments, was set to 100%. On the whole, the detection of a build-up curve was impeded by the low SNR, as well as the short proton mixing times.

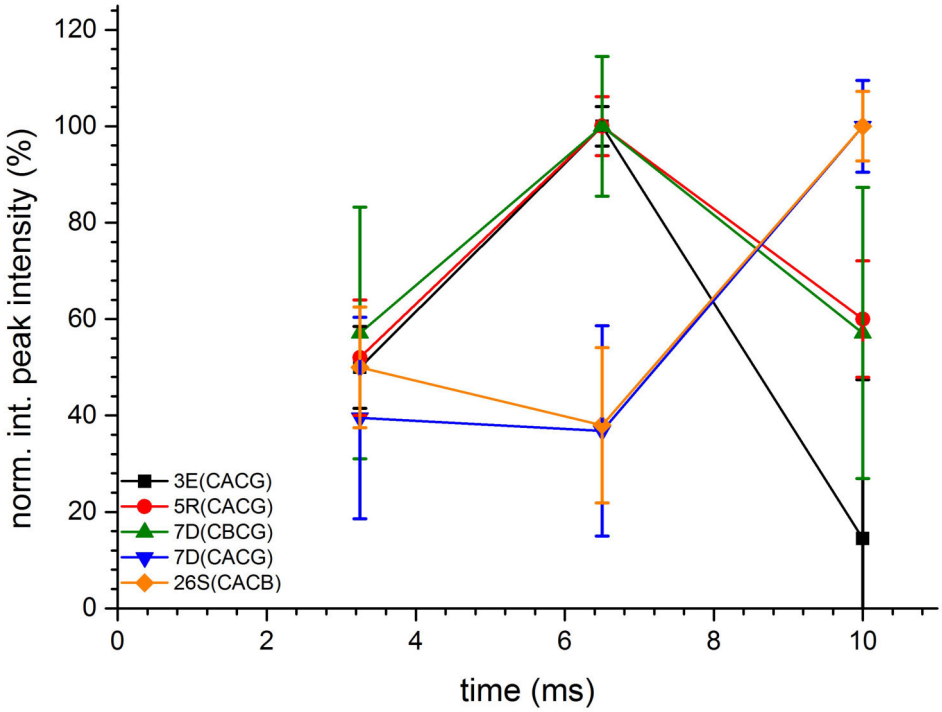

Figure 4.46: Results from water-PDSD experiments plotted as normalized peak integral of the observed residues versus increasing proton mixing times (ORIGIN), lines were only intended to guide the eye. The highest-measured intensity o each signal, which was detected in the series of three experiments, was set to 100%. Similarly, as detected before, low SNR and too little proton mixing times hampered the detection of build-up curves.

4.9.3 Water-edited SPC5

After the acquisition of water-edited PDSD spectra, we switched to acquiring water-edited SPC5 spectra, to check our findings. To detect the steady build-up of the solvent-exposed residues of the fibril, ^{1}H-^{1}H mixing times were incremented from 3 to 6 ms.
Again, like in the water-edited PDSD, the complete magnetization of the strongly coupled protons was dephased and by applying a subsequent incremented proton mixing step we transferred the left-over magnetization from the water protons to the fibril surface protons. Afterwards a CP step and SPC5 mixing followed.
Due to too short proton mixing times, only the very start of the potential build-up curve was detected. Additionally, the low SNR complicated the reliability of the results.
In figure 4.47, a 2D SPC5 spectrum, recorded with a proton mixing time of 3 ms was shown. For a better understanding of the build-up, a representative overlay of 1D slices, showed the relatively small intensity build-up of Val24-Cβ and -Cγ correlations (fig. 4.48). In this figure, the spectrum with the lowest proton mixing time was shown in light-grey, representing the minimum intensity. The darker the 1D slice got, the more advanced was the proton mixing time, leading to a signal build-up. All assigned peaks were integrated in each spectrum of the time series and afterwards normalized with the maximum integral value. Finally, the normalized integrated peak intensities were plotted against the proton mixing time.
For Gln15 and Lys28 a rising curve could be detected (fig. 4.49). Nonetheless, there were two sudden intensity jumps in both datasets at 5 ms for Lys28 and 6 ms for Gln15, respectively. Remarkably, the sudden intensity gain of Gln15 at 6 ms, was observed for residues Ala21, Val24 and Ser26, too (fig. 4.50). Additionally, the latter three residues demonstrated the same build-up trajectory as Gln15, although their mean values exhibited lower fluctuations compared to the mean value of Gln15.

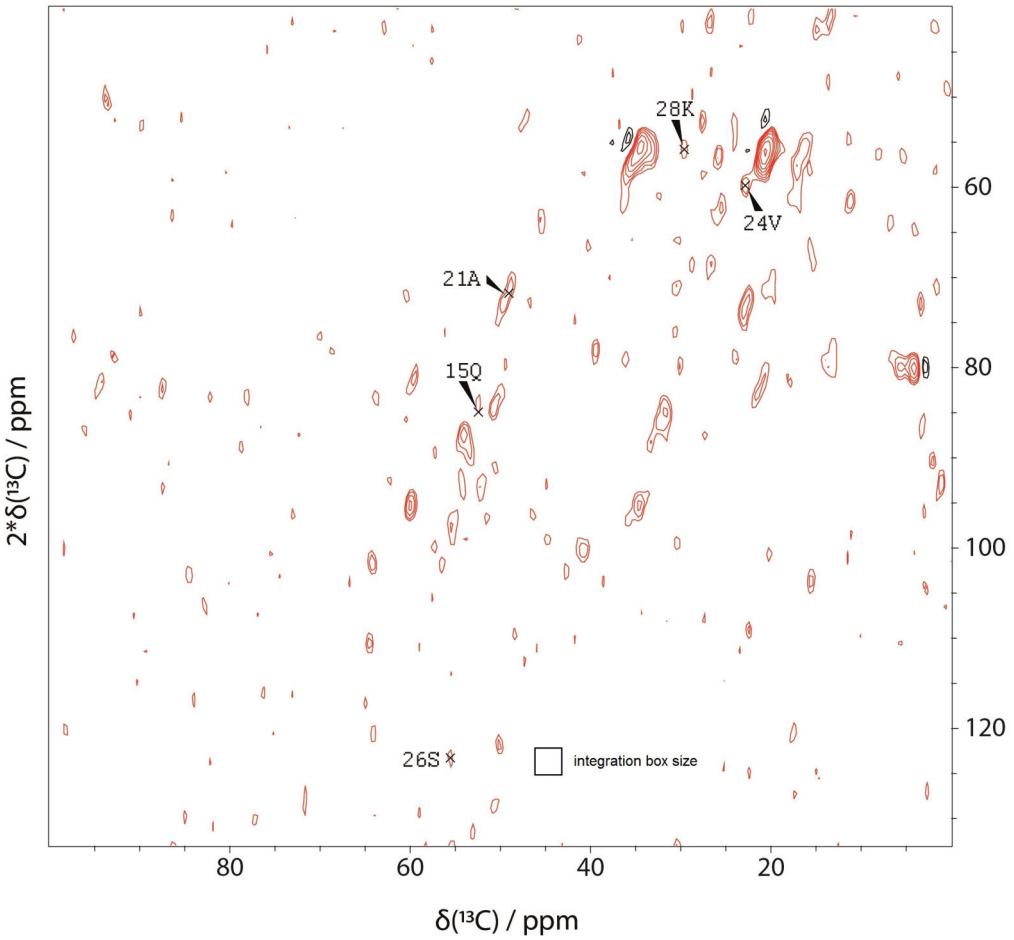

Figure 4.47: 2D SPC5-water reference spectrum of fibrillar Aβ(1-42) (SPARKY). The spectrum was recorded at a magnetic field strength of 14.1 T corresponding to a proton Larmor frequency of 600 MHz, a sample temperature of T = 0 ± 5°C, a spinning speed of 8 kHz and a proton mixing time of 3.25 ms. For homonuclear ^{13}C-^{13}C mixing, SPC5 was employed. A squared and shifted sine bell function was used for apodization (shift of 0.35π). Assigned resonance peaks were traced over the incremented proton mixing time and were afterwards integrated.

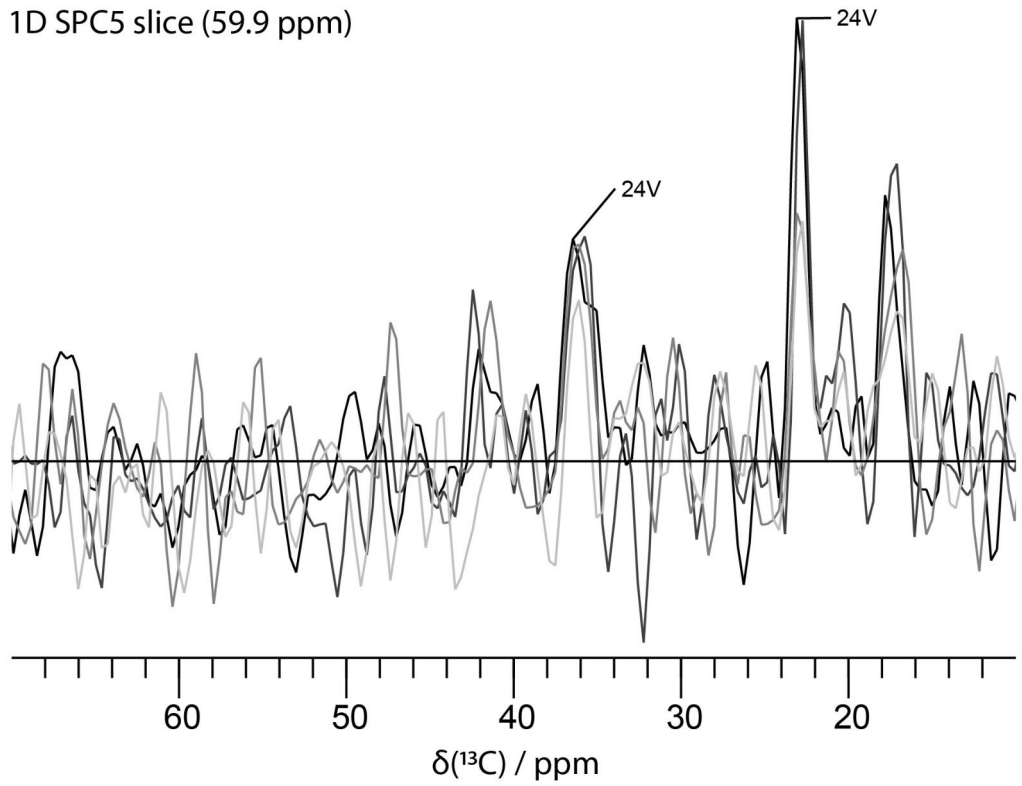

Figure 4.48: Representative 1D overlay strip plot of water-edited SPC5 spectra of fibrillar Aβ(1-42) (CCPN). The spectra were recorded at a magnetic field strength of 14.1 T corresponding to a proton Larmor frequency of 600 MHz, a sample temperature of T = 0 ± 5°C and a spinning speed of 8 kHz. For homonuclear ^{13}C-^{13}C mixing, SPC5 was employed. A squared and shifted sine bell function was used for apodization (shift of 0.35π). In the reference 1D slice (light-grey) (proton mixing time = 3 ms) taken out of a plane of the original 2D spectrum at 59.9 ppm, Val24-Cβ (36.7 ppm) and Val24-Cβ (23 ppm) resonance peaks are assigned. Darker 1D slice colors indicate longer proton mixing times (3, 4, 5 and 6 ms (black), respectively). From the overlayed 1D slices one can clearly observe the intensity gains of Val24-Cβ and Val24-Cβ. For the final data analysis, resonance signals in 2D spectra were integrated.

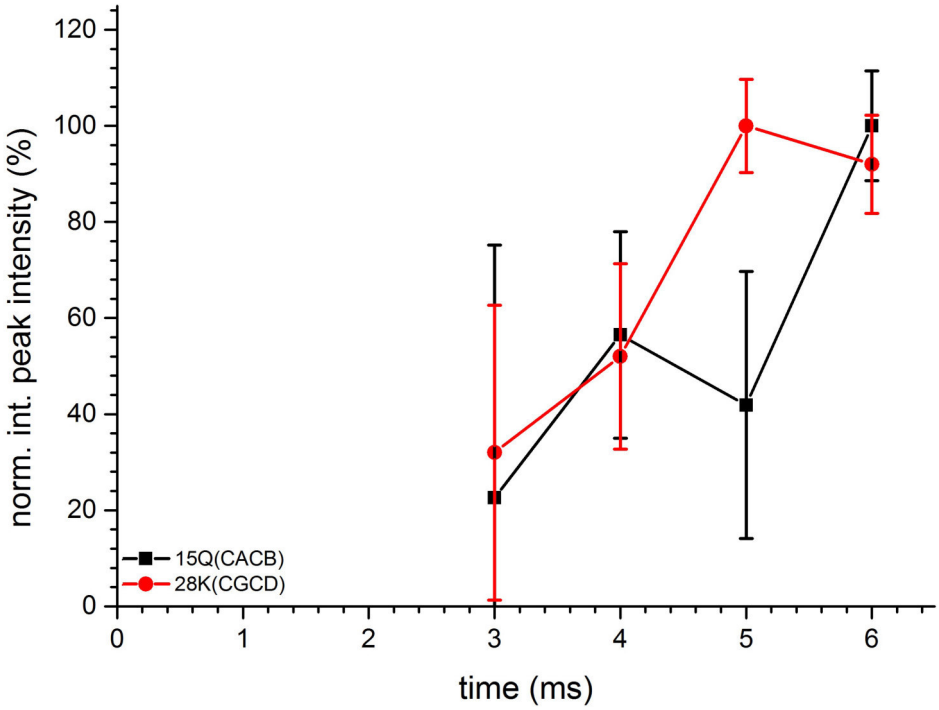

Figure 4.49: Results from water-edited SPC5 experiments plotted as normalized peak integral of the observed residues versus increasing proton mixing time (ORIGIN), lines were only intended to guide the eye. The highest-measured intensity of each signal, which was detected in the series of four experiments, was set to 100%. We could detect the very beginning of an increasing intensity of Gln15 and Lys28 resonances.

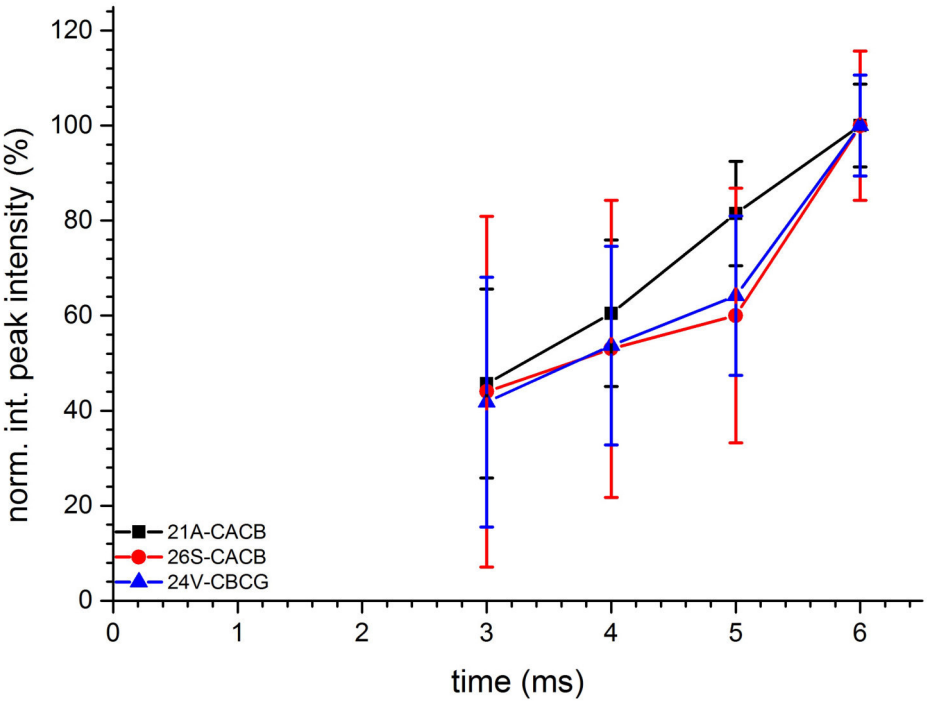

Figure 4.50: Results from water-edited SPC5 experiments plotted as normalized peak integral of the observed residues versus increasing proton mixing time (ORIGIN), lines were only intended to guide the eye. The highest-measured intensity of each signal, which was detected in the series of four experiments, was set to 100%. Ala21, Val24 and Ser26 showed a steady increase, too.

4.9.4 Discussion

Beginning with 1D CP measurements, we could detect a build-up of magnetization in the water-edited spectra, leading to the observation of all signals detected in the un-edited CP spectra previously. By augmenting the CP experiment with a proton evolution period, we could prove aliphatic, aromatic and caboxyl groups of the protein were in contact with water protons, supporting the previous result.
Continuing with water-edited 2D PDSD experiments and upon closer examination of the reference PDSD spectrum, we could observe that only residues with exchangeable protons were unambiguously assignable after a longitudinal ^{1}H- ^{1}H mixing time of 3.25 ms (fig. 4.43). This result indicated a high dependence of the polarization transfer on proton exchange, as previously observed by Lv et al. and Wang et al. [142,145]. In detail, polarization was transferred by exchangeable protons in the hydroxy groups of Glu3, Asp7 and Ser26, the guanidinium group of Arg5, as well as the amine group of Lys28. Since several high-intense Lys28 resonances could be observed, the fast chemical exchange rates between amine and water protons played a crucial role in polarizing several residues along the Lys28 side-chain (Cα-Cβ, Cβ-Cγ, Cγ-Cδ, Cδ-Cϵ and Cα-Cϵ). Moreover, the Lys28-Cγ-Cδ resonance was detectable in the water-edited SPC5 experiment, too.
In the water-edited SPC5 experiments, increasing intensities could be observed, probably attributed to the shorter final proton mixing time of 6 ms.
Interestingly, even inward-facing residues in steric-zippers were assignable, like Gln15, Ala21 and Val24. Detecting Ala21 and Val24 resonances could be related to an enhanced polarization transfer by exchanging protons of Glu22 and Asp23 hydroxy side-chains. In the case of Gln15, the detection might be facilitated by a polarization transfer of Lys16 amine protons. However, aliphatic and carboxyl resonances of Lys16, Glu22 and Asp23 could not be assigned, whereas Lys16 was typically low-intense, even in the spectra without water-editing.
On the whole, the relatively short incrementation intervals, only sampled initial points of the the build-up curve far below a constant stage of saturation. This could be concluded from previous work focusing on water-edited polarization build-ups using final proton mixing times of $\geq$ 100 ms [106,142,147]. With this approach, diffusion constants of solvent-exposed and inward-facing residues could be included in a theoretical model, allowing for numerical simulations, which could be compared to the experimental data. In addition, effects of the water-protein surface area and the protein volume could be considered too, if datasets of entire build-up curves should be fitted.
Furthermore, even mixing times of only 3 ms led to the rise of several unassignable resonances due to spectral overlap, as observed in water-edited PDSD and SPC5 experiments. At this point, a repetition of the experiments at higher magnetic field strengths and longer proton mixing times might be helpful, which is work

in progress.
In addition, choosing SPC5 recoupling yielded the possibility of observing residues located in steric zippers within the fibril core, however at the cost of prolonged measurement times.
In that perspective, another fruitful approach would be the detection of ^{15}N-^{13}C-correlation experiments, succesfully applied previously [142, 147]. By using this approach, the proton exchange rates of solvent-exposed residues containing ^{15}N-atoms could be examined, including the determination of salt-bridges. These results could also give detailed insight into the dynamics of the polarization transfer of the side-chain nitrogen atoms, compared to the backbone nitrogen atoms.
Furthermore, employing longer mixing times to detect the complete build-up curve and fit it to the theoretical model might yield better results. By doing so, relaxation effects could be included in the model, too. This would provide even more information concerning the mobility of the residues, again in relation to salt-bridges, as well as hydrophobic clusters and hydrogen bonds in β-strands.

4.10 ThT binding experiments

As mentioned in the introduction, ThT is a suitable marker to measure aggregation kinetics of amyloidogenic proteins. Likewise congo red staining indicates the presence of amyloid fibrils. Binding of congo red to the amyloid fibril formed by the HET-s proteins has previously been described by A. Schütz et al. [148]. In this study, the binding site between congo red and the fully deuterated HET-s fibril was presented. Using this study as a reference, we started with fibril surface measurements and investigated the binding of Thioflavin T (ThT) to reproduced Aβ(1-42) fibrils.
Peak shifts were predicted to appear for residues located in the end of the second β-strand of the fibril in the onset of the loop, more precisely Val18 to Glu22. These insights were provided by molecular dynamics simulations, carried out by Holger Gohlke and Benedikt Frieg.
However, no peak shifts within the measured linewidths could be detected at low ThT (20 $\mu\frac{mol}{l}$) nor at high ThT concentrations (800 $\mu\frac{mol}{l}$).
These results could be explained by previously published results, showing a binding of ThT to fibrils can be impeded by a low pH value [149,150]. Since our sample has a pH of 2, even the addition of excess ThT showed no effect of binding on a molecular scale. Nonetheless, we did not investigate if there were any macroscopic deviations in the fibrils.
Similar chemical shifts in flat and twisted fibril morphologies have previously been observed for β-endorphin fibrils [151]. The generation of two different polymorphs with similar chemical shifts, was caused by different salt concentrations in the fibril growth medium containing the β-endorphin monomers. Since only the small ligand ThT was added to the buffer medium of the fibrils, one would probably not expect big macroscopic structural variations. Nonetheless, to check if there are macroscopic deviations, negative-stain transmission electron microscopy, scanning transmission electron microscopy or atomic force microscopy might be helpful.

4.10.1 Low ThT concentration

First and foremost, we started with a ThT concentration of 20 $\mu\frac{mol}{l}$ to investigate, wether a binding takes place or not. As we can see from the overlay of the reference spectrum and the ThT-Aβ(1-42) spectrum, there were no chemical shift perturbations detectable (fig. 4.51).

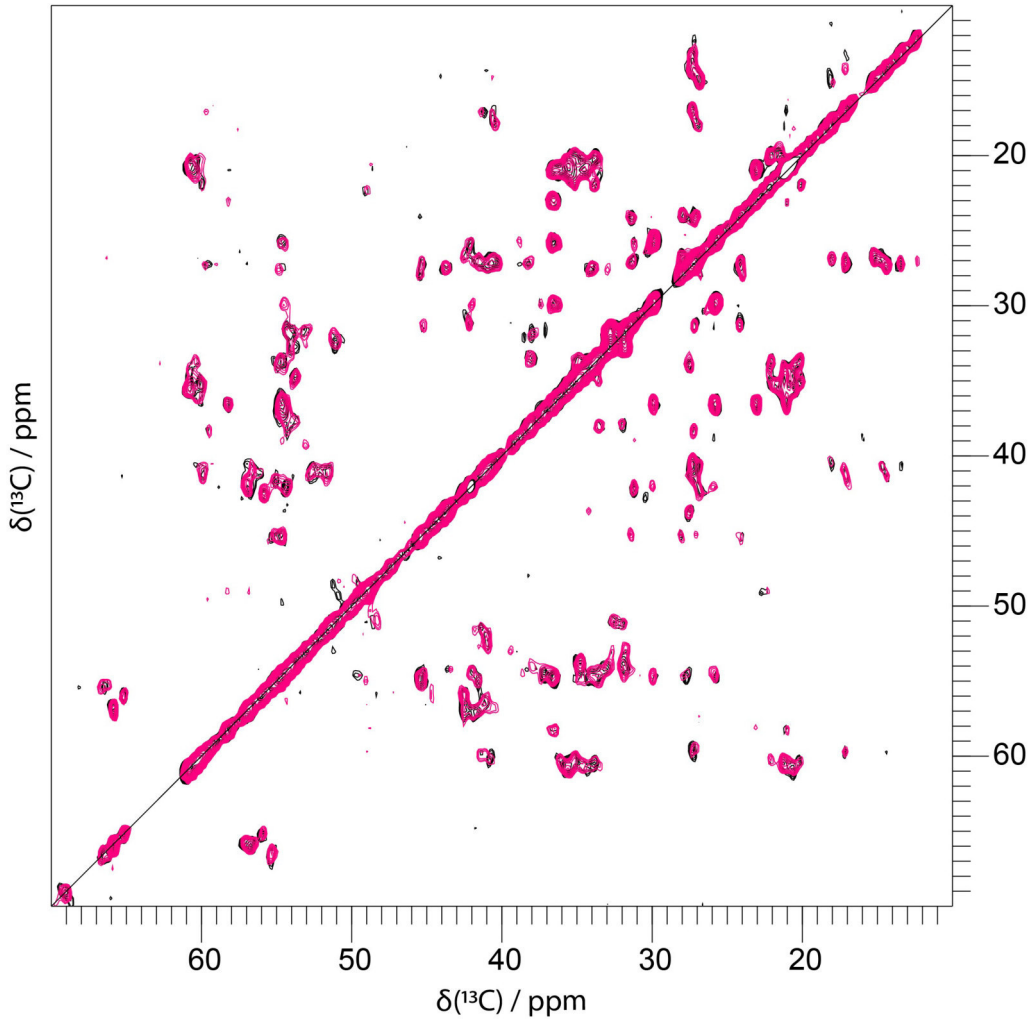

Figure 4.51: Overlay of Proton-Driven Spin Diffusion (PDSD) spectra of fibrillar Aβ(1-42) (pink) and fibrillar Aβ(1-42) with 20 $\mu\frac{mol}{l}$ ThT (black) (CCPN). Both spectra were recorded at a magnetic field strength of 18.8 T corresponding to a proton Larmor frequency of 800 MHz, a spinning speed of 12.5 kHz and a sample temperature of T = 0 ± 5°C. For homonuclear ^{13}C-^{13}C mixing, PDSD with a mixing time of 20 ms was employed. A squared and shifted sine bell function was used for apodization (shift of 0.35π). No chemical shift perturbations could be detected.

4.10.2 High ThT concentration

We repeated the previous experiment with a ThT concentration of 800 $\mu\frac{mol}{l}$. Analogously, there were no chemical shift perturbations observable in the overlay of the reference spectrum and the ThT-Aβ(1-42)-spectrum (fig. 4.52). To probe possible perturbations in the aromatic region, a 200 ms mixing time PDSD was recorded (fig. 4.53). Although the SNR was quite low, no chemical shift perturbations could be detected. These data were further supported by an NCα spectrum only showing the excitation of different Cβ resonances, but no deviations in the Cα-region (fig. 4.54).

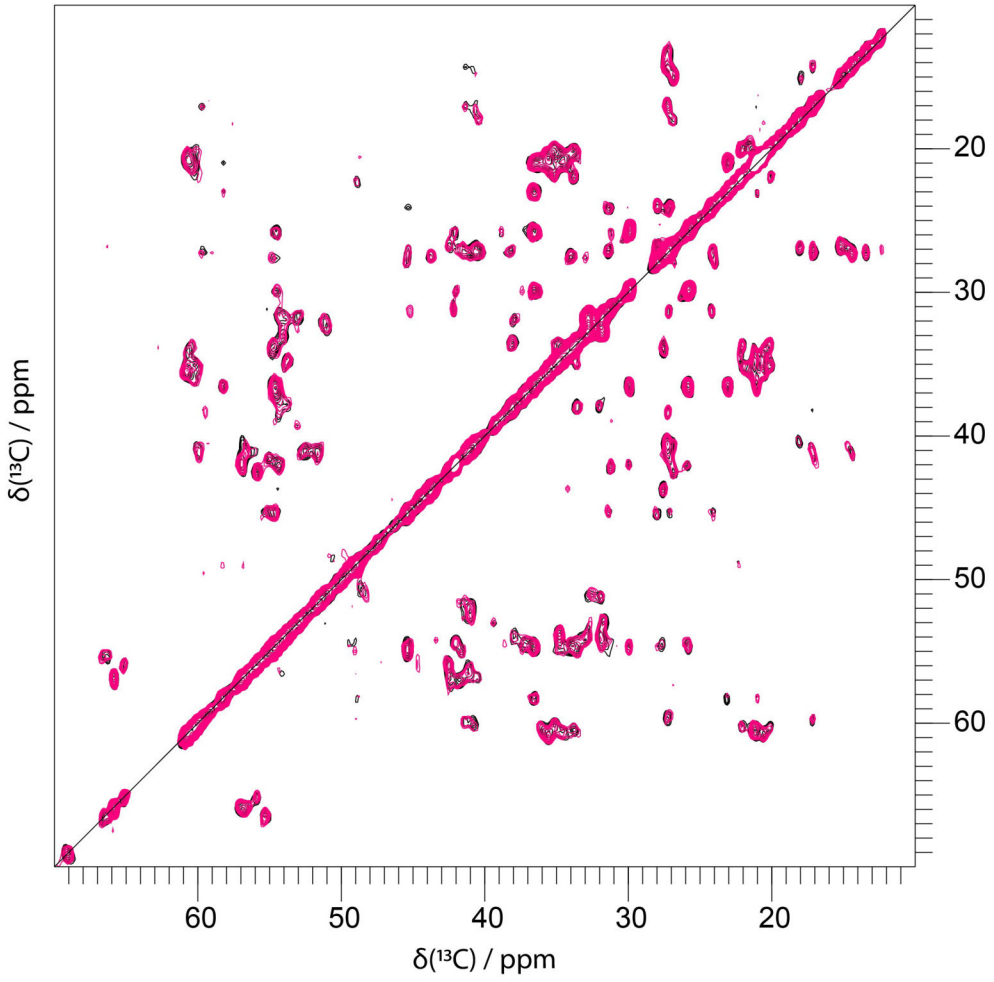

Figure 4.52: Overlay of Proton-Driven Spin Diffusion (PDSD) spectra of fibrillar Aβ(1-42) (pink) and fibrillar Aβ(1-42) with 800 $\mu\frac{mol}{l}$ ThT (black) (CCPN). Both spectra were recorded at a magnetic field strength of 18.8 T corresponding to a proton Larmor frequency of 800 MHz, a spinning speed of 12.5 kHz and a sample temperature of T = 0 ± 5°C. For homonuclear ^{13}C-^{13}C mixing, PDSD with a mixing time of 20 ms was employed. A squared and shifted sine bell function was used for apodization (shift of 0.35π). No chemical-shift perturbations could be found.

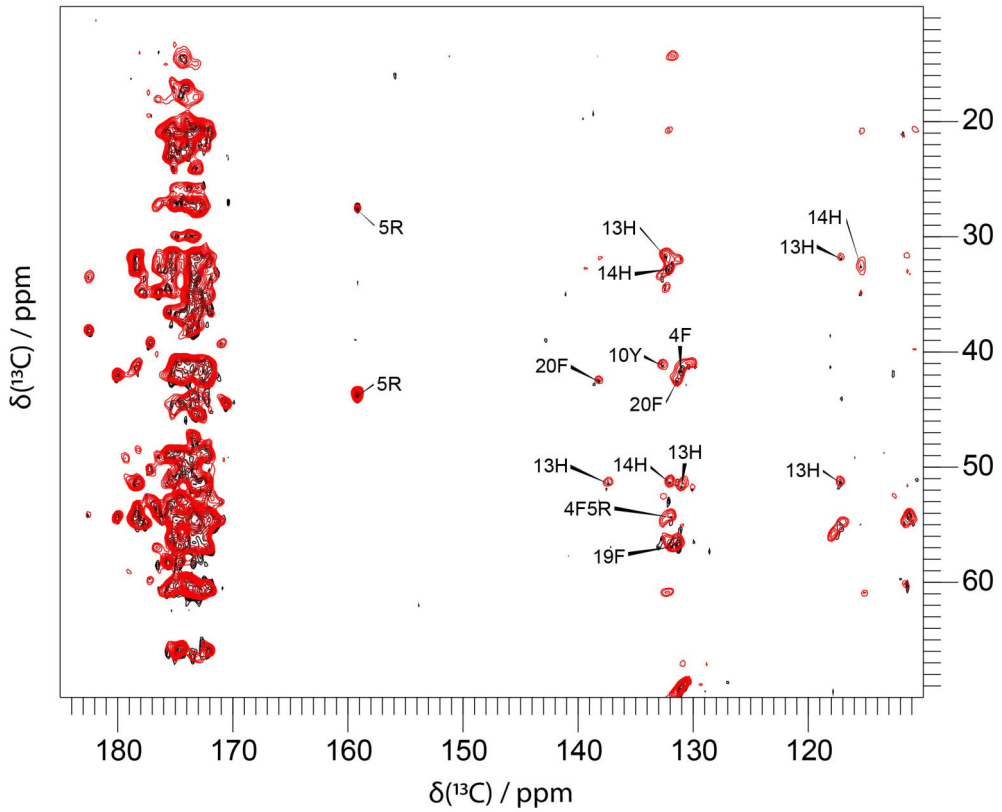

Figure 4.53: Overlay of Proton-Driven Spin Diffusion (PDSD) spectra of fibrillar Aβ(1-42) (red) and fibrillar Aβ(1-42) with 800 $\mu\frac{mol}{l}$ ThT (black) (CCPN). Both spectra were recorded at a magnetic field strength of 18.8 T corresponding to a proton Larmor frequency of 800 MHz, a spinning speed of 12.5 kHz and a sample temperature of T = 0 ± 5°C. For homonuclear ^{13}C-^{13}C mixing, PDSD with a mixing time of 200 ms was employed. A squared and shifted sine bell function was used for apodization (shift of 0.35π). No chemical-shift perturbations could be found. The low SNR in the aromatic region had to be taken into consideration of course.

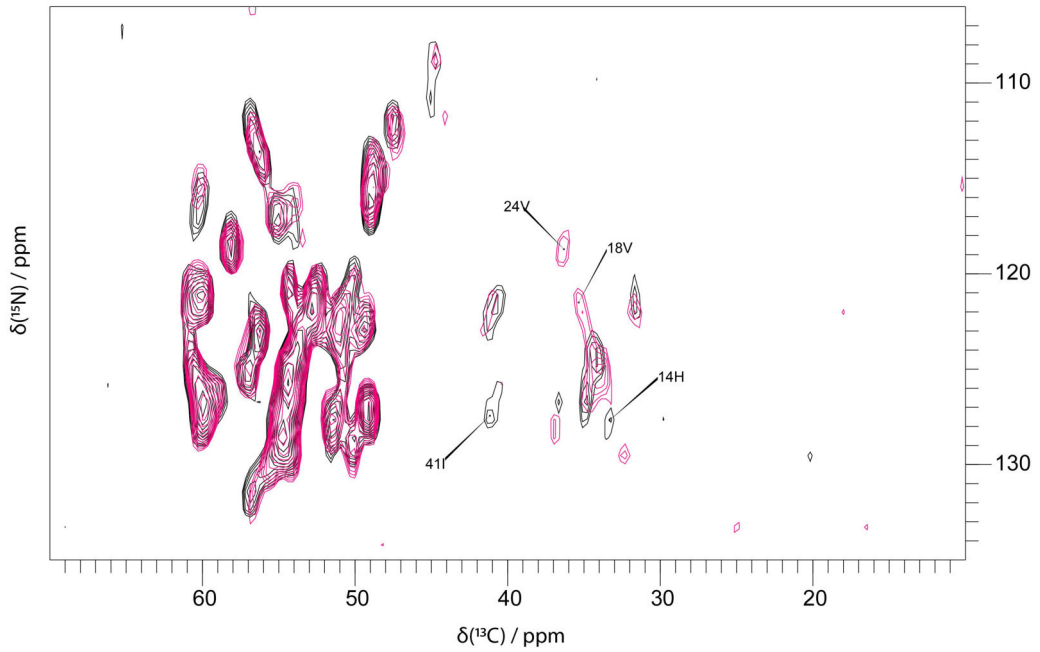

Figure 4.54: Overlay of NCα spectra of fibrillar Aβ(1-42) (pink) and fibrillar Aβ(1-42) with 800 $\mu\frac{mol}{l}$ ThT (black) (CCPN). Both spectra were recorded at a magnetic field strength of 18.8 T corresponding to a proton Larmor frequency of 800 MHz, a spinning speed of 20 kHz and a sample temperature of T = 0 ± 5°C. A squared and shifted sine bell function was used for apodization (shift of 0.35π). No peak shift deviations could be found. Interestingly, different Cβ-resonances were excited in the spectrum of the sample containing ThT, which are assigned with labels.

4.11 pH shift experiments

Intriguingly, molecular dynamics simulations exhibited a detachment of the N-terminus of the Aβ(1-42) fibrils upon shifting the pH to 7 (unpublished results). This would support the finding of flexible residues in the N-terminus of fibrillar Aβ(1-42) in INEPT-type spectra, demonstrated by Colvin et al. [42], while conserving an S-shaped C-terminus. To investigate whether our sample would also change its N-terminal conformation upon a pH shift, homonuclear as well as heteronuclear experiments were carried out.

In the beginning, we probed the structural integrity of the N-terminus with an INEPT 1D spectrum. Remarkably this spectrum remained empty. Afterwards we continued with 2D PDSD spectra, with 20 and 200 ms mixing times, respectively (fig. 4.55-4.58). The SNR was reduced significantly by a lower amount of sample and more buffer liquid in the pH 7 sample, causing an increased demand of scans ($\sim$ 3 times more scans). Moreover, alanine peak intensities were reduced, caused by rotational resonance, except for Ala42, which now adopted a random coil conformation. Since all alanine residues could be completely assigned in PDSD spectra recorded at 600 MHz, this characteristic was related to the static magnetic field, as well as the applied spinning speed. Therefore it would be recommended to repeat these experiments at 600 MHz, too.

From the 20 ms mixing time PDSD, we could conclude an intensity loss for N-terminal residues, but also of middle domain and C-terminal residues as well. Noteworthy these residues were low in intensity in the reference spectra, too. The Cα-Cβ correlation signals of Glu3, His6, His14, Gln15, Lys16, Phe19, Asp23, Met35 and Ile41 were obviously decreased into the noise level in the 20 ms PDSD. The Cα-Cβ correlation of Phe4 was masked by Phe20 and the aromatic side-chains of Phe4 were also not detectable in the 200 ms PDSD, whereas a weak Arg5-Cδ-Cζ correlation occurred. Furthermore Arg5-Cα and Arg5-Cγ correlations gained intensity. Additionally Arg5 resonance signals of Cα, Cγ and Cδ were detectable in the NCαCX spectrum.

Regarding the aliphatic correlation signals of Asp1, Asp1-Cα-Cβ seemed to either vanish or double, however this remained unclear due to the overlapping with Lys28-Cα-Cϵ correlations. Nonetheless, a doubled set of Asp1-Cα-Cγ resonances could be found in the CO-region of the 20 and 200 ms mixing times PDSDs, respectively (fig. 4.56 and 4.58). The new resonance peak of Asp1-Cα-Cγ exhibited significantly higher Cα (+ 2.0 ppm) and Cγ shifts (+ 3.0 ppm), respectively, suggesting a second deprotonated conformer.

Intense correlation signals of Lys28 could be observed, including a splitting along the Cϵ- and Cβ-resonance of Lys28, resulting in two signals, found in the 20 and 200 ms specta, respectively. One of this signal coincided with the Asp1-Cα-Cβ correlation, as previously described in the heteronuclear long-range measurement

chapter (4.4.2). In the case of Asp7, the situation was somehow similar, because of the overlap with Asn27 in the aliphatic region. Similar like for Asp1, we could detect a shifted Asp7-Cα-Cγ correlation in the CO-region of the 20 ms spectrum, which surprisingly vanished in the 200 ms spectrum. Again, Cα and Cγ shifts of Asp7 were shifted 1 ppm towards a higher resonance frequency, pointing to a deprotonated more random-coil like state.
Even though Cα-Cβ of Asp1 and Asp7 signals were not clearly distinguishable in the aliphatic region of the PDSD spectra, the Cα-Cγ and Cβ-Cγ of Asp1 and Asp7 were still detectable in the CO region, respectively.
In perspective of the previously described salt-bridge formed by Asp1, Lys28 and Ala42, findings of doubled resonance signals of Asp1 and Lys28, as well as a free C-terminal end of Ala42, indicated a possibly less-stabilized second N-terminal conformer. Remarkably, residues of the N-terminal kink, namely Ser8 and Tyr10, were detectable, too.
The disappearance of His6 and His14 could be related to the higher pH. Nonetheless, His6 had an enforcing effect on the kink around Tyr10, by forming a salt bridge with Glu11. Combined together, these intensity losses all represented a rather destabilized N-terminal β-strand. Interestingly, His13 still remained detectable in the aliphatic and aromatic region in the 20 ms PDSD spectrum, whereas it vanished in the CO region of the 20 ms spectrum and moreover in the aromatic region of the 200 ms spectrum. Aliphatic peaks of Gln15 were observable in the NCαCX spectrum, although Gln15 resonance peaks vanished completely in the PDSDs.
Bearing in mind the long side-chains of lysine, leucine and isoleucine residues, significant intensity losses could be obtained, attributed to the low SNR and the relatively short mixing time of 20 ms (fig. 4.55 and 4.56). In the case of Leu17 and Leu34, losses occured especially for Cγ and Cδ resonances.
Lys16 resonance signals vanished completely and did not reappear at 200 ms mixing time, however the Leu17-Cγ-Cδ correlations did, as well Leu34-Cγ-Cδ correlations. In addition Lys16 signals were not observed in the NCαCX spectrum, which was expected since they were not observed in the reference NCαCX spectrum either.
Of note was the observation of an intense Phe19-N-Cα correlation in the NCαCX spectrum, which had not been observed before. Interestingly, a second rotamer of Phe20 could not be observed in the pH shifted sample, confirmed by the finding of only one set of resonances of Ala21 in the NCαCX spectrum (fig. 4.59).
A closer look at the resonance signals of glutamic acid at the diagonal suggested chemical shift perturbations of Cβ and Cγ values. Unfortunately, no Glu-Cδ correlations could be obtained in the CO-region of the 20 and 200 ms PDSD spectra, nor in the NCαCX spectrum. Due to the sparse amount of data, a complete assignment of Glu3, Glu11 and Glu22 residues remained elusive and should be achieved in future experiments. However, keeping in mind that both Phe20- and Glu22- side-

chains were solvent-exposed in the initial structure, structural rearrangements of Glu22 might have forced Phe20 to adopt a certain fixed rotameric state.
Contrary to Lys16, Lys28 resonance signals remained highly intense, like in the reference spectra. Remarkably, the resonance signals along the Cϵ chemical shift of Lys28, including Cβ, Cγ and Cδ correlations, all appeared to be split. This could be a hint of two different conformations at the sides of the fibril, destabilizing the N-terminal salt bridges, as previously observed for the shifted carboxyl resonances of Asp1 and Asp7.
Alternatively, these doubled Lys28-Cϵ resonances could also be interresidual correlations between Asn27-Cβ and Lys28 side-chain atoms, which is however less likely, due to the fact that there were no other interresidual cross peaks detectable and the splitting could be observed in the 20 ms PDSD spectrum, too.
With regards to the isoleucine sidechains, Ile31 seemed to be rather unaffected by the pH shift, whereas side-chain correlations of Ile32 and Ile41 remained missing in the 20 ms PDSD spectrum. By increasing the mixing time, side-chain correlations of Ile31 reappeared, as well as Ile41-Cγ1-Cδ.
Finding random coil shifts of Ala42-Cα (+ 4.5 ppm), Ala42-Cβ (- 1.5 ppm) and the deprotonated Ala42-CO signal (+ 3.0 ppm), could be linked again to the degradation of the salt-bridges formed by the N- and C-termini involving Asp1 and Lys28. In the CO-region of the NCαCX spectrum, both chemical shift perturbations of Ala42-CO and Ala42-N could be detected (fig. 4.60). As a result of the free N-terminal Ala42, Asp1 would not be enabled to form a salt bridge with Lys28, which in turn further destabilizes the N-terminal β-strand. Moreover, Ile41-N and Ile41-Cγ2 were shifted towards higher values [+ 2,5 ppm (^{15}N) and + 0.5 ppm (^{13}C)], impacted by a free C-terminus. In conclusion, this backed up the suggestion of a possible second conformer of the N- and C-terminal interface region.
In conclusion, we suggested the finding of an additional less attached N-terminal segment, being present as a second conformer. We could provide evidence to support this conclusion, by the observation of resonance doublings of Asp1 and Lys28, as well as the finding of random-coil like and deprotonated shifts of Asp1, Asp7 and Ala42. To provide further proof on this finding, 3D, long-range correlation experiments and cryoEM measurements would be helpful, to compare these new results to our previous findings.

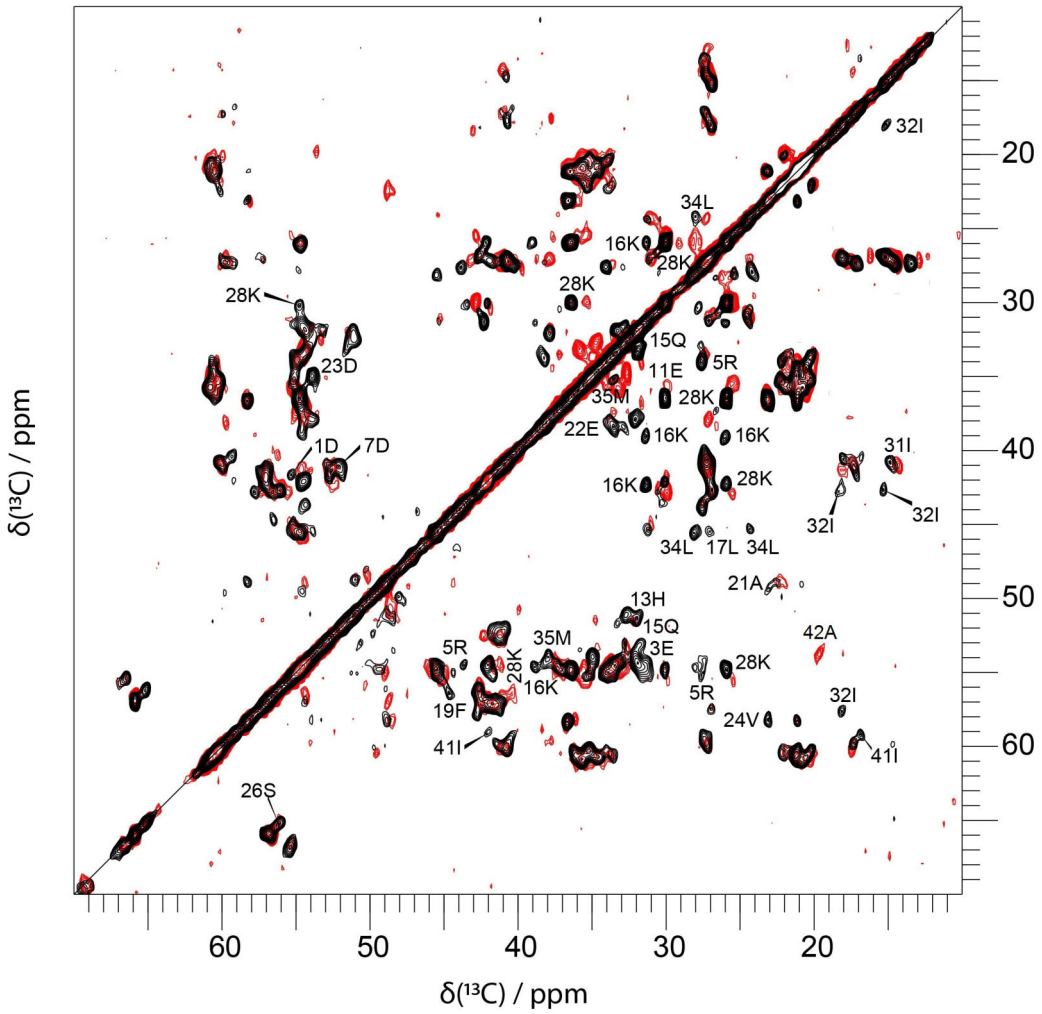

Figure 4.55: Overlay of Proton-Driven Spin Diffusion (PDSD) spectra of fibrillar Aβ(1-42) at pH 2 (black) and fibrillar Aβ(1-42) at pH 7 (red) (CCPN). Both spectra were recorded at a magnetic field strength of 18.8 T corresponding to a proton Larmor frequency of 800 MHz, a spinning speed of 12.5 kHz and a sample temperature of T = 0 ± 5°C. For homonuclear ^{13}C-^{13}C mixing, PDSD with a mixing time of 20 ms was employed. A squared and shifted sine bell function was used for apodization (shift of 0.28π for the black spectrum and 0.35π for the red spectrum). In the red spectrum the SNR was much lower (288 scans red spectrum, 80 scans black spectrum). Assigned residues displayed chemical shift perturbations resulting from the pH shift, vanished or were of interest for the stability of the N-terminus. Especially residues in the N-terminus clearly lost intensity (Asp1, Glu3, Arg5, His6, His14, Gln15). Moreover, residues in the middle domain and the C-terminus also experienced intensity losses (Lys16, Leu17, Phe19, Asp23, Val24, Ile32, Met35, Ile41). Interestingly Ala42-Cα-Cβ adopted a random coil conformation after the pH shift, deducible by a higher Cα and conversely lower Cβ-shift. Lastly a peak splitting of Lys28-Cδ-Cϵ and Lys28-Cγ-Cβ was observed.

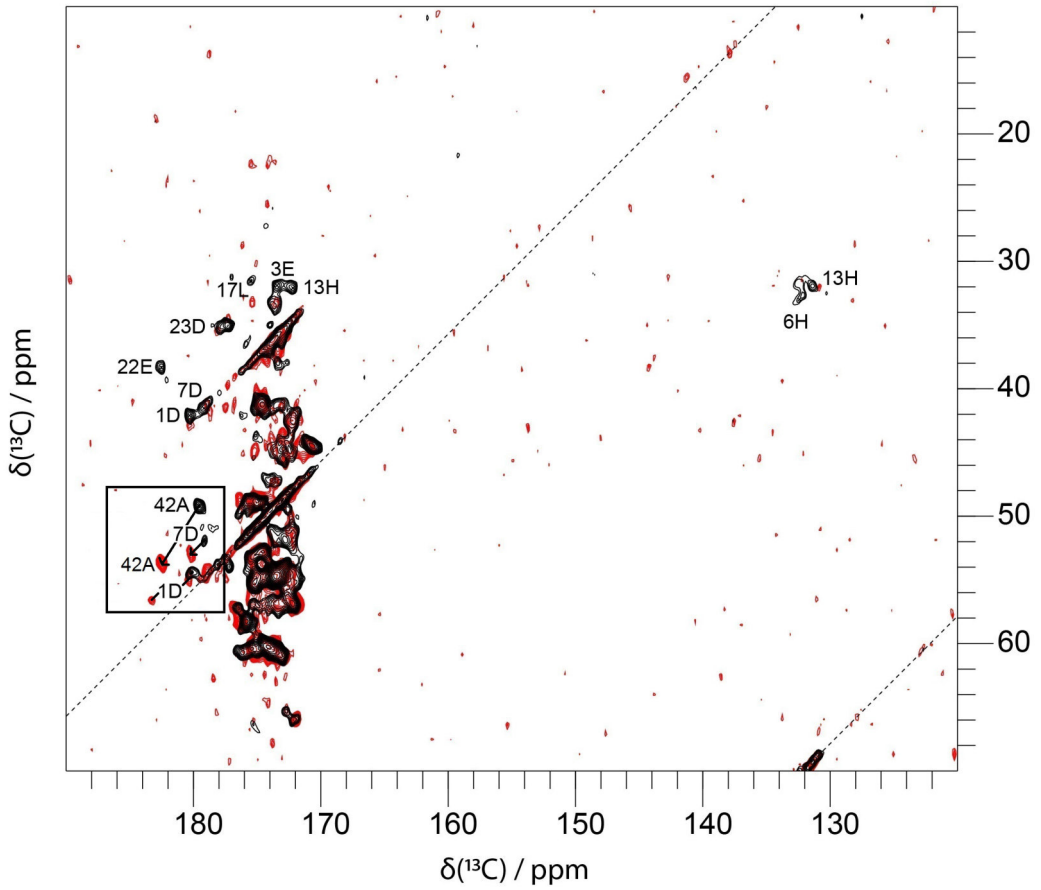

Figure 4.56: Overlay of the aromatic and carboxyl regions of Proton-Driven Spin Diffusion (PDSD) spectra of fibrillar Aβ(1-42) at pH 2 (black) and fibrillar Aβ(1-42) at pH 7 (red) (CCPN). Both spectra were recorded at a magnetic field strength of 18.8 T corresponding to a proton Larmor frequency of 800 MHz, a spinning speed of 12.5 kHz and a sample temperature of T = 0 ± 5°C. For homonuclear ^{13}C-^{13}C mixing, PDSD with a mixing time of 20 ms was employed. A squared and shifted sine bell function was used for apodization (shift of 0.28π for the black spectrum and 0.35π for the red spectrum, respectively). In the red spectrum the SNR was much lower (288 scans red spectrum, 80 scans black spectrum). Assigned residues displayed chemical shift perturbations resulting from the pH shift, vanished or were of interest for the stability of the N-terminus. In the aromatic region His13 is still detectable, whereas the peak in the CO region vanished. Several other peaks in the CO region vanished similarly, like Glu3, His13, Leu17 and Glu22. Remarkably, Asp1-Cα- and Cγ-shifts were shifted by + 2 ppm and + 3ppm, respectively, as well as Asp7-Cα- and Cγ-shifts were shifted by + 1 ppm. Surprisingly, Ala42-Cα- and CO-shifts were even shifted by + 4.5 ppm and + 3.0 ppm, respectively. All these chemical shift perturbations indicated a higher degree of random-coil structure and deprotonation of carboxyl groups (black box).

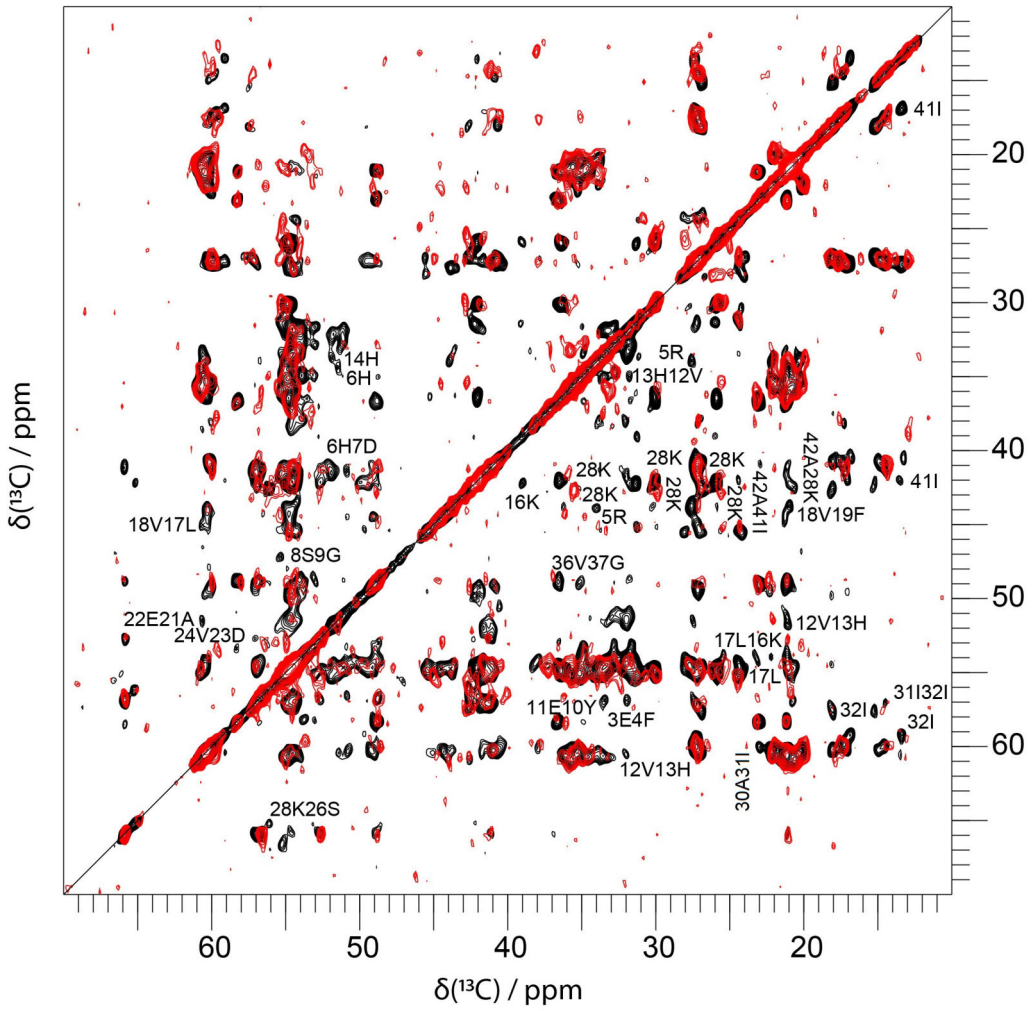

Figure 4.57: Overlay of the aliphatic regions of Proton-Driven Spin Diffusion (PDSD) spectra of fibrillar Aβ(1-42) at pH 2 (black) and fibrillar Aβ(1-42) at pH 7 (red) (CCPN). Both spectra were recorded at a magnetic field strength of 18.8 T corresponding to a proton Larmor frequency of 800 MHz, a spinning speed of 12.5 kHz and a sample temperature of T = 0 ± 5°C. For homonuclear ^{13}C-^{13}C mixing, PDSD with a mixing time of 200 ms was employed. A squared and shifted sine bell function was used for apodization (shift of 0.28π for the black spectrum and 0.35π for the red spectrum, respectively). In the red spectrum the SNR was much lower (248 scans red spectrum, 160 scans black spectrum). Assigned residues displayed chemical shift perturbations resulting from the pH shift, vanished or were of interest for the stability of the N-terminus. Due to the worse SNR several interresidual signals dropped below the noise level. Moreover even intraresidual peaks were not detectable anymore, like Arg5-Cβ-Cγ, which was observable in the 20 ms PDSD spectrum. However also resonance signals that had not been observed in the 20 ms PDSD spectrum, like Lys16, Leu17, Ile32 and Ile41 did not appear. Finally peak splittings along the Lys28-Cϵ chemical shift could be observed, indicating two possible side-chain conformers.

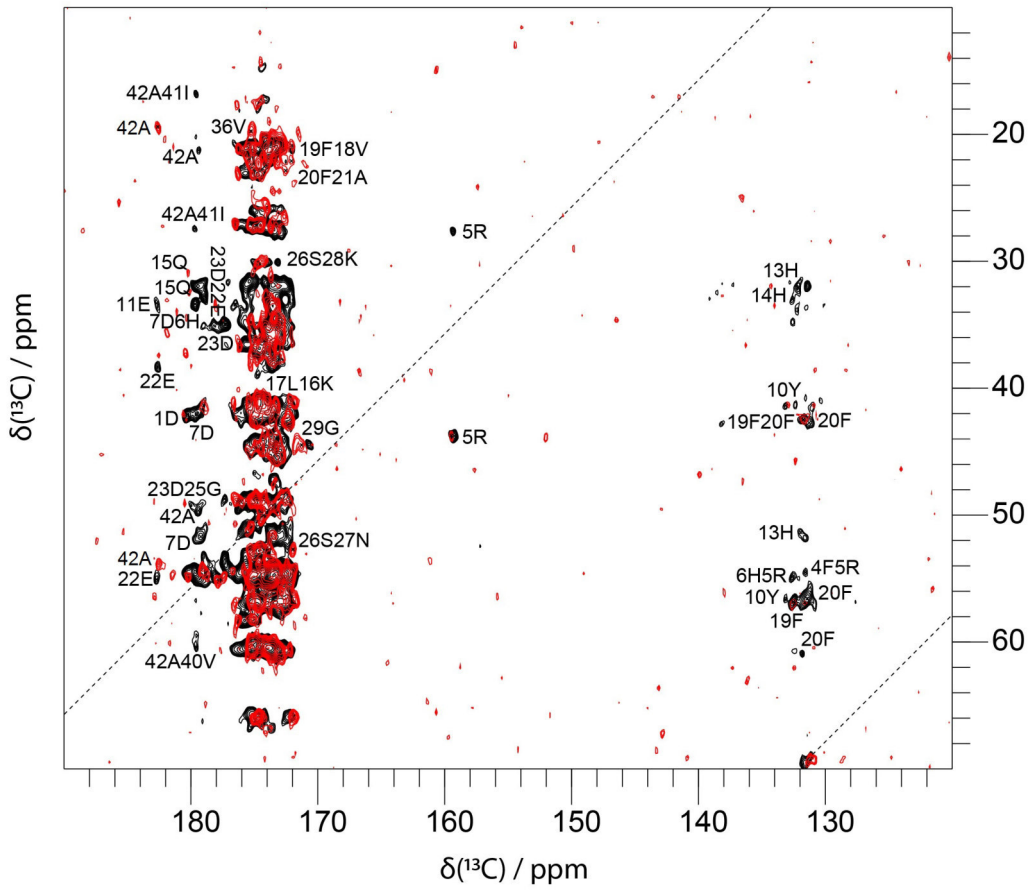

Figure 4.58: Overlay of the aromatic and carboxyl regions of Proton-Driven Spin Diffusion (PDSD) spectra of fibrillar Aβ(1-42) at pH 2 (black) and fibrillar Aβ(1-42) at pH 7 (red) (CCPN). Both spectra were recorded at a magnetic field strength of 18.8 T corresponding to a proton Larmor frequency of 800 MHz, a spinning speed of 12.5 kHz and a sample temperature of T = 0 ± 5°C. For homonuclear ^{13}C-^{13}C mixing, PDSD with a mixing time of 200 ms was employed. A squared and shifted sine bell function was used for apodization (shift of 0.28π for the black spectrum and 0.35π for the red spectrum, respectively). In the red spectrum the SNR was much lower (248 scans red spectrum, 160 scans black spectrum). Assigned residues displayed chemical shift perturbations resulting from the pH shift, vanished or were of interest for the stability of the N-terminus. Due to the worse SNR several interresidual signals dropped below the noise level. Moreover even intraresidual peaks were not detectable anymore, like aromatic resonance signals of histidines and phenylalanines. Nonetheless, only peaks of His13, Phe19 and Phe20 were expected to appear in the aromatic region. An Arg5-Cδ-Cζ correlation could be observed, indicating the conserved rigidity of this salt-bridge forming residue. The Ala42-Cα-CO resonance signal observed in the 20 ms spectrum remained in the same position, whereas the Asn27-Cα-Cγ signal vanished. Additionally an Ala42-Cβ-CO resonance signal appeared.

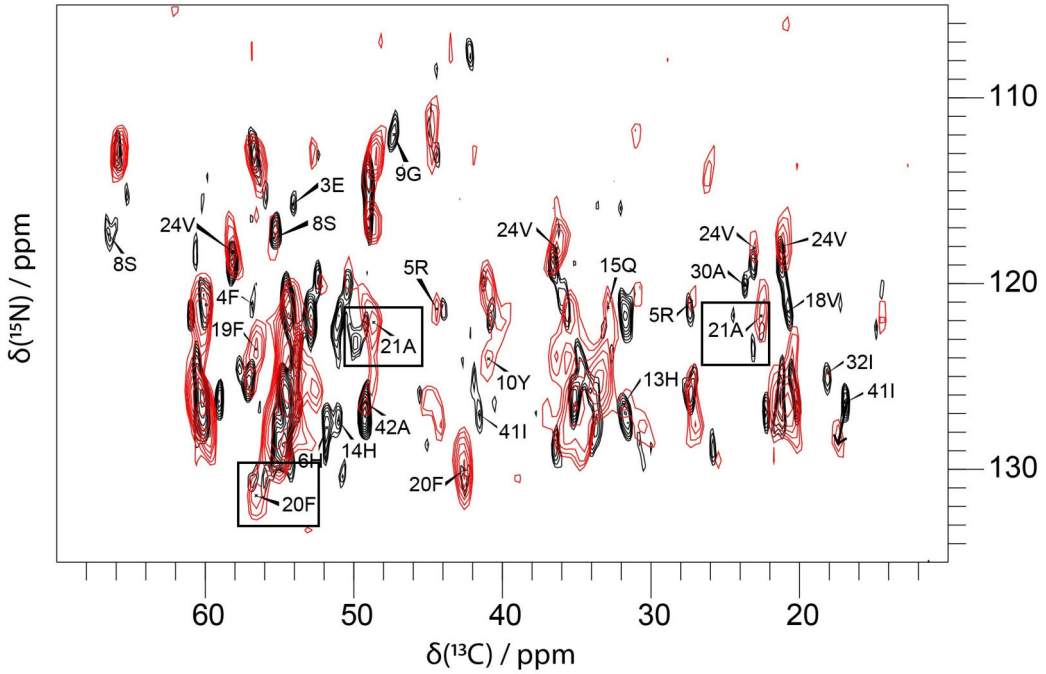

Figure 4.59: Overlay of the aliphatic regions of NCαCX spectra of fibrillar Aβ(1-42) at pH 2 (black) and pH 7 (red) (CCPN). Both spectra were recorded at a magnetic field strength of 18.8 T corresponding to a proton Larmor frequency of 800 MHz and a sample temperature of T = 0 ± 5°C. The applied spinning speed in the black spectrum was 18 kHz and in the red spectrum 12.5 kHz, respectively. A squared and shifted sine bell function was used for apodization (shifts of 0.28π for the black and 0.35π for the red spectrum, respectively). In the red spectrum the SNR was lower (3584 scans red spectrum, 6656 scans black spectrum). Assigned residues displayed chemical shift perturbations resulting from the pH shift, vanished or were of interest for the stability of the N-terminus. Remarkably, no peak doublings of Phe20-N-Cα, Ala21-N-Cα and Ala21-N-Cβ could be detected, marked with boxes. Due to the relatively low SNR Glu3-N-Cα and Phe4-N-Cα vanished into the noise, whereas Arg5-N-Cγ/Cδ, Ser8-N-Cα and Tyr10-N-Cβ were still detectable. Moreover Ile32-N-Cγ2 and Ile41-N-Cβ signals disappeared. However, Ile41-N-Cγ2 was shifted towards higher values [+ 2,5 ppm (^{15}N) and + 0.5 ppm (^{13}C)]. A His13-N-Cβ correlation was still detectable. Interestingly, a strong Phe19-N-Cα correlation appeared.

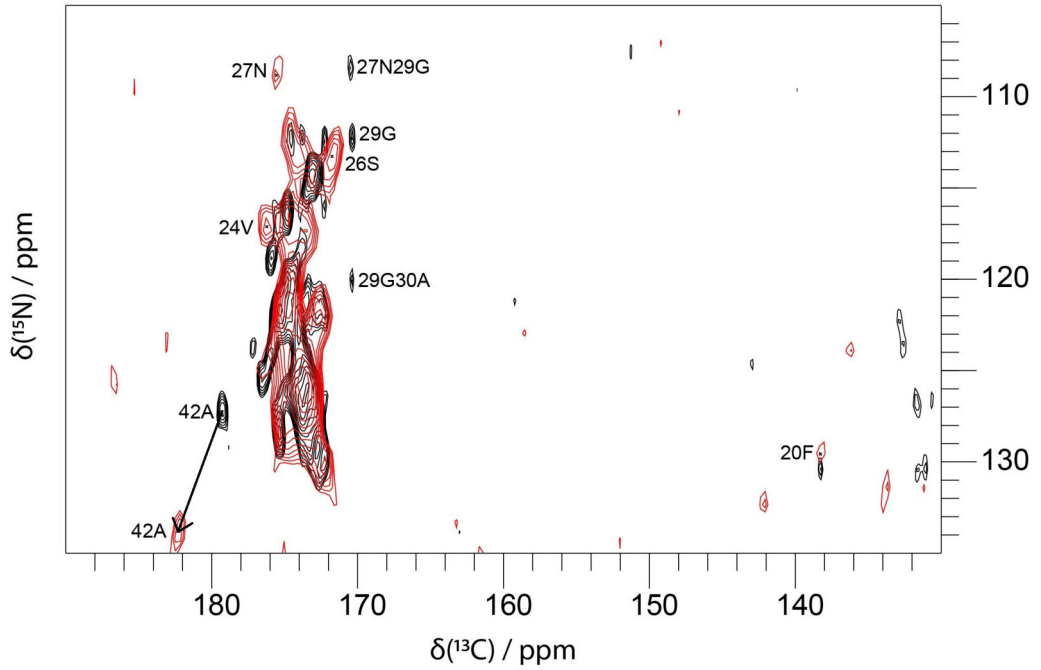

Figure 4.60: Overlay of the aromatic and carboxyl regions of NCαCX spectra of fibrillar Aβ(1-42) at pH 2 (black) and pH 7 (red) (CCPN). Both spectra were recorded at a magnetic field strength of 18.8 T corresponding to a proton Larmor frequency of 800 MHz and a sample temperature of T = 0 ± 5°C. The applied spinning speed in the black spectrum was 18 kHz and in the red spectrum 12.5 kHz, respectively. A squared and shifted sine bell function was used for apodization (shifts of 0.28π for the black and 0.35π for the red spectrum, respectively). In the red spectrum the SNR was lower (3584 scans red spectrum, 6656 scans black spectrum). Assigned residues displayed chemical shift perturbations resulting from the pH shift, vanished or were of interest for the stability of the N-terminus. Interresidual contacts of Gly29 and moreover intraresidual contacts of the latter, as well as Ala42 vanished. A very low intense aromatic side-chain correlation of Phe20-N-Cγ could be observed. Interestingly, the newly observed Ala42-N-CO signal in red could be easily distinguished from the old one in black, because of the high CO and N shift.

5 Conclusion

In conclusion, we could determine the structure of our Aβ(1–42) fibril polymorph with cryoEM and ssNMR with consistent results. The well-resolved peaks allowed the assignment of all 42 amino acids of the peptide, as well as their chemical shift analysis towards protonation states. In addition, long-range contacts backed the structure based on the cryoEM data, underlining the benefit of this powerful combined approach. The published de-novo structure showed interesting features: a rigid N-terminus, kinks at positions 10 and 23 forming an L-shape and a staggered arrangement of the monomers wihtin the protofibrils.

The attachment of the N-terminus to the fibril core was stabilized by a hydrophobic cluster, which might be further stabilised and more pathogenic in a familiar inherited form of AD (A2V mutation) [152]. For rats and mice, which do not develop AD, attributed to three mutations (R5G, Y10F and H13R), the kink formation around residue 10 might be hindered. Additionally, the so-called arctic mutation (E22G) involved in early onset dementia, could support the kink around position 23 by reducing charge repulsion [153].

Contrary to the study of Lopez del Amo et al., our DNP measurements could not reproduce the observation of maintaining a similar resolution upon freezing our sample from room temperature to 100 K. However, we could confirm an enhancement of resolution by increasing the static magnetic field. The investigation of which sample preparation method was more suitable for the fibril sample yielded the rather surprising result that a glycerol-containing sample with a lower AMUPol concentration led to a higher enhancement factor.

Moreover, we started to investigate the dynamics of the fibril with T_ρ^1 experiments, further supporting our finding of a rigid N-terminus, yet not as rigid as the middle and C-terminal domain of the fibril.

The surface experiments suggested a highly ordered salt-bridge on the side of the interface region, facilitating the transfer of magnetization from the surrounding and coordinated water molecules and are continued.

Binding studies of ThT and Aβ(1-42) could be investigated on a nuclear length scale, however there are still open questions regarding macroscopic changes of the fibril geometry, which have to be addressed.

Likewise, our understanding of the pH shift indicates a structural change regarding the N-terminus and the interface region, however these experiments are still

work in progress.
On the whole, the understanding of pathogenic familial mutations in AD, the investigation of fibril rigidity and the development of kinetic models for fibril growth will profit from the presented results.

6 Publications

6.1 Fibril structure of amyloid-β(1–42) by cryo–electron microscopy

Lothar Gremer, Daniel Schölzel, Carla Schenk, Elke Reinartz, Jörg Labahn, Raimond B. G. Ravelli, Markus Tusche, Carmen Lopez-Iglesias, Wolfgang Hoyer, Henrike Heise, Dieter Willbold and Gunnar F. Schröder

Published in: Science, 358:116-119, 2017.

Impact Factor: 14.142 (SJR)

Contribution: 8.3 %

Involved in the conception and application of the solid state NMR experiments, as well as reporting a detailed description of the latter in the materials and methods part of the paper.

6.2 Origin of Metastable Oligomers and their Effects on Amyloid Fibril Self-Assembly

Filip Hasecke, Tatiana Miti, Carlos Perez, Daniel Schölzel, Lothar Gremer, Clara S. R. Grüning, Garrett Matthews, Georg Meisl, Tuomas P. J. Knowles, Dieter Willbold, Philipp Neudecker, Henrike Heise, Ghanim Ullah, Wolfgang Hoyer and Martin Muschol

Published in: Chemical Science, 9(27):5937-5948, 2018.

Impact Factor: 9.063 (rsc.org)

Contribution: 6.7 %

Involved in the solid state NMR measurements and the analysis of the results.

6.3 Hyperpolarized MAS NMR of Unfolded and Misfolded Proteins

Anna König, Daniel Schölzel, Boran Uluca, Thibault Viennet, Ümit Akbey and Henrike Heise

Published in: Solid State Nuclear Magnetic Resonance, 98:1-11, 2019.

Impact Factor: 2.674 (elsevier.com)

Contribution: 17 %

Wrote parts of the subsection "DNP-enhanced MAS NMR of amyloid fibrils".

6.4 Isotopically enriched systems (Chapter 10)

Claudia Beumer, Anna König, Daniel Schölzel, Boran Uluca, Franziska Weirich and Henrike Heise

Publisher: Royal Society of Chemistry

Book title: Modern methods in solid-state NMR: a practitioner's guide

Editor: Paul Hodgkinson

Type: Book Chapter (pages 289-321)

Contribution: 17 %

Wrote two subsections of the section "Dipolar Recoupling Techniques for Multi-dimensional NMR Spectroscopy".

7

Supplement

On the following pages, experimental details, fitting parameters, the complete chemical shift assignment and applied pulse program codes can be found.

Supplement Table 1: Experimental Details of NMR Experiments published in L. Gremer et al. [94].

Sample: uniformly 13C & 15N labelled and recombinantly expressed Aβ1-42									
	HN CP	PDSD	SPC5_2	NCACX DARR	NCACB DREAM	NCOCX DARR	NCOCX DARR	NcoCACB BSH CP DREAM	NcoCACB BSH CP DREAM
	1D	2D	2D	2D	2D	2D	3D	2D	3D
Mixing time		1) 20 ms 2) 50 ms 3) 200 ms		55 ms		1) 100 ms 2) 107.5 ms	80 ms		
^{1}H frequency (MHz)	800	1) & 3) 800 2) 600	600	800	800	1) 600 2) 800	800	800	800
MAS (kHz)	18.00	1) & 3) 12.50 2) 11.00	8.00	18.00	21.50	1) 14.00 2) 18.00	18.00	21.50	21.50
VT gas temperature (°C)	-10	-10	-10	-10	-10	-10	-10	-10	-10
Transfer 1	HN CP	HC CP	HC CP	HN CP	HN CP	HN CP	HN CP	HN CP	HN CP
Carrier (ppm)	114.62	1) & 3) 73.14 2) 90.05	70.53	119.99	119.91	1) 119.97 2) 119.91	119.91	119.91	119.91
Duration of 1st transfer (µs)	500	1) & 3) 500 2) 300	300	500	660	1) 400 2) 780	660	760	660
Transfer 2			SPC5	N-CA CP	N-CA CP	N-CO CP	N-CO CP	N-CO CP	N-CO CP
Carrier (ppm)			Ca: 53.860 CO: 117.19	54.16	55.70	1) 174.42 2) 175.03	175.03	175.03	175.70
duration of 2nd transfer (µs)				2000	2600	1) 1400 2) 1325	1100	2600	2600
^{13}C rf field (kHz)				4.71	7.45	1) 4.46 2) 3.42	7.24	7.66	7.55
^{15}N rf field (kHz)				11.41	11.76	1) 9.68 2) 12.93	9.27	11.96	12.21
Transfer 3					DREAM			BSH CP	BSH CP
Carrier (ppm)					55.70			56.03	60.60
duration of 3rd transfer (µs)					1875			3800	3750
^{13}C rf field (kHz)								13.97	14.69
Transfer 4								DREAM	DREAM
Carrier (ppm)								56.43	57.5
duration of 4th transfer (µs)								1800	1850
t1 increments	182	1) & 3) 1250 2) 454	908	1250	714	1) 1072 2) 1406	882	882	714
t1 spectral width (kHz)	18.116	1) & 3) 104.167 2) 37.879	37.878	104.167	59.524	1) 89.286 2) 78.125	73.529	73.529	59.524
t2 increments		1) & 3) 240 2) 198	240	22	20	1) 20 2) 22	12	20	12
t2 spectral width (kHz)		1) & 3) 40.225 2) 33.281	40.080	2.999	3.200	1) 3.600 2) 3.000	2.400	3.200	2.400
t3 increments							20		15
t3 spectral width (kHz)							5.000		5.000
Number of scans		1) 80, 3) 160 2) 192	Ca: 224 CO: 256	6656	800	1) 4672 2) 7840	544	5376	1376
Duration	1.75 h	1) 21.75 h 2) 43.7 h 3) 47.25 h	Ca: 43.5 h CO: 69.5 h	168.6 h	18 h	1) 43.6 h 2) 110 h	304.5 h	121 h	557.5 h

Supplement Table 2: Chemical Shifts for Aβ(1-42) fibrils

		N	C′	Cα	Cβ	Cγ	Cδ	Cε	Cξ	Nδ1	Nδ2	Nε1	Nε2	Nξ	NH1	NH2
1	D		172.0	55.0	41.9	180.1										
2	A	121.9	175.6	51.0	32.0											
3	E	116.1	173.6	54.4	32.0	33.7										
4	F	121.5	172.5	56.6	42.3	137.9	131.6									
5	R	121.2	173.6	54.6	33.9	27.5	43.9		159.3			84.6			72.7	70.5
6	H	127.3	173.8	51.4	33.3	132.5				182.8			176.3			
7	D	121.5	173.2	52.0	41.2	179.3										
8	S	117.0	175.0	55.3	66.3											
9	G	111.8	174.0	47.3												
10	Y	124.8	173.8	56.8	41.6		133.0	118.4	157.0							
11	E	125.5	173.7	54.6	33.4	35.0	182.6									
12	V	124.5	174.1	60.4	34.8	21.1, 20.1										
13	H	126.7	172.8	51.4	31.9	131.8	117.3	137.7		182.8			176.3			
14	H	127.3	174.1	51.2	32.7	132.7	115.1			182.8			176.3			
15	Q	121.6	173.9	53.1	31.9	33.1	179.2									
16	K	123.8	173.3	54.5	39.0	26.0	31.5	42.4						33.8		
17	L	128.6	175.1	54.9	45.0	31.4	27.2, 24.4									
18	V	121.5	176.4	60.6	35.4	21.0, 22.2										
19	F	122.2	172.6	56.6	44.2	137.6	131.5, 132.9									
20	F	130.2	172.5	56.3	42.5	138.1	131.3									
20'	F	130.2	172.5	56.0	42.5	138.1	131.3									
21	A	122.5	174.9	49.2	22.3											
21'	A	123.5	176.3	49.6	23.1											
22	E	121.3	173.5	54.5	33.5	38.1	182.7									
23	D	126.7	174.1	53.9	35.1	177.0										
24	V	118.8	175.8	58.1	36.7	21.1, 23.1										
25	G	116.3	174.6	49.0												
26	S		172.4	56.6	65.9											
26'	S	115.1	172.7	56.1	65.4											
27	N	119.7	175.6	52.4	41.4	178.1					109.6					
28	K	128.6	175.5	54.9	36.4	26.1	30.1	42.1						33.8		
29	G	111.6	170.5	44.7												
30	A	120.6	173.8	49.8	23.6											
31	I	121.5	174.6	60.1	40.8	27.3, 17.5	14.7									
32	I	125.0	176.0	57.5	42.7	27.0, 18.1	15.2									
33	G	113.7		44.8												
34	L	126.0	173.5	54.5	45.4	27.9	25.4, 24.3									
35	M	126.5	173.5	54.3	37.9	32.1		17.3								
36	V	126.3	175.5	60.2	35.2	20.6, 21.2										
37	G	114.6	173.1	49.0												
38	G	116.0	173.2	48.9												
39	V	125.4	173.4	60.4	33.9	21.4, 20.8										
40	V	126.8	174.0	60.4	35.2	21.7, 20.5										
41	I	126.3	175.7	59.1	41.8	27.4, 17.2	13.4									
42	A	126.8	179.4	49.3	21.2											

Supplement Table 3: Experimental Details of NMR Experiments presented in this thesis.

Sample: uniformly 13C & 15N labelled and recombinantly expressed Aβ1-42									
	HC CP	PDSD	SPC5_2	Water-PDSD	Water-SPC5_2	T_1^{ρ}-PDSD	T_1^{ρ}-SPC5_2	NCA	PAIN
	1D	2D	2D	2D	2D	2D	2D	2D	2D
Mixing time (ms)		20		50		50			
^{1}H frequency (MHz)	1) 800 (DNP) 2) 600 (DNP)	1) 800 (RT_B) 2) 800 (RT_V) 3) 800 (DNP) 4) 600 (DNP)	1) 800 (DNP) 2) 600 (DNP)	600	600	600	600	800	600
MAS (kHz)	1) 11.00 2) 8.00	1) & 2) 12.50 3) 11.00 4) 8.00	8.00	11.00	8.00	15.00	8.00	1) 18.00 2) 20.00	15.00
VT gas temperature (°C)	-170	-10 -170	-170	-10	-10	-10	-10	-10	-10
Transfer 1	HC CP	HC CP	HC CP	HC CP	HC CP	HC CP	HC CP	HN CP	HN CP
Carrier (ppm)	1) 55.39 2) 83.00	1) & 2) 73.00 3) 55.39 4) 100.00	1) 90.00 2) 83.00	99.81	39.98	108.96	99.81	1) 119.91 2) 117.34	1) 33.25 2) 33.36 3) 110.21
Duration of 1st transfer (µs)	150	1) 1000 2) 500 3) & 4) 150	1) 200 2) 150	450	660	200	350	1) 560 2) 1500	1) 900 2) 700 3) 400
Transfer 2			SPC5		SPC5		SPC5	N-CA CP	PAIN CP
Carrier (ppm)			1) 90.00 2) 83.00		39.98		99.81	1) 54.16 2) 55.00	1) 174.94 2) 42.44 3) 21.39
duration of 2nd transfer (ms)								1) 1.2 2) 2.6	15
^{13}C rf field (kHz)								1) 4.66 2) 51.13	1) 22.35 2) 23.04 3) 22.52
^{15}N rf field (kHz)								1) 11.16 2) 39.02	1) 26.87 2) 24.67 3) 26.4
T_1^{ρ} / proton mixing time (ms)				3.25, 6.5, 10	3, 4, 5, 6	0, 2.5, 5, 10	0, 4, 8		
Spin lock field (kHz)						37.5	36		
t1 increments	1) 1280 2) 1024	1) 1792 2) 2500 3) 1280 4) 1024	1) 768 2) 1024	572	760	714	572	1) 1428 2) 1024	1) 544 2) 520 3) 544
t1 spectral width (kHz)	1) 59.52 2) 45.45	1) 52.08 2) 104.17 3) 59.52 4) 45.45	1) 52.08 2) 45.45	35.71	54.35	44.64	35.71	1) 59.52 2) 64.1	1) 54.4 2) 52.1 3) 54.4
t2 increments		1) & 2) 480 3) 260 4) 140	1) 170 2) 120	396	80	632	480	1) 100 2) 56	1) & 2) 30 3) 26
t2 spectral width (kHz)		1) 40.32 2) 40.22 3) 44.25 4) 33.11	1) 68.49 2) 49.02	33	16.00	45	40	1) 5.02 2) 4.87	1) & 2) 3.05 3) 2.7
Number of scans	1) 128 2) 32/128/ 512	1) 80 2) 80 3) 144 4) 144	1) 208 2) 80	192	3840	160	240	1) 256 2) 736	1) 9008 2) 10112 3) 12912
Duration (h)	1) 0.1 2) 0.04/0.1/ 0.6	1) 22/32.8 2) 21.7 3) 62.5/43.5 4) 22.5	1) 95.3 2) 13.5	43.5	172	58	64.3	1) 14.25 2) 23.3	1) 183.3 2) 170.5 3) 188.6

Supplement Table 4.1: Experimental Details of peak integration boxes used for 13C-T_ρ^1-PDSD measurements.

Sample: uniformly 13C & 15N labelled and recombinantly expressed Aβ1-42				
residue	**Y1**	**Y2**	**X1**	**X2**
Ala2 (CαCβ)	50.45	51.45	23.75	24.75
Arg5 (CαCδ)	53.8	54.8	43.2	44.2
Arg5 (CαCγ)	53.8	54.8	27	28
Arg5 (CδCγ)	43.3	44.3	27	28
Ser8 (CαCβ)	54.2	55.2	65.9	66.9
Ser8 (CβCO)	65.9	66.9	174.4	175.4
Ala21 (CαCβ)	48.7	49.7	21.75	22.75
Glu22 (CγCδ)	37.9	38.9	182	183
Asp23 (CβCγ)	34.5	35.5	177.1	178.1
Val24 (CαCβ)	57.5	58.5	36	37
Val24 (CαCγ)	57.5	58.5	22.4	23.4
Val24 (CβCγ)	35.9	36.9	22.4	23.4
Ser26 (CαCβ)	55.9	56.9	65.2	66.2
Ser26 (CβCO)	65.2	66.2	171.8	172.8
Lys28 (CγCδ)	29.4	30.4	25.3	26.3
Lys28 (CβCγ)	35.9	36.9	25.3	26.3
Lys28 (CβCδ)	35.9	36.9	29.5	30.5
Gly29 (CαCO)	44	45	169.9	170.9
Ile31 (CβCγ1)	41.2	42.2	27	28
Ile31 (CβCδ)	41.2	42.2	14	15
Ile31 (CαCβ)	59.1	60.1	40.2	41.2
Ile32 (CαCγ2)	56.6	57.6	17.5	18.5
Ile32 (CαCγ1)	56.6	57.6	26.4	27.4
Ala42 (CαCβ)	48.6	49.6	20.15	21.15
Ala42 (CαCO)	48.8	49.8	178.8	179.8

Supplement Table 4.2: Experimental Details of peak integration boxes used for 13C-T_ρ^1-SPC5 measurements.

Sample: uniformly 13C & 15N labelled and recombinantly expressed Aβ1-42				
residue	**Y1**	**Y2**	**X1**	**X2**
Ala21 (Cα+Cβ, Cα)	70	71	48.4	49.4
Val24 (Cα+Cγ, Cγ)	58.8	59.8	22.3	23.3
Ser26 (Cα+Cβ, Cβ)	121.5	122.5	65.2	66.2
Lys28 (Cγ+Cδ, Cδ)	55.3	56.3	29.3	30.3

Supplement Table 4.3: Fitting parameters used for 13C-T_ρ^1-PDSD fitting curves.

Sample: uniformly 13C & 15N labelled and recombinantly expressed Aβ1-42			
residue	**fp / ms**	**A**	**R^2_{adj} / %**
Ala2 (CαCβ)	8.8	99.6	91
Arg5 (CαCδ)	13.0	99.6	85
Arg5 (CαCγ)	7.6	99.2	96
Arg5 (CδCγ)	7.4	71.0	26
Ser8 (CαCβ)	4.9	72.1	30
Ala21 (CαCβ)	7.0	100.4	91
Glu22 (CγCδ)	3.7	90.2	90
Asp23 (CβCγ)	7.5	86.3	77
Val24 (CαCβ)	18.1	101.4	97
Val24 (CαCγ)	14.3	95.0	80
Val24 (CβCγ)	10.2	100.1	72
Ser26 (CαCβ)	8.0	92.9	91
Ser26 (CβCO)	11.3	97.2	98
Lys28 (CγCδ)	8.7	95.7	90
Lys28 (CβCγ)	5.9	94.9	90
Lys28 (CβCδ)	7.5	91.8	87
Gly29 (CαCO)	6.3	98.0	97
Ile31 (CβCγ1)	9.6	94.2	43
Ile31 (CβCδ)	6.7	98.7	91
Ile32 (CαCγ2)	21.8	96.6	89
Ala42 (CαCβ)	18.3	98.8	97
Ala42 (CαCO)	12.6	84.5	55

Supplement Table 4.4: Fitting parameters used for 13C-T_ρ^1-SPC5 fitting curves.

Sample: uniformly 13C & 15N labelled and recombinantly expressed Aβ1-42			
residue	**fp / ms**	**A**	**R^2_{adj} / %**
Ala21 (Cα+Cβ, Cα)	10.4	102.4	95
Val24 (Cα+Cγ, Cγ)	9.5	90.4	90
Ser26 (Cα+Cβ, Cβ)	3.3	98.7	99
Lys28 (Cγ+Cδ, Cδ)	9.7	93.6	67

Supplement Table 5.1: Experimental Details of peak integration boxes used for water-edited PDSD measurements.

Sample: uniformly 13C & 15N labelled and recombinantly expressed Aβ1-42				
residue	**Y1**	**Y2**	**X1**	**X2**
Glu3 (CαCγ)	32	33.8	53.2	55
Arg5 (CαCγ)	26.9	28.7	53	54.8
Asp7 (CβCγ)	40.4	42.2	177.9	179.7
Asp7 (CαCγ)	50.95	52.75	177.9	179.7
Ser26 (CαCβ)	64.6	66.4	56	57.8
Lys28 (CγCδ)	29	30.8	24.8	26.6
Lys28 (CδCε)	40.9	42.7	29.3	31.1
Lys28 (CβCγ)	35.3	37.1	25	26.8
Lys28 (CαCβ)	53	54.8	35.7	37.5
Lys28 (CαCε)	53.6	55.4	41	42.8

Supplement Table 5.2: Experimental Details of peak integration boxes used for water-edited SPC5 measurements.

Sample: uniformly 13C & 15N labelled and recombinantly expressed Aβ1-42				
residue	**Y1**	**Y2**	**X1**	**X2**
Gln15 (Cα+Cβ, Cα)	84	85.8	51.5	53.3
Ala21 (Cα+Cβ, Cα)	70.8	72.6	48.1	49.9
Val24 (Cβ+Cγ, Cγ)	58.9	60.7	21.9	23.7
Ser26 (Cα+Cβ, Cα)	121.2	123	55.2	57
Lys28 (Cγ+Cδ, Cδ)	54.9	56.7	28.7	30.5
Ile32 (Cβ+Cγ2, Cγ2)	60.1	61.9	16.6	18.4

Supplement Table 6: Experimental details of data analysis of water-edited- and T_ρ^1-spectra.

peak integration parameters								
experiment	box length (ppm)	SW (dir. dim.) (ppm)	SW (ind. dim.) (ppm)	points (dir. dim.)	points (ind. dim.)	points (box)	noise (rmsd) ($*10^3$)	noise (box) ($*10^3$)
^{13}C- T_ρ^1-PDSD								
0 ms	1	298	300	1024	1024	11.73	11.5	39.4
2.5 ms	1	298	300	1024	1024	11.73	11.2	38.5
5 ms	1	298	300	1024	1024	11.73	10.9	37.4
10 ms	1	298	300	1024	1024	11.73	10.8	37
^{13}C- T_ρ^1-SPC5								
0 ms	1	238	267	1024	512	8.17	6.6	19.3
4 ms	1	238	267	1024	512	8.17	6.5	18.9
8 ms	1	238	267	1024	512	8.17	6.4	18.5
water-edited PDSD								
3.25 ms	1.8	237	219	1024	512	32.75	5.5	31.3
6.5 ms	1.8	237	219	1024	512	32.75	5.3	30.5
10 ms	1.8	237	219	1024	512	32.75	6.3	36.2
water-edited SPC5								
3 ms	1.8	360	106	1024	128	11.11	22.1	73.7
4 ms	1.8	360	106	1024	128	11.11	22.6	75.3
5 ms	1.8	360	106	1024	128	11.11	21.7	72.4
6 ms	1.8	360	106	1024	128	11.11	21.2	70.7

Pulse program of ^{13}C-$T_{1\rho}$-PDSD:

File: /home/dschoelzel/home/pulse_progs/DA/tancp2dradt1rho.c Page 1 of 3

```
#include      "standard.h"
#include      "solidstandard.h"

// Define Values for Phasetables
static      int   table1[      4] = {    0, 0, 0, 0};                                          // phH90
static      int   table2[      4] = {    3, 3, 3, 3};                                          // phHhx
static      int   table3[      8] = {    0, 0, 0, 0, 2, 2, 2, 2};                              // phXhx
static      int   table4[      4] = {    1, 1, 1, 1};                                          // phXmix1
static      int   table5[      4] = {    0, 1, 2, 3};                                          // phXmix2
static      int   table6[      8] = {    0, 1, 2, 3, 2, 3, 0, 1};                              // phRec
static      int   table7[     16] = {    0, 0, 0, 0, 0, 0, 0, 0, 2, 2, 2, 2, 2, 2, 2, 2};     // phX_sl


#define phH90 t1
#define phHhx t2
#define phXhx t3
#define phXmix1 t4
#define phXmix2 t5
#define phRec t6
#define phX_sl t7

pulsesequence() {

// Define Variables and Objects and Get Parameter Values

    double   duty;

 CP hx = getcp(          "HX"  , 0.0  , 0.0  , 0,  1);
 strncpy(hx.fr,          "dec"   , 3);
 strncpy(hx.to,          "obs"   , 3);
 putCmd(     "frHX='dec'       \n " );
 putCmd(     "toHX='obs'       \n " );

 DSEQ dec = getdseq(          "H"  );
```

File: /home/dschoelzel/home/pulse_progs/DA/tancp2dradt1rho.c Page 2 of 3

```
// Set Mixing Period to N Rotor Cycles

     double   taur=    1,mix,srate;
  mix =  getval(              "tXmix"     );
  srate =  getval(                "srate"      );
     if   (srate >=          500.0   )
    taur = roundoff((                   1.0  /srate),         0.125e-6     );
     else   {
    printf(              "ABORT: Spin Rate (srate) must be greater than 500                              \n " );
    psg_abort(              1);
  }
  mix = roundoff(mix,taur);
  mix = mix - getval(                 "pwX90"   );
     if   (mix <       0.0   ) mix =       0.0   ;

// Dutycycle Protection

duty =     4.0e-6     + getval(       "pwH90"   ) + getval(         "tHX"    ) + d2
       +              2.0  *getval(     "pwX90"   ) + getval(         "ad"    ) + getval(         "rd"    ) + at;

  duty = duty/(duty + d1 +                    4.0e-6     );
     if   (duty >        0.1   ) {
    printf(              "Duty cycle         %.1f%%  >10  %%Abort!       \n " , duty*      100 );
    psg_abort(              1);
  }

// Create Phasetables

  settable(phH90,             4,table1);
  settable(phHhx,             4,table2);
  settable(phXhx,             8,table3);
  settable(phXmix1,               4,table4);
  settable(phXmix2,               4,table5);
  settable(phRec,             8,table6);
  settable(phX_sl,              16,table7);

  setreceiver(phRec);

     if   (phase1 ==         2)
    tsadd(phXhx,              1, 4);

// Begin Sequence

  txphase(phXhx); decphase(phH90);
  obspwrf(getval(             "aXhx"    )); decpwrf(getval(               "aH90"    ));
  obsunblank(); decunblank(); _unblank34();
  delay(d1);
  sp1on(); delay(               2.0e-6     ); sp1off(); delay(                 2.0e-6     );

// H to X Cross Polarization

  decrgpulse(getval(                "pwH90"   ),phH90,     0.0   ,  0.0  );
  decphase(phHhx);
   _cp_{hx,phHhx,phXhx};
```

```
// F2 Indirect Period for X

  txphase(phXmix1);
  obspwrf(getval(          "aX90"   ));
     double   time1 = getTimeMarker();

  _dseqon(dec);
  delay(d2);
  _dseqoff(dec);


// X Channel Spinlock

  decpwrf(getval(          "aHlock"    ));
  obspwrf(getval(          "aXlock"    ));
  txphase(phX_sl);
  decunblank(); decon();
  rgpulse(getval(          "tlock"     ),phX_sl,      0.0  , 0.0  );
  decoff();


// RAD(DARR) Mixing For X
     double   time2 = getTimeMarker();
  printf(        "increment =        %dtime2 =       %f us  \n " ,d2_index,(time2-time1)*            1.0e6   );
  decpwrf(getval(          "aHmix"   ));
  obspwrf(getval(          "aX90"   ));
  decunblank();            //decon();
  rgpulse(getval(          "pwX90"  ),phXmix1,     0.0  , 0.0  );
  txphase(phXmix2);
  obsunblank();
  delay(mix);
  rgpulse(getval(          "pwX90"  ),phXmix2,     0.0  , 0.0  );


// Begin Acquisition

  _dseqon(dec);
  obsblank(); _blank34();
  delay(getval(          "rd"   ));
  startacq(getval(            "ad"   ));
  acquire(np,          1/sw);
  endacq();
  _dseqoff(dec);
  obsunblank(); decunblank(); _unblank34();
}
```

Pulse program of ^{13}C-$T_{1\rho}$-SPC5:

File: /home/dschoelzel/home/pulse_progs/DA/spc5t1rho2d.c Page 1 of 4

```
#include      "standard.h"
#include      "solidstandard.h"

// Define Values for Phasetables

static      int   table1[      4] = {     1, 1, 1, 1};                                    // phH90
static      int   table2[      8] = {     0, 0, 0, 0, 2, 2, 2, 2};                        // phXhx
static      int   table3[      4] = {     0, 0, 0, 0};                                    // phHhx
static      int   table4[      4] = {     3, 3, 3, 3,};                                   // phXmix1
static      int   table5[      4] = {     0, 1, 2, 3};                                    // phXmix2
static      int   table6[      8] = {     0, 3, 2, 1, 2, 1, 0, 3};                        // phRec
static      int   table7[      16] = {     0, 0, 0, 0, 0, 0, 0, 0, 2, 2, 2, 2, 2, 2, 2, 2};   // pHx_sl

#define phH90 t1
#define phXhx t2
#define phHhx t3
#define phXmix1 t4
#define phXmix2 t5
#define phRec t6
#define phX_sl t7

static      double   d2_init;

pulsesequence() {

// Define Variables and Objects and Get Parameter Values

  CP hx = getcp(            "HX"  , 0.0  , 0.0  , 0,  1};
  strncpy(hx.fr,            "dec"   , 3};
  strncpy(hx.to,            "obs"   , 3};
  putCmd(      "frHX='dec'       \n " };
  putCmd(      "toHX='obs'       \n " };

  MPSEQ spc5 = getspc5(             "spc5X"    , 0, 0.0  , 0.0  , 0,  1};
  MPSEQ spc5ref = getspc5(                "spc5X"    ,spc5.iSuper,spc5.phAccum,spc5.phInt,                  1,  1};
  strncpy(spc5.ch,            "obs"   , 3};
  putCmd(      "chXspc5='obs'       \n " };
```

```
DSEQ dec = getdseq(          "H"  );
strncpy(dec.t.ch,            "dec"   , 3);
putCmd(     "chHtppm='dec'      \n " );
strncpy(dec.s.ch,            "dec"   , 3);
putCmd(     "chHspinal='dec'         \n " );

// Set Constant-time Period for d2.

    if   (d2_index ==        0) d2_init = getval(          "d2"   );
    double   d2_ = (ni -          1)/sw1 + d2_init;
putCmd(     "d2acqret =       %f\n " ,roundoff(d2_,        12.5e-9    ));
putCmd(     "d2dwret =       %f\n " ,roundoff(      1.0  /sw1,   12.5e-9    ));


// Copy Current Parameters to Processed

putCmd(     "groupcopy('current','processed','acquisition')"                          );


// Dutycycle Protection

DUTY d = init_dutycycle();
d.dutyon = getval(           "pwH90"  ) + getval(         "tHX"   ) + spc5.t + spc5ref.t;
d.dutyoff = d1 +             4.0e-6     +    2.0   *getval(     "tZF"    );
d.c1 = d.c1 + (!strcmp(dec.seq,                    "tppm"  ));
d.c1 = d.c1 + ((!strcmp(dec.seq,                    "tppm"  )) && (dec.t.a >          0.0  ));
d.t1 = d2_ + getval(         "rd"   ) + getval(        "ad"   ) + at;
d.c2 = d.c2 + (!strcmp(dec.seq,                    "spinal"      ));
d.c2 = d.c2 + ((!strcmp(dec.seq,                    "spinal"      )) && (dec.s.a >          0.0  ));
d.t2 = d2_ + getval(         "rd"   ) + getval(        "ad"   ) + at;
d = update_dutycycle(d);
abort_dutycycle(d,           10.0   );

// Set Phase Tables

settable(phH90,          4,table1);
settable(phXhx,          8,table2);
settable(phHhx,          4,table3);
settable(phXmix1,        4,table4);
settable(phXmix2,        4,table5);
settable(phRec,          8,table6);
settable(phX_sl,         16,table7);

// Add STATES-TPPI (STATES + "FAD")

    double   obsstep =       360.0   /(PSD*   8192 ),
     srate;
     srate=getval(                "srate"     );

    if   (phase1 ==       2)
   initval((              45.0   /obsstep),v1);
    else
   initval(            0.0   ,v1);
 initval((d2*srate*             180.0   /obsstep),v2);
 obsstepsize(obsstep);
```

File: /home/dschoelzel/home/pulse_progs/DA/spc5t1rho2d.c Page 3 of 4

```
  setreceiver(phRec);

// Begin Sequence

  txphase(phXhx); decphase(phH90);
  obspwrf(getval(          "aXhx"   )); decpwrf(getval(          "aH90"   ));
  obsunblank(); decunblank(); _unblank34();
  delay(d1);
  sp1on(); delay(          2.0e-6   ); sp1off(); delay(          2.0e-6   );

// H to X Cross Polarization

  decrgpulse(getval(          "pwH90"  ),phH90,     0.0  , 0.0  );
  decphase(phHhx);
   _cp_{hx,phHhx,phXhx};
  obspwrf(getval(          "aX90"   ));

// X Channel Spinlock

  decpwrf(getval(          "aHlock"    ));
  obspwrf(getval(          "aXlock"    ));
  txphase(phX_sl);
  decunblank(); decon();
  rgpulse(getval(          "tlock"     ),phX_sl,     0.0  , 0.0  );
  decoff();

// Mixing with SPC5 Recoupling-Period One

  obspwrf(getval(          "aX90"   ));
  rgpulse(getval(          "pwX90"  ),phXmix1,     0.0  , 0.0  );
  obspwrf(getval(          "aXspc5"    ));
  decoff();
  xmtrphase(v1); txphase(phXmix1);
  delay(getval(          "tZF"    ));
  decpwrf(getval(          "aHmix"    ));
 decoffset(getval(          "ofHlg"    ));
  decunblank();
  decon();
  _mpseq(spc5, phXmix1);
  decoff();
  decoffset(getval(          "dof"    ));

// F1 Indirect Period For X

  xmtrphase(v2); txphase(phXmix2);
  _dseqon(dec);
  delay(d2);
  _dseqoff(dec);

// Mixing with SPC5 Recoupling-Period Two

  decpwrf(getval(          "aHmix"    ));
 decoffset(getval(          "ofHlg"    ));
  decunblank();
  decon();
  _mpseq(spc5ref, phXmix2);
  decoff();
```

```
  decoffset(getval(          "dof"   ));
  obspwrf(getval(          "aX90"   ));
  xmtrphase(zero); txphase(phXmix2);
  delay(getval(          "tZF"   ));
  rgpulse(getval(          "pwX90"  ),phXmix2,     0.0  , 0.0  );

// Begin Acquisition

  _dseqon(dec);
  obsblank(); _blank34();
  delay(getval(          "rd"   ));
  startacq(getval(          "ad"   ));
  acquire(np,          1/sw);
  endacq();
  _dseqoff(dec);
  obsunblank(); decunblank(); _unblank34();
}
```

Pulse program of water-edited PDSD:

File: /home/dschoelzel/home/pulse_progs/DA/waterccpdsd.c Page 1 of 4

```
#include      "standard.h"
#include      "solidstandard.h"

// Define Values for Phasetables

static      int   table1[      4] = {     0, 2, 0, 2};
static      int   table2[      4] = {     1, 1, 1, 1};
static      int   table3[      4] = {     3, 3, 3, 3};
static      int   table4[      4] = {     0, 0, 2, 2};

static      int   table5[      4] = {     1, 1, 1, 1};

static      int   table6[      16] = {     0, 0, 0, 0, 1, 1, 1, 1, 2, 2, 2, 2, 3, 3, 3, 3};

static      int   table7[      16] = {     0, 2, 2, 0, 1, 3, 3, 1, 0, 2, 2, 0, 1, 3, 3, 1};

static      double   pwH90;

static      double   pwH180;

static      double   phH180;

#define phH90 t1
#define phH180 t2
#define phHhx t3
#define phXhx t4
#define phXmix1 t5
#define phXmix2 t6
#define phRec t7

pulsesequence() {


// Define Variables and Objects and Get Parameter Values

    double   duty;

 CP hx = getcp(          "HX"  , 0.0   , 0.0   , 0,  1);
 strncpy(hx.fr,          "dec"   , 3);
 strncpy(hx.to,          "obs"   , 3);
 putCmd(     "frHX='dec'       \n " );
 putCmd(     "toHX='obs'       \n " );

 DSEQ dec = getdseq(           "H" );
```

```
// Set Mixing Period to N Rotor Cycles

   double taur=1,mix,srate;
   mix =  getval("tXmix");
   srate =  getval("srate");
   if (srate >= 500.0)
      taur = roundoff((1.0/srate), 0.125e-6);
   else {
      printf("ABORT: Spin Rate (srate) must be greater than 500\n");
      psg_abort(1);
   }
   mix = roundoff(mix,taur);
   mix = mix - getval("pwX90");
   if (mix < 0.0) mix = 0.0;


// Dutycycle Protection

duty = 4.0e-6 + getval("pwH90") + getval("tHX") + d2 +
          mix + 2.0*getval("pwX90") + getval("ad") + getval("rd") + at;
   duty = duty/(duty + d1 + 4.0e-6);
   if (duty > 0.1) {
      printf("Duty cycle %.1f%% >10%%. Abort!\n", duty*100);
      psg_abort(1);
  }


// Create Phasetables

   settable(phH90,4,table1);
   settable(phH180,4,table2);
   settable(phHhx,4,table3);
   settable(phXhx,4,table4);
   settable(phXmix1,4,table5);
   settable(phXmix2,16,table6);
   settable(phRec,16,table7);
   setreceiver(phRec);


   if (phase1 == 2)
      tsadd(phH90,1,4),
      tsadd(phH180,1,4);

   if (phase2 == 2)
      tsadd(phXhx,1,4);


// Begin Sequence

   txphase(phXhx); decphase(phH90);
   obspwrf(getval("aXhx")); decpwrf(getval("aH90"));
   obsunblank(); decunblank(); _unblank34();
   delay(d1);
   sp1on(); delay(2.0e-6); sp1off(); delay(2.0e-6);
```

File: /home/dschoelzel/home/pulse_progs/DA/waterccpdsd.c Page 3 of 4

```
// initial 90° pulse

  decrgpulse(getval(          "pwH90"  ),phH90,     0.0  ,  0.0  );


// T2filter

  delay(getval(          "ddeph"   ));
  decrgpulse(getval(          "pwH180"  ),phH180,     0.0  ,  0.0  );
  delay(getval(          "ddeph"   ));


// F1 indirect period for H

  delay(d2);


// H to X Cross Polarization

  decrgpulse(getval(          "pwH90"  ),phH90,     0.0  ,  0.0  );
  decphase(phHhx);
   _cp_{hx,phHhx,phXhx};


// F2 Indirect Period for X

  txphase(phXmix1);
  obspwrf(getval(          "aX90"   ));
     double   time1 = getTimeMarker();

  _dseqon(dec);
  delay(d2);
  _dseqoff(dec);


// RAD(DARR) Mixing For X
     double   time2 = getTimeMarker();
  printf(          "increment =          %dtime2 =       %f us  \n " ,d2_index,(time2-time1)*          1.0e6   );
  decpwrf(getval(          "aHmix"   ));
  decunblank(); decon();
  rgpulse(getval(          "pwX90"  ),phXmix1,     0.0  ,  0.0  );
  txphase(phXmix2);
  obsunblank();
  delay(mix);
  rgpulse(getval(          "pwX90"  ),phXmix2,     0.0  ,  0.0  );
  decoff();

// Begin Acquisition

  _dseqon(dec);
  obsblank(); _blank34();
  delay(getval(          "rd"   ));
  startacq(getval(          "ad"   ));
  acquire(np,          1/sw);
  endacq();
  _dseqoff(dec);
```

```
   obsunblank(); decunblank(); _unblank34();
}
```

Pulse program of water-edited SPC5:

File: /home/dschoelzel/home/pulse_progs/DA/waterspc5_2d.c Page 1 of 4

```
#include      "standard.h"
#include      "solidstandard.h"

// Define Values for Phasetables

static      int   table1[      8] = {     0, 0, 0, 0, 2, 2, 2, 2};                                                    // phH90
static      int   table2[      4] = {     0, 0, 0, 0};                                                                // phH180
static      int   table3[      4] = {     2, 2, 2, 2};                                                                // phHmix1
static      int   table4[      16] = {     0, 0, 0, 0, 0, 0, 0, 0, 2, 2, 2, 2, 2, 2, 2, 2};                          // phHmix2
static      int   table5[      4] = {     3, 3, 3, 3};                                                                // phHhx
static      int   table6[      4] = {     3, 3, 3, 3};                                                                // phXhx
static      int   table7[      4] = {     0, 0, 0, 0};                                                                // phXmix1
static      int   table8[      4] = {     0, 1, 2, 3};                                                                // phXmix2
static      int   table9[      16] = {     0, 3, 2, 1, 2, 1, 0, 3, 2, 1, 0, 3, 0, 3, 2, 1};                          // phRec

#define phH90 t1
#define phH180 t2
#define phHmix1 t3
#define phHmix2 t4
#define phHhx t5
#define phXhx t6
#define phXmix1 t7
#define phXmix2 t8
#define phRec t9

static      double   d2_init;
pulsesequence() {


// Define Variables and Objects and Get Parameter Values

  CP hx = getcp(            "HX"  , 0.0   , 0.0   , 0,  1);
  strncpy(hx.fr,            "dec"   , 3);
  strncpy(hx.to,            "obs"   , 3);
  putCmd(      "frHX='dec'       \n " );
  putCmd(      "toHX='obs'       \n " );

  MPSEQ spc5 = getspc5(             "spc5X"     , 0,  0.0   , 0.0   , 0,  1);
  MPSEQ spc5ref = getspc5(                "spc5X"     ,spc5.iSuper,spc5.phAccum,spc5.phInt,                  1,  1);
  strncpy(spc5.ch,              "obs"   , 3);
  putCmd(      "chXspc5='obs'       \n " );
```

```
DSEQ dec = getdseq(          "H" );
strncpy(dec.t.ch,            "dec"  , 3);
putCmd(    "chHtppm='dec'     \n " );
strncpy(dec.s.ch,            "dec"  , 3);
putCmd(    "chHspinal='dec'        \n " );

// Set Constant-time Period for d2.

   if  (d2_index ==       0) d2_init = getval(          "d2"  );
   double  d2_ = (ni -         1)/sw1 + d2_init;
putCmd(    "d2acqret =       %f\n " ,roundoff(d2_,       12.5e-9   });
putCmd(    "d2dwret =      %f\n " ,roundoff(     1.0  /sw1,   12.5e-9   });


// Copy Current Parameters to Processed


putCmd(    "groupcopy('current','processed','acquisition')"                          );

// Dutycycle Protection

DUTY d = init_dutycycle();
d.dutyon = getval(           "pwH90"  ) + getval(        "tHX"  ) + spc5.t + spc5ref.t;
d.dutyoff = d1 +           4.0e-6    +   2.0  *getval(    "tZF"  );
d.c1 = d.c1 + (!strcmp(dec.seq,                    "tppm"  });
d.c1 = d.c1 + ((!strcmp(dec.seq,                    "tppm"  }) && (dec.t.a >          0.0  });
d.t1 = d2_ + getval(         "rd"  ) + getval(       "ad"  ) + at;
d.c2 = d.c2 + (!strcmp(dec.seq,                    "spinal"     });
d.c2 = d.c2 + ((!strcmp(dec.seq,                    "spinal"     }) && (dec.s.a >          0.0  });
d.t2 = d2_ + getval(         "rd"  ) + getval(       "ad"  ) + at;
d = update_dutycycle(d);
abort_dutycycle(d,           10.0  );


// Set Phasetables

settable(phH90,          8,table1);
settable(phH180,           4,table2);
settable(phHmix1,          4,table3);
settable(phHmix2,          16,table4);
settable(phHhx,          4,table5);
settable(phXhx,          4,table6);
settable(phXmix1,          4,table7);
settable(phXmix2,          4,table8);
settable(phRec,          16,table9);
setreceiver(phRec);

// Add STATES-TPPI (STATES + "FAD")

   double  obsstep =       360.0  /(PSD*  8192 },
   srate;
    srate=getval(                "srate"    };

   if  (phase1 ==       2)
  initval({             45.0  /obsstep),v1);
```

```
    else
  initval(        0.0  ,v1);
initval((d2*srate*        180.0   /obsstep),v2);

obsstepsize(obsstep);
setreceiver(phRec);


// Begin Sequence

txphase(phXhx); decphase(phH90);
obspwrf(getval(        "aXhx"   )); decpwrf(getval(        "aH90"   ));
obsunblank(); decunblank(); _unblank34();
delay(d1);
sp1on(); delay(        2.0e-6    ); sp1off(); delay(        2.0e-6    );


// initial 90° pulse

decrgpulse(getval(        "pwH90"  ),phH90,     0.0  , 0.0  );


// T2filter

decpwrf(getval(        "aH180"   ));
delay(getval(        "ddeph"   ));
decrgpulse(getval(        "pwH180"  ),phH180,     0.0  , 0.0  );
delay(getval(        "ddeph"   ));


// 90° pulse on H

decpwrf(getval(        "aH90"   ));
decrgpulse(getval(        "pwH90"  ),phHmix1,     0.0  , 0.0  );


// tau delay period for H

delay(getval(        "tHmix"    ));


// 90° pulse on H

decrgpulse(getval(        "pwH90"  ),phHmix2,     0.0  , 0.0  );


// H to X Cross Polarization


decphase(phHhx);
 _cp_{hx,phHhx,phXhx};
obspwrf(getval(        "aX90"   ));

// Mixing with SPC5 Recoupling-Period One

rgpulse(getval(        "pwX90"  ),phXmix1,     0.0  , 0.0  );
obspwrf(getval(        "aXspc5"    ));
```

```
  decoff();
  xmtrphase(v1); txphase(phXmix1);
  delay(getval(          "tZF"   ));
  decpwrf(getval(          "aHmix"   ));
 decoffset(getval(          "ofHlg"    ));
  decunblank();
  decon();
  _mpseq(spc5, phXmix1);
  decoff();
  decoffset(getval(          "dof"   ));

// F1 Indirect Period For X

  xmtrphase(v2); txphase(phXmix2);
  _dseqon(dec);
  delay(d2);
  _dseqoff(dec);

// Mixing with SPC5 Recoupling-Period Two

  decpwrf(getval(          "aHmix"   ));
 decoffset(getval(          "ofHlg"    ));
  decunblank();
  decon();
  _mpseq(spc5ref, phXmix2);
  decoff();
  decoffset(getval(          "dof"   ));
  obspwrf(getval(          "aX90"   ));
  xmtrphase(zero); txphase(phXmix2);
  delay(getval(          "tZF"   ));
  rgpulse(getval(          "pwX90"  ),phXmix2,     0.0  , 0.0  );

// Begin Acquisition

  _dseqon(dec);
  obsblank(); _blank34();
  delay(getval(          "rd"   ));
  startacq(getval(          "ad"   ));
  acquire(np,          1/sw);
  endacq();
  _dseqoff(dec);
  obsunblank(); decunblank(); _unblank34();
}
```

8

References

[1] D. J. Selkoe. Alzheimer's Disease. Cold Spring Harb Perspect Biol., 3(7):1-16, 2011.

[2] G. G. Glenner and C. W. Wong. Alzheimer's disease and Down's syndrome: Sharing of a unique cerebrovascular amyloid fibril protein. Biochem. Biophys. Res. Commun., 122:1131–1135, 1984.

[3] C. L. Masters, G. Simms, N. A. Weinman, G. Multhaup, B. L. McDonald and K. Beyreuther. Amyloid plaque core protein in Alzheimer disease and Down syndrome. Proc. Natl. Acad. Sci., 82:4245–4249, 1985.

[4] J. A. Hardy and G. A. Higgins. Alzheimer's disease: the amyloid cascade hypothesis. Science, 256(5054):184-185, 1992.

[5] A. Goate, M. C. Chartier-Harlin and M. Mullan. Segregation of a missense mutation in the amyloid precursor protein gene with familial Alzheimer's disease, Nature, 349(6311):704–706, 1991.

[6] E. Levy-Lahad, W. Wasco and P. Poorkaj. Candidate gene for the chromosome 1 familial Alzheimer's disease locus, Science, 269(5226):973–977, 1995.

[7] R. Sherrington, E. I. Rogaev and Y. Liang. Cloning of a gene bearing missense mutations in early-onset familial Alzheimer's disease, Nature, 375(6534):754–760, 1995.

[8] C. Reitz, Alzheimer's Disease and the Amyloid Cascade Hypothesis: A Critical Review. Int. J. Alzheimers. Dis., 2012:1–11, 2012.

[9] G. Thinakaran and E. H. Koo. Amyloid Precursor Protein Trafficking, Processing, and Function. J. Biol. Chem., 283(44):29615–29619, 2008.

[10] D. J. Selkoe. Alzheimer's Disease: Genes, Proteins, and Therapy. Phys. Rev., 81(2):741-766, 2001.

[11] M. R. Nilsson. Techniques to study amyloid fibril formation in vitro. Methods, 34(1):151–160, 2004.

[12] S. I. Cohen, M. Vendruscolo, M. E. Welland, C. M. Dobson, E. M. Terentjev and T. P. Knowles. Nucleated polymerization with secondary pathways. I. Time evolution of the principal moments. J. Chem. Phys., 135:65–105, 2011.

[13] J. E. Morley and S. A. Farr. The role of amyloid-beta in the regulation of memory. Biochem. Pharm., 88(4):479-485, 2014.

[14] M. T. Lin and M. F. Beal. Alzheimer's APP mangles mitochondria. Nat. Med., 12:1241–1243, 2006.

[15] L. Devi and M. Ohno. Mitochondrial dysfunction and accumulation of the B-secretase-cleaved C-terminal fragment of APP in Alzheimer's disease transgenic mice. Neurobiol. Dis., 45:417–424, 2012.

[16] S. J. Soscia, J. E. Kirby, K. J. Washicosky, S. M. Tucker, M. Ingelsson, B. Hyman, M. A. Burton, L. E. Goldstein, S. Duong, R. E. Tanzi and R. D. Moir. The Alzheimer's Disease-Associated Amyloid β-Protein Is an Antimicrobial Peptide. PloS One, 5(3):1-10, 2010.

[17] C. M. Dobson. Protein misfolding, evolution and disease. Trends in Biochem. Sciences, 24(9):329-332, 1999.

[18] D. E. Otzen, editor. Amyloid Fibrils and Prefibrillar Aggregates: Molecular and Biological Properties. Wiley-VCH, Weinheim, Germany, 1st edition, 2013.

[19] M. Sunde, L. C. Serpell, M. Bartlam, P. E. Fraser, M. B. Pepys and C. C. Blake. Common core structure of amyloid fibrils by synchrotron X-ray diffraction. J. Mol. Biol., 273:729–739, 1997.

[20] D. S. Eisenberg and M. Jucker. The amyloid state of proteins in human diseases. Cell, 148:1188–1203, 2016.

[21] M. R. Sawaya, S. Sambashivan, R. Nelson, M. I. Ivanova, S. A. Sievers, M. I. Apostol, M. J. Thompson, M. Balbirnie, J. J. Wiltzius, H. T. McFarlane, A. O. Madsen, C. Riekel and D. Eisenberg. Atomic structures of amyloid cross-beta spines reveal varied steric zippers. Nature, 447(7143):453–457, 2007.

[22] D. S. Eisenberg and M. R. Sawaya. Structural Studies of Amyloid Proteins at the Molecular Level. Annu. Rev. Biochem., 86:69-95, 2017.

[23] R. G. S. Spencer, K. J. Halverson, M. Auger, .A E. McDermott, R. G. Griffin, and P. T. Lansbury Jr. An unusual peptide conformation may precipitate amyloid formation in Alzheimer's disease: application of solid-state NMR to the determination of protein secondary structure. Biochem., 30(43):10382–10387, 1991.

[24] P. T. Lansbury Jr., P. R. Costa, J. M. Griffiths, E. J. Simon, M. Auger, K. J. Halverson, D. A. Kocisko, Z. S. Hendsch, T. T. Ashburn, R. G.S. Spencer, B. Tidor and R. G. Griffin. Structural model for the β-amyloid fibril based on interstrand alignment of an antiparallel-sheet comprising a C-terminal peptide. Nature Struc. Bio., 2:990–998, 1995.

[25] P. R. Costa, D. A. Kocisko, B. Q. S, P. T. Lansbury and R. G. Griffin. Determination of Peptide Amide Configuration in a Model Amyloid Fibril by Solid-State NMR. J. Am. Chem. Soc., 119(43):10487–10493, 1997.

[26] A. T. Petkova, G. Buntkowsky, F. Dyda, R. D. Leapman, W.-M. Yau and R. Tycko. Solid State NMR Reveals a pH-dependent Antiparallel β-Sheet Registry in Fibrils Formed by a β-Amyloid Peptide. J. Mol. Biol., 335(1):247-260, 2004.

[27] Z. Bu, Y. Shi, D. J. E. Callaway and R. Tycko. Molecular Alignment within β-Sheets in Aβ14-23 Fibrils: Solid-State NMR Experiments and Theoretical Predictions. Biophys. J., 92(2):594–602, 2007.

[28] O. N. Antzutkin, R. D. Leapman, J. J. Balbach and Robert Tycko. Supramolecular Structural Constraints on Alzheimer's β-Amyloid Fibrils from Electron Microscopy and Solid-State Nuclear Magnetic Resonance. Biochem., 41(51):15436–15450, 2002.

[29] J. J. Balbach, Y. Ishii, O. N. Antzutkin, R. D. Leapman, N. W. Rizzo, F. Dyda, J. Reed and R. Tycko. Amyloid Fibril Formation by Aβ16-22, a Seven-Residue Fragment of the Alzheimer's β-Amyloid Peptide, and Structural Characterization by Solid State NMR. Biochem., 39(45):13748–13759, 2000.

[30] D. J.Gordon, J. J. Balbach, R. Tycko and S. C. Meredith. Increasing the Amphiphilicity of an Amyloidogenic Peptide Changes the β-Sheet Structure in the Fibrils from Antiparallel to Parallel. Biophys. J., 86(1):428-434, 2004.

[31] R. Tycko and Y. Ishii. Constraints on Supramolecular Structure in Amyloid Fibrils from Two-Dimensional Solid-State NMR Spectroscopy with Uniform Isotopic Labeling. J. Am. Chem. Soc., 125(22):6606–6607, 2003.

[32] T. L. S. Benzinger, D. M. Gregory, T. S. Burkoth, H. Miller-Auer, D. G. Lynn, R. E. Botto and S. C. Meredith. Two-Dimensional Structure of β-Amyloid(10-35) Fibrils. Biochem., 39(12):3491–3499, 2000.

[33] T. L. S. Benzinger, D. M. Gregory, T. S. Burkoth, H. Miller-Auer, D. G. Lynn, R. E. Botto and S. C. Meredith. Propagating structure of Alzheimer's β-amyloid(10-35) is parallel β-sheet with residues in exact register. Proc. Natl. Acad. Sci. U.S.A., 95(23):13407-13412, 1998.

[34] A. K. Paravastu, A. T. Petkova and R. Tycko. Polymorphic Fibril Formation by Residues 10–40 of the Alzheimer's β-Amyloid Peptide. Biophys. J., 90(12):4618-4629, 2006.

[35] A. T. Petkova, Y. Ishii, J. J. Balbach, O. N. Antzutkin, R. D. Leapman, F. Delaglio and R. Tycko. A structural model for Alzheimer's β-amyloid fibrils based on experimental constraints from solid state NMR. Proc. Natl. Acad. Sci. U.S.A., 99(26):16742-16747, 2002.

[36] O. N. Antzutkin, J. J. Balbach and R. Tycko. Site-Specific Identification of Non-β-Strand Conformations in Alzheimer's β-Amyloid Fibrils by Solid-State NMR. Biophys. J., 84(5):3326-3335, 2003.

[37] A. T. Petkova, R. D. Leapman, Z. Guo, W.-M. Yau, M. P. Mattson and R. Tycko. Self-Propagating, Molecular-Level Polymorphism in Alzheimer's β-Amyloid Fibrils. Science, 307(5707):262-265, 2005.

[38] A. T. Petkova, W.-M. Yau and R. Tycko. Experimental Constraints on Quaternary Structure in Alzheimer's β-Amyloid Fibrils. Biochem., 45(2):498–512, 2006.

[39] T. Lührs, C. Ritter, M. Adrian, D. Riek-Loher, B. Bohrmann, H. Döbeli, D. Schubert and Roland Riek. 3D structure of Alzheimer's amyloid-β(1-42) fibrils. Proc. Natl. Acad. Sci. U.S.A., 102(48):17342-17347, 2005.

[40] Y. Xiao, B. Ma, D. McElheny, S. Parthasarathy, F. Long, M. Hoshi, R. Nussinov and Y. Ishii. Aβ(1–42) Fibril Structure Illuminates Self-recognition and Replication of Amyloid in Alzheimer's disease. Nat. Struct. Mol. Biol., 22(6)499–505, 2015.

[41] M. T. Colvin, R. Silvers, Q. Zhe Ni, T. V. Can, I. Sergeyev, M. Rosay, K. J. Donovan, B. Michael, J. Wall, S. Linse and R. G. Griffin. Atomic Resolution Structure of Monomorphic Aβ42 Amyloid Fibrils. J. Am. Chem. Soc., 138(30):9663–9674, 2016.

[42] M. Aulikki Wälti, F. Ravotti, H. Arai, C. G. Glabe, J. S. Wall, A. Böckmann, P. Güntert, B. H. Meier and R. Riek. Atomic-resolution structure of a disease-relevant Aβ(1–42) amyloid fibril. Proc. Natl. Acad. Sci. U.S.A., 113(34):4976-4984, 2016.

[43] W. Qiang, W.-M. Yau, Y. Luo, M. P. Mattson and R. Tycko. Antiparallel β-sheet architecture in Iowa-mutant β-amyloid fibrils. Proc. Natl. Acad. Sci. U.S.A., 109(12):4443-4448, 2012.

[44] N. Ferguson, J. Becker, H. Tidow, S. Tremmel, T. D. Sharpe, G. Krause, J. Flinders, M. Petrovich, J. Berriman, H. Oschkinat and A. R. Fersht. General

structural motifs of amyloid protofilaments. Proc. Natl. Acad. Sci. U.S.A., 103(44):16248-16253, 2006.

[45] S. Luca, W.-M. Yau, R. Leapman and R. Tycko. Peptide Conformation and Supra-molecular Organization in Amylin Fibrils: Constraints from Solid-State NMR. Biochem., 46(47):13505-13522, 2007.

[46] K. Iwata, T. Fujiwara, Y. Matsuki, H. Akutsu, S. Takahashi, H. Naiki, and Y. Goto. 3D structure of amyloid protofilaments of β2-microglobulin fragment probed by solid-state NMR. Proc. Natl. Acad. Sci. U.S.A., 103(48):18119-18124, 2006.

[47] J. C. C. Chan, N. A. Oyler, W.-M. Yau and R. Tycko. Parallel β-Sheets and Polar Zippers in Amyloid Fibrils Formed by Residues 10-39 of the Yeast Prion Protein Ure2p. Biochem., 44(31):10669–10680, 2005.

[48] J.-X. Lu, W. Qiang, W.-M. Yau, C. D. Schwieters, S. C. Meredith and R. Tycko. Molecular Structure of β-Amyloid Fibrils in Alzheimer's Disease Brain Tissue. Cell, 154(6):1257-1268, 2013.

[49] A. K. Schütz, T. Vagt, M. Huber, O. Y. Ovchinnikova, R. Cadalbert, J. Wall, P. Güntert, A. Böckmann, R. Glockshuber, B. H. Meier. Atomic-Resolution Three-Dimensional Structure of Amyloid β Fibrils Bearing the Osaka Mutation. Angewandte Chemie Intern. Ed., 54(1):331-335, 2015.

[50] W. Qiang, W.-M. Yau, J.-X. Lu, J. Collinge and R. Tycko. Structural variation in amyloid-β fibrils from Alzheimer's disease clinical subtypes. Nature, 541:217–221, 2017.

[51] C. Ritter, M.-L. Maddelein, A. B. Siemer, T. Lührs, M. Ernst, B. H. Meier, S. J. Saupe and R. Riek. Correlation of structural elements and infectivity of the HET-s prion. Nature, 435:844–848, 2005.

[52] E. Vázquez-Fernández, M. R. Vos, P. Afanasyev, L. Cebey, A. M. Sevillano, E. Vidal, I. Rosa, L. Renault, A. Ramos, P. J. Peters, J. J. Fernández, M. van Heel, H. S. Young , J. R. Requena and H. Wille. The Structural Architecture of an Infectious Mammalian Prion Using Electron Cryomicroscopy. PLOS Pathogens, 12(9):1-21, 2016.

[53] M. D. Tuttle, G. Comellas, A. J. Nieuwkoop, D. J. Covell, D. A. Berthold, K. D. Kloepper, J. M. Courtney, J. K. Kim, A. M. Barclay, A. Kendall, W. Wan, G. Stubbs, C. D. Schwieters, V. M. Y. Lee, J. M. George and C. M. Rienstra. Solid-state NMR structure of a pathogenic fibril of full-length human α-synuclein. Nat. Struct. Mol. Biol., 23:409–415, 2016.

[54] A. W. P. Fitzpatrick, B. Falcon, S. He, A. G. Murzin, G. Murshudov, H. J. Garringer, R. A. Crowther, B. Ghetti, M. Goedert and S. H. W. Scheres. Cryo-EM structures of tau filaments from Alzheimer's disease. Nature, 547:185–190, 2017.

[55] D. T. Murray, M. Kato, Yi Lin, K. R. Thurber, I. Hung, S. L. McKnight and R. Tycko. Structure of FUS Protein Fibrils and Its Relevance to Self-Assembly and Phase Separation of Low-Complexity Domains. Cell, 171(3):615–627, 2017.

[56] D. Eisenberg and M. Jucker. The amyloid state of proteins in human diseases. Cell, 148(6):1188-203, 2012.

[57] M. Balbirnie, R. Grothe and D. S. Eisenberg. An amyloid-forming peptide from the yeast prion Sup35 reveals a dehydrated β-sheet structure for amyloid. Proc. Natl. Acad. Sci. U.S.A., 98(5):2375-2380, 2001.

[58] R. Nelson, M. R. Sawaya, M. Balbirnie, A. Madsen, C. Riekel, R. Grothe and D. Eisenberg. Structure of the cross-β spine of amyloid-like fibrils. Nature, 435(7043):773–778, 2005.

[59] P. C. A. van der Wel, J. R. Lewandowski and R. G. Griffin. Solid-State NMR Study of Amyloid Nanocrystals and Fibrils Formed by the Peptide GNNQQNY from Yeast Prion Protein Sup35p. J. Am. Chem. Soc., 129(16):5117–5130, 2007.

[60] P. C. A. van der Wel, J. R. Lewandowski and R. G. Griffin. Structural Characterization of GNNQQNY Amyloid Fibrils by Magic Angle Spinning NMR. Biochem., 49(44):9457–9469, 2010.

[61] C. Wasmer, A. Lange, H. Van Melckebeke, A. B. Siemer†, R. Riek, B. H. Meier. Amyloid Fibrils of the HET-s(218–289) Prion Form a β Solenoid with a Triangular Hydrophobic Core. Science, 319(5869):1523-1526, 2008.

[62] J.-P. Colletier, A. Laganowsky, M. Landau, M. Zhao, A. B. Soriaga, L. Goldschmidt, D. Flot, D. Cascio, M. R. Sawaya and D. Eisenberg. Molecular basis for amyloid-β polymorphism. Proc. Natl. Acad. Sci. U.S.A., 108(41):16938-16943, 2011.

[63] R. Tycko. Physical and structural basis for polymorphism in amyloid fibrils. Protein Science, 23(11):1528—1539, 2014.

[64] A. K. Paravastu, R. D. Leapman, W.-M. Yau and R. Tycko. Molecular structural basis for polymorphism in Alzheimer's β-amyloid fibrils. Proc. Natl. Acad. Sci. U.S.A., 105(47):18349-18354, 2008.

[65] W. Qiang, W.-M. Yau and R. Tycko. Structural Evolution of Iowa Mutant β-Amyloid Fibrils from Polymorphic to Homogeneous States under Repeated Seeded Growth. J. Am. Chem. Soc., 133(11):4018–4029, 2011.

[66] R. Tycko. Amyloid Polymorphism: Structural Basis and Neurobiological Relevance. Neuron, 86(3):632-645, 2015.

[67] C. A. Lasagna-Reeves, C. G. Glabe and R. Kayed. Amyloid-β Annular Protofibrils Evade Fibrillar Fate in Alzheimer Disease Brain. J. Biol. Chem., 286(25):22122–22130, 2011.

[68] A. J. Nicoll, S. Panico, D. B. Freir, D. Wright, C. Terry, E. Risse, C. E. Herron, T. O'Malley, J. D. F. Wadsworth, M. A. Farrow, D. M. Walsh, H. R. Saibil and J. Collinge. Amyloid-β nanotubes are associated with prion protein-dependent synaptotoxicity. Nature Comm., 4:1-9, 2013.

[69] S. Li, S. Hong, N. E. Shepardson, D. M. Walsh, G. M. Shankar and D. Selkoe. Soluble oligomers of amyloid β-protein facilitate hippocampal long-term depression by disrupting neuronal glutamate uptake. Neuron., 62(6):788–801, 2009.

[70] C. Cunningham. Microglia and neurodegeneration: The role of systemic inflammation. GLIA, 61(1):71–90, 2013.

[71] G. Eskici and P. H. Axelsen. Copper and Oxidative Stress in the Pathogenesis of Alzheimer's Disease. Biochem., 51(32):6289–6311, 2012.

[72] A. E. McDermott and T. Polenova. Solid-State NMR Studies of Biopolymers. John Wiley & Sons Ltd., Chichester, United Kingdom, 1st edition, 2010.

[73] P. Hodgkinson, editor. Modern methods in solid-state NMR. Royal Society of Chemistry, Cambridge, United Kingdom, 1st edition, 2018.

[74] P. C. A. van der Wel. New applications of solid-state NMR in structural biology. Emerging Topics in Life Sciences,1:1-11, 2018.

[75] A. Loquet, N. El Mammeri, J. Stanek, M. Berbon, B. Bardiaux, G. Pintacuda and B. Habenstein. 3D structure determination of amyloid fibrils using solid-state NMR spectroscopy. Methods, 138-139:26-38, 2018.

[76] H. Heise. Solid-State NMR Spectroscopy of Amyloid Proteins. ChemBioChem, 9(2):179-189, 2008.

[77] R. Tycko. Solid-State NMR Studies of Amyloid Fibril Structure. Annu. Rev. Phys. Chem., 62:279–99, 2011.

[78] D. Huang, B. C. Hudson, Y. Gao, E. K. Roberts and A. K. Paravastu. Chapter 2 - Solid-State NMR Structural Characterization of Self-Assembled Peptides with Selective 13C and 15N Isotopic Labels. Peptide Self-Assembly: Methods and Protocols, Methods in Molecular Biology, vol. 1777. Springer Nature, New York, United States of America, 1st edition, 2018.

[79] J. Keeler. Understanding NMR spectroscopy. John Wiley & Sons Ltd., Chichester, United Kingdom, 2nd edition, 2010.

[80] M. H. Levitt. Spin Dynamics. John Wiley & Sons Ltd., Chichester, United Kingdom, 2nd edition, 2008.

[81] M. J. Duer. Solid-State NMR Spectroscopy. Blackwell Science, Oxford, United Kingdom, 1st edition, 2002.

[82] E.R. Andrew, A. Bradbury and R.G. Eades. Nuclear Magnetic Resonance Spectra from a Crystal rotated at High Speed. Nature, 182(4650):1659-1659, 1958.

[83] A. E. Bennett, C. M. Rienstra, M. Auger, K. V. Lakshmi and Robert G. Griffin. Heteronuclear decoupling in rotating solids. J. Chem. Phys., 103(16):6951-6958, 1995.

[84] T. R. Carver and C.P. Slichter. Polarization of Nuclear Spins in Metals. Physical Review, 92(1):212-213, 1953.

[85] C. Sauvée, M. Rosay, G. Casano, F. Aussenac, R. T. Weber, O. Ouari and P. Tordo. Highly Efficient, Water-Soluble Polarizing Agents for Dynamic Nuclear Polarization at High Frequency. Angewandte Chemie, 125(41):11058-11061, 2013.

[86] C. F. Hwang and D. A. Hill. New Effect in Dynamic Polarization. Phys. Rev. Let., 18(4):110-112, 1967.

[87] C. F. Hwang and D. A. Hill. Phenomenological Model for the New Effect in Dynamic Polarization. Phys. Rev. Let., 19(18):1011-1014, 1967.

[88] D. Lee, S. Hediger and G. De Paëpe. Is solid-state NMR enhanced by dynamic nuclear polarization? Solid State Nuc. Mag. Res., 66–67:6-20, 2015.

[89] M. Rosay, L. Tometich, S. Pawsey, R. Bader, R. Schauwecker, M. Blank, P. M. Borchard, S. R. Cauffman, K. L. Felch, R. T. Weber, R. J. Temkin, R. G. Griffin and W. E. Maas. Solid-state dynamic nuclear polarization at 263 GHz: spectrometer design and experimental results. Phys. Chem. Chem. Phys., 12(22):5850-5860, 2010.

[90] K. R. Thurber and R. Tycko. Theory for cross effect dynamic nuclear polarization under magic-angle spinning in solid state nuclear magnetic resonance: The importance of level crossings. J. Chem. Phys., 137(8):1-14, 2012.

[91] F. Mentink-Vigier, Ü. Akbey, Y. Hovav, S. Vega, H. Oschkinat and A. Feintuch. Fast passage dynamic nuclear polarization on rotating solids. J. Mag. Res., 224:13-21, 2012.

[92] T. Maly, G. T. Debelouchina, V. S. Bajaj, K.-N. Hu, C.-G. Joo, M. L. Mak–Jurkauskas, J. R. Sirigiri, P. C. A. van der Wel, J. Herzfeld, R. J. Temkin and R. G. Griffin. Dynamic nuclear polarization at high magnetic fields. J. Chem. Phys., 128:1-19, 2008.

[93] L. Kuhn, editor. Hyperpolarization Methods in NMR Spectroscopy. Springer-Verlag, Heidelberg, Germany, 1st edition, 2013.

[94] K. N. Hu, H. Yu, T. M. Swager and R. G. Griffin. Dynamic nuclear polarization with biradicals. J. Am. Chem. Soc., 126(35):10844-10845, 2004.

[95] T. A. Siaw, A. Leavesley, A. Lund, I. Kaminker and S. Han. A versatile and modular quasi optics-based 200 GHz dual dynamic nuclear polarization and electron paramagnetic resonance instrument. J. Mag. Res., 264:131–153, 2016.

[96] M. Schmidt, A. Rohou, K. Lasker, J. K. Yadav, C. Schiene-Fischer, M. Fändrich and N. Grigorieff. Peptide dimer structure in an Aβ(1–42) fibril visualized with cryo-EM. Proc. Natl. Acad. Sci. U.S.A., 112(38):11858–11863, 2015.

[97] L. Gu, J. Tran, L. Jiang and Z. Guo. A new structural model of Alzheimer's Aβ42 fibrils based on electron paramagnetic resonance data and Rosetta modeling. J. Struc. Biol., 194:61–67, 2016.

[98] L. Gremer, D. Schölzel, C. Schenk, E. Reinartz, J. Labahn, R. B. G. Ravelli, M. Tusche, C. Lopez-Iglesias, W. Hoyer, H. Heise, D. Willbold, G. F. Schröder. Fibril structure of amyloid-β(1-42) by cryo-electron microscopy. Science, 358:116-119, 2017.

[99] O. Brener, T. Dunkelmann, L. Gremer, T. van Groen, E. A. Mirecka, I. Kadish, A. Willuweit, J. Kutzsche, D. Jürgens, S. Rudolph, M. Tusche, P. Bongen, J. Pietruszka, F. Oesterhelt, K.-J. Langen, H.-U. Demuth, A. Janssen, W. Hoyer, S. A. Funke, L. Nagel-Steger and D. Willbold. QIAD assay for quantitating a compound's efficacy in elimination of toxic Aβ oligomers. Sci. Rep., 5(13222):1-13, 2015.

[100] B. M. Fung, A. K. Khitrin and K. Ermolaev. An improved broadband decoupling sequence for liquid crystals and solids. J. Magn. Reson., 142:97–101, 2000.

[101] W. Lee, M. Tonelli and J. L. Markley. NMRFAM-SPARKY: enhanced software for biomolecular NMR spectroscopy. Bioinformatics, 31(8):1325–1327, 2014.

[102] C. Ader, R. Schneider, K. Seidel, M. Etzkorn, S. Becker and Marc Baldus. Structural Rearrangements of Membrane Proteins Probed by Water-Edited Solid-State NMR Spectroscopy. J. Am. Chem. Soc., 131(1):170–176, 2009.

[103] F. Delaglio, S. Grzesiek, G. W. Vuister, G. Zhu, J. Pfeifer and Ad Bax. NMRpipe - a multidimensional spectral processing system based on unix pipes. J. Biomol. NMR, 6(3):277–293, 1995.

[104] S. P. Skinner, R. H. Fogh, W. Boucher, T. J. Ragan, L. G. Mureddu and G. W. Vuister. CcpNmr Analysis Assign: a flexible platform for integrated NMR analysis. J. Biomol. NMR, 66:111–124, 2016.

[105] K. Schmidt-Rohr and Hans Spiess. Multidimensional Solid-State NMR and Polymers. Academic Press, San Diego, United States of America, 1st edition, 1994.

[106] W. Luo and M. Hong. Conformational Changes of an Ion Channel Detected Through Water-Protein Interactions Using Solid-State NMR Spectroscopy. J. Am. Chem. Soc., 132(7):2378–2384, 2010.

[107] J. K. Williams and M. Hong. Probing membrane protein structure using water polarization transfer solid-state NMR. J. Magn. Res., 247:118-127, 2014.

[108] Y. Shen and A. Bax. Protein backbone and sidechain torsion angles predicted from NMR chemical shifts using artificial neural networks. J. Biomol. NMR, 56(3):227–241, 2013.

[109] A. H. DePace and J. S. Weissman. Nat. Struct. Biol., 9(5):389–396, 2002.

[110] Y. Inoue, A. Kishimoto, J. Hirao, M. Yoshida and H. Taguchi. Strong Growth Polarity of Yeast Prion Fiber Revealed by Single Fiber Imaging. J. Biol. Chem., 276(38):35227–35230, 2001.

[111] R. Zhang, X. Hu, H. Khant, S. J. Ludtke, W. Chiu, M. F. Schmid, C. Frieden and J.-M. Lee. Interprotofilament interactions between Alzheimer's Aβ1–42 peptides in amyloid fibrils revealed by cryoEM. Proc. Natl. Acad. Sci. U.S.A., 106(12):4653-4658, 2009.

[112] H. Heise, W. Hoyer, S. Becker, O. C. Andronesi, D. Riedel and M. Baldus. Molecular-level secondary structure, polymorphism, and dynamics of full-length α-synuclein fibrils studied by solid-state NMR. Proc. Natl. Acad. Sci. U.S.A., 102(44):15871-15876, 2005.

[113] M. Hohwy, C. M. Rienstra, C. P. Jaroniec and R. G. Griffin. Fivefold symmetric homonuclear dipolar recoupling in rotating solids: Application to double quantum spectroscopy. J. Chem. Phys., 110(16):7983-7992, 1999.

[114] M. Baldus, A. T. Petkova, J. Herzfeld and R. G. Griffin. Cross polarization in the tilted frame: assignment and spectral simplification in heteronuclear spin systems. Mol. Phys., 95(6):1197-1207, 1998.

[115] K. Takegoshi, S. Nakamura and T. Terao. 13C-1H dipolar-assisted rotational resonance in magic-angle spinning NMR. Chem. Phys. Let. 344(5-6):, 631-637, 2001.

[116] C. Shi, H. K. Fasshuber, V. Chevelkov, S. Xiang, B. Habenstein, S. K. Vasa, S. Becker and A. Lange. BSH-CP based 3D solid-state NMR experiments for protein resonance assignment. J. Biomol. NMR, 59(1):15–22, 2014.

[117] R. Verel, M. Ernst and B. H. Meier. Adiabatic dipolar recoupling in solid-state NMR: The DREAM scheme. J. Magn. Reson., 150(1):81-99, 2001.

[118] G. De Paepe, J. R. Lewandowski, A. Loquet, A. Böckmann and R. G. Griffin. Proton assisted recoupling and protein structure determination. J. Chem. Phys., 129(24):1-21, 2008.

[119] S. Schwarzinger, G. J. A. Kroon, T. R. Foss, P. E. Wright and H. J. Dyson. Random coil chemical shifts in acidic 8 M urea: Implementation of random coil shift data in NMRView. J. Biomol. NMR, 18(1):43–48, 2000.

[120] S. H. Li, M. Hong, Protonation, Tautomerization, and Rotameric Structure of Histidine: A Comprehensive Study by Magic-Angle-Spinning Solid-State NMR. J. Am. Chem. Soc., 133(5):1534-1544, 2011.

[121] P. Keim, R. A. Vigna, J. S. Morrow, R. C. Marshall and F. R. N. Gurd. Carbon 13 Nuclear Magnetic Resonance of Pentapeptides of Glycine Containing Central Residues of Serine, Threonine, Aspartic and Glutamic Acids, Asparagine, and Glutamine. J. Biol. Chem., 248(22):7811-7818, 1973.

[122] S. R. Hartmann and E. L. Hahn. Nuclear Double Resonance in the Rotating Frame. Phys. Rev., 128(5):2042-2053, 1962.

[123] G. Cornilescu, F. Delaglio and A. Bax. Protein backbone angle restraints from searching a database for chemical shift and sequence homology. J. Biomol. NMR, 13(3):289–302, 1999.

[124] H. Saito. Conformation dependent 13C chemical shifts: A new means of conformational characterization as obtained by high-resolution solid-state 13C NMR. Magn. Reson. Chem., 24(10):835–852, 1986.

[125] D. S. Wishart and B. D. Sykes. The 13C chemical-shift index: A simple method for the identification of protein secondary structure using 13C chemical-shift data. J. Biomol. NMR, 4(2):171–180, 1994.

[126] J. Lewandowski, G. De Paëpe and R. G. Griffin. Proton Assisted Insensitive Nuclei Cross Polarization. J. Am. Chem. Soc., 129(4):728-729, 2007.

[127] J.-M. Lopez del Amo, D. Schneider, A. Loquet, A. Lange and B. Reif. Cryogenic solid state NMR studies of fibrils of the Alzheimer's disease amyloid-β peptide: perspectives for DNP. 56(4):359–363, 2013.

[128] S. Lange, A. H. Linden, Ü. Akbey, W. T. Franks, N. M. Loening, B.-J. van Rossum and H. Oschkinat. The effect of biradical concentration on the performance of DNP-MAS-NMR. J. Magn. Res., 216:209-212, 2012.

[129] Ü. Akbey, A. H. Linden and H. Oschkinat. High-Temperature Dynamic Nuclear Polarization Enhanced Magic-Angle-Spinning NMR. Appl. Magn. Reson., 43(1-2):81–90, 2012.

[130] T. Bauer, C. Dotta, L. Balacescu, J. Gath, A. Hunkeler, A. Böckmann and B. H. Meier. Line-Broadening in Low-Temperature Solid-State NMR Spectra of Fibrils. J. Biomol. NMR, 67(1):51–61, 2017.

[131] D. F. Hansen, P. Neudecker and L. E. Kay. Determination of Isoleucine Side-Chain Conformations in Ground and Excited States of Proteins from Chemical Shifts. J. Am. Chem. Soc., 132(22):7589–7591, 2010.

[132] V. S. Bajaj, P. C. A. van der Wel, and R. G. Griffin. Observation of a low-temperature, dynamically driven structural transition in a polypeptide by solid-state NMR spectroscopy. J. Am. Chem. Soc., 131(1):118–128, 2009.

[133] T. Zinkevich, V. Chevelkov, B. Reif, K. Saalwächter and A. Krushelnitsky. Internal protein dynamics on ps to μs timescales as studied by multi-frequency 15N solid-state NMR relaxation. J. Biomol. NMR, 57(3):219–235, 2013.

[134] A. A. Smith, E. Testori, R. Cadalbert, B. H. Meier and M. Ernst. Characterization of fibril dynamics on three timescales by solid-state NMR. J. Biomol. NMR, 65(3–4):171–191, 2016.

[135] J. M. Lamley, M. J. Lougher, H. J. Sass, M. Rogowski, S. Grzesiek and J. R. Lewandowski. Unraveling the complexity of protein backbone dynamics with combined 13C and 15N solid-state NMR relaxation measurements. Phys. Chem. Chem. Phys., 17:21997-22008, 2015.

[136] J. R. Lewandowski. Advances in solid-state relaxation methodology for probing site-specific protein dynamics. Acc. Chem. Res., 46(9):2018–27, 2013.

[137] P. Schanda and M. Ernst. Studying Dynamics by Magic-Angle Spinning Solid-State NMR Spectroscopy: Principles and Applications to Biomolecules. Prog. Nucl. Magn. Reson. Spectrosc., 96:1–46, 2016.

[138] J. R. Lewandowski, H. J. Sass, S. Grzesiek, M. Blackledge and Lyndon Emsley. Site-Specific Measurement of Slow Motions in Proteins. J. Am. Chem. Soc., 133(42):16762–16765, 2011.

[139] M. H. Levitt, T. G. Oas and Robert G. Griffin. Rotary Resonance Recoupling in Heteronuclear Spin Pair Systems. Isr. J. Chem., 28(4):271-282, 1988.

[140] T. G. Oas, R. G. Griffin and M. H. Levitt. Rotary resonance recoupling of dipolar interactions in solid-state nuclear magnetic resonance spectroscopy. J. Chem. Phys., 89(2):692-695, 1988.

[141] N. C. Nielsen, H. Bildsøe, H. J. Jakobsen and M. H. Levitt. Double-quantum homonuclear rotary resonance: Efficient dipolar recovery in magic-angle spinning nuclear magnetic resonance. J. Chem. Phys., 101(3):1805-1812, 1994.

[142] G. Lv, Ashutosh Kumar, Y. Huang and D. Eliezer. A Protofilament-Protofilament Interface in the Structure of Mouse α-Synuclein Fibrils. Biophys. J. , 114(12):2811-2819, 2018.

[143] E. Liepinsh and G. Otting. Proton exchange rates from amino acid side chains-implications for image contrast. Magn. Reson. Med., 35:30-42, 1996.

[144] A. Böckmann, C. Gardiennet, R. Verel, A. Hunkeler, A. Loquet, G. Pintacuda, L. Emsley, B. H. Meier and A. Lesage. Characterization of different water pools in solid-state NMR protein samples. J. Biomol. NMR, 45(3):319–327, 2009.

[145] T. Wang, H. Jo, W. F. DeGrado and M. Hong. Water Distribution, Dynamics, and Interactions with Alzheimer's β-Amyloid Fibrils Investigated by Solid-State NMR. J. Am. Chem. Soc., 139(17):6242–6252, 2017.

[146] J. K. Williams and M. Hong. Probing membrane protein structure using water polarization transfer solid-state NMR. J. Magn. Res., 247:118-127, 2014.

[147] O. C. Andronesi, M. von Bergen, J. Biernat, K. Seidel, C. Griesinger, E. Mandelkow and Marc Baldus. Characterization of Alzheimer's-like Paired Helical Filaments from the Core Domain of Tau Protein Using Solid-State NMR Spectroscopy. J. Am. Chem. Soc., 130(18):5922–5928, 2008.

[148] A. K. Schütz, A. Soragni, S. Hornemann, A. Aguzzi, M. Ernst, A. Böckmann and B. H. Meier. The Amyloid–Congo Red Interface at Atomic Resolution. Angew. Chem. Int. Ed., 50(26): 5956-5960, 2011.

[149] E. V. Hackl, J. Darkwah, G. Smith and I. Ermolina. Effect of acidic and basic pH on Thioflavin T absorbance and fluorescence. Eur. Biophys. J., 44(4):249–261, 2015.

[150] M. Groenning. Binding mode of Thioflavin T and other molecular probes in the context of amyloid fibrils - current status. J. Chem. Biol., 3(1):1-18, 2010.

[151] C. Seuring, J. Verasdonck, P. Ringler, R. Cadalbert, H. Stahlberg, A. Böckmann, B. H. Meier and R. Riek. Amyloid Fibril Polymorphism: Almost Identical on the Atomic Level, Mesoscopically Very Different. J. Phys. Chem. B, 121(8):1783–1792, 2017.

[152] G. Di Fede, M. Catania, M. Morbin, G. Rossi, S. Suardi, G. Mazzoleni, M. Merlin, A. R. Giovagnoli, S. Prioni, A. Erbetta, C. Falcone, M. Gobbi, L. Colombo, A. Bastone, M. Beeg, C. Manzoni, B. Francescucci, A. Spagnoli, L. Cantù, E. Del Favero, E. Levy, M. Salmona and F. Tagliavini. A Recessive Mutation in the APP Gene with Dominant-Negative Effect on Amyloidogenesis. Science, 323(5920):1473-1477, 2009.

[153] C. Nilsberth, A. Westlind-Danielsson, C. B. Eckman, M. M. Condron, K. Axelman, C. Forsell, C. Stenh, J. Luthman, D. B. Teplow, S. G. Younkin, J. Näslund and L. Lannfelt. The 'Arctic' APP mutation (E693G) causes Alzheimer's disease by enhanced Aβ protofibril formation. Nature Neuroscience, 4:887–893, 2001.

9 Danksagung

In erster Linie bedanke ich mich bei Frau Prof. Dr. Henrike Heise für die Vergabe des interessanten und kompetitiven Themas und darüberhinaus für ihre Unterstützung während meiner Dissertation.

Ausdrücklicher Dank geht auch an Jun.-Prof. Dr. Gunnar Schröder für die Übernahme der Zweitkorrektur dieser Arbeit und die Durchführung und Interpretation der cryoEM-Messungen.

Anschließend möchte ich mich bei Dr. Lothar Gremer für die Bereitstellung der Probe, der Anregung fachlicher Diskussionen und der kontinuierlichen Vorantreibung des Projekts bedanken.

Darüberhinaus bedanke ich mich für die Beantwortung technischer Fragen und schneller Hilfe bei technischen Problemen bei Dr. Rudolf Hartmann und Kevin Bochinsky.

Ebenso bedanke ich mich bei meinen Arbeitskollegen, Dr. Claudia Beumer, Anna König, Kai Schmitz, Jürgen Schönborn, Dr. Franziska Weirich, Dr. Baran Uluca und zusätzlich bei allen aktuellen und ehemaligen Kollegen der AG Heise.

Abschließend bedanke ich mich für die vielen anregenden Diskussionen und konstruktive Kritik bei allen aktuellen und ehemaligen Kollegen im Institut für physikalische Biologie der Heinrich-Heine-Universität Düsseldorf.

Auch bei meinem Mentor Prof. Dr. Dieter Schumacher bedanke ich mich für seine Beratung während meiner Dissertation.

Unabdingbar während meiner kompletten Promotionszeit war die Unterstützung durch meine Familie und meine Freunde.

10

Eidesstattliche Erklärung

Ich versichere an Eides Statt, dass die Dissertation von mir selbständig und ohne unzulässige fremde Hilfe unter Beachtung der "Grundsätze zur Sicherung guter wissenschaftlicher Praxis an der Heinrich-Heine-Universität Düsseldorf" erstellt worden ist.

Ferner erkläre ich, dass ich in keinem anderen Dissertationsverfahren mit oder ohne Erfolg versucht habe, diese Dissertation einzureichen.